

# Development of a Dual-Particle Imaging System for Nonproliferation Applications

By

Alexis Pierre Valère Poitrasson-Rivière

A dissertation submitted in partial fulfillment  
of the requirements for the degree of  
Doctor of Philosophy  
(Nuclear Engineering and Radiological Sciences)  
in the University of Michigan  
2016

Doctoral Committee:

Professor Sara A. Pozzi, Chair  
Assistant Professor Marek Flaska, Penn State University  
Professor Zhong He  
Associate Professor David D. Wentzloff

© Alexis Pierre Valère Poitrasson-Rivière  
2016

## **Dedication**

This work is dedicated to my rock and my wind.

## **Acknowledgements**

I would first of all like to thank my family and friends for supporting me throughout my doctoral studies. I would also like to thank my advisor, my committee members, the faculty and staff at the Nuclear Engineering & Radiological Sciences department, as well as all the students I had the chance to interact with, for making this experience fulfilling and enjoyable from start to finish.

I would finally like to thank the different sponsors that have helped make this work possible. This work is supported, in part, by the U.S. Defense Threat Reduction Agency under Grant No. HDTRA1-09-C-0012, by the National Nuclear Security Administration through NA-22 funding opportunity DE-FOA-0000568, and by the National Science Foundation and the Domestic Nuclear Detection Office of the Department of Homeland Security through the Academic Research Initiative Award #CMMI 0938909. The prototype systems described in this work are funded by the Department of Energy, Nuclear Energy University Program, Award #DE-NE0000324.

## Table of Contents

<b>Dedication .....</b>	<b>ii</b>
<b>Acknowledgements .....</b>	<b>iii</b>
<b>List of Figures.....</b>	<b>vi</b>
<b>List of Tables .....</b>	<b>x</b>
<b>List of Appendices.....</b>	<b>xi</b>
<b>Chapter 1. Introduction .....</b>	<b>1</b>
1.1. From Nuclear Physics to Nuclear Nonproliferation.....	1
1.2. Nuclear Nonproliferation .....	2
1.3. Radiation Imaging .....	4
1.4. Radiation Imaging in Nuclear Nonproliferation .....	5
<b>Chapter 2. Compton Imaging – The iFind Project.....</b>	<b>8</b>
2.1. Premise .....	8
2.2. Two-Plane Compton Camera Concept.....	9
2.3. Tools and Methodology .....	11
2.3.1. <i>MCNPX-PoliMi and MPPost</i> .....	11
2.3.2. <i>Terrestrial Background Model</i> .....	15
2.3.3. <i>Lanthanum Intrinsic Background Model</i> .....	16
2.3.4. <i>Detection of Imageable Events</i> .....	17
2.3.5. <i>Backprojection Imaging</i> .....	18
2.4. Results .....	20
2.4.1. <i>Scatter-Plane Optimization</i> .....	20
2.4.2. <i>Absorption-Plane Optimization</i> .....	23
2.4.3. <i>Minimum Detectable Activity Study</i> .....	26
2.4.4. <i>MLEM – Backprojection Comparison</i> .....	30
2.4.5. <i>Validation Measurements</i> .....	32
2.5. Advantages and Limitations of Compton Imaging .....	34
<b>Chapter 3. Neutron Imaging.....</b>	<b>36</b>
3.1. Premise .....	36
3.2. Neutron-Scatter Camera Concept.....	37
3.3. Tools and Methodology .....	38
3.4. Simulation validation .....	42
3.4.1. <i>Measurement Setup</i> .....	43
3.4.2. <i>Results Comparison</i> .....	44
3.5. Advantages and Limitations of a Neutron-Scatter Camera.....	46

<b>Chapter 4. Dual Particle Imaging System .....</b>	<b>48</b>
4.1. Premise .....	48
4.2. Three-Plane Dual-Particle Imaging Concept .....	49
4.3. Data-Acquisition Executable and Real-Time Processing .....	53
4.3.1. <i>Prototype Setup</i> .....	53
4.3.2. <i>Synchronization Procedure</i> .....	58
4.3.3. <i>System Capabilities</i> .....	59
4.4. Three-Plane DPI Results .....	61
4.5. Advantages and Limitations of the Three-Plane DPI System .....	66
<b>Chapter 5. Two-Plane DPI System.....</b>	<b>67</b>
5.1. Two-Plane DPI Concept & Optimization .....	67
5.1.1. <i>Concept Design</i> .....	67
5.1.2. <i>Optimization</i> .....	68
5.2. Results .....	74
5.2.1. <i>Efficiency &amp; Field of View</i> .....	74
5.2.2. <i>MOX Measurements</i> .....	78
5.2.3. <i>Angular-Resolution Analysis</i> .....	79
5.2.4. <i>Simulation Validation</i> .....	83
5.2.5. <i>Material Characterization</i> .....	84
5.3. Summary, Advantages, and Limitations of the Two-Plane DPI System .....	86
<b>Chapter 6. Summary, Conclusion and Future Improvements .....</b>	<b>89</b>
6.1. Conclusions .....	89
6.2. Future Improvements .....	91
<b>Appendices.....</b>	<b>94</b>
<b>References.....</b>	<b>147</b>

## List of Figures

Fig. 1-1. Evolution of the atom model through the years [1]. .....	1
Fig. 2-1. Artist rendition of the Compton-camera set-up on the back of a truck.....	9
Fig. 2-2. Principle of source localization with a two-plane Compton camera; the ‘location-probability’ cone is created using Compton-scattering physics. The source can be located anywhere on the surface of the cone; therefore, the intersection of several cones is required. ....	10
Fig. 2-3. Relative Compton scatter to total interaction cross-sections for several scintillators at energies up to 1000 keV. For the energy range shown, pair-production is not an option so the photoelectric absorption cross-section is the remaining part of the total cross-section. ....	11
Fig. 2-4. Excerpt from the MCNPX-PoliMi output file. The time value, truncated here to 3 significant numbers for ease of reading, has a precision of $10^{-2}$ shakes ( $10^{-1}$ ns).....	12
Fig. 2-5. Flow chart of the data-analysis algorithm. ....	13
Fig. 2-6. MCNP source term implemented to the background model. ....	15
Fig. 2-7. Comparison of simulated and measured background data collected with an HPGe detector. The measured background data was obtained from SNL. ....	15
Fig. 2-8. Model of the background source. The soil cylinder was located 1 m below the system. The radius R was set to 12 m in the simulations.....	16
Fig. 2-9. Number of correlated counts per second for a varying time window half-width with a $\text{CaF}_2/\text{LaBr}_3$ camera. All other systems displayed similar trends. The secondary axis corresponds to the ‘Source’ and ‘Mixed’ curves. ....	18
Fig. 2-10. Uncollided (shown on right axis), single-scattered, and multiple-scattered (shown on left axis) photon flux incident on the absorption-plane; incident photon source energy of 300 keV. ....	21
Fig. 2-11. Figure of merit plotted as a function of $\text{CaF}_2$ scatter-plane thickness for monoenergetic photons with energies between 100 and 400 keV. A region of optimum scatter-plane thickness can be identified around the peaks of the curves (1.5 to 2.5 cm).....	22
Fig. 2-12. Figure of merit plotted as a function of $\text{C}_9\text{H}_{10}$ scatter-plane thickness for monoenergetic photons with energies between 100 and 400 keV. A region of optimum scatter-plane thickness can be identified around the peaks of the curves (3.3 to 5.3 cm).....	23
Fig. 2-13. Illustration of the variables in the calculation used for the angular uncertainty associated to the absorption plane. ....	25
Fig. 2-14. $\text{FOM}_{\text{abs}}$ plotted for $\text{LaBr}_3$ as a function of thickness and detector side length for 400-keV photons. ....	26

Fig. 2-15 Energy distribution of the correlated counts produced by background radiation, collected by a CaF <sub>2</sub> / NaI(Tl) camera. The error bars (on the order of 10 %) were omitted from the plot for clarity. ....	27
Fig. 2-16. Backprojection image of the background with the 662 keV energy window for a CaF <sub>2</sub> /NaI(Tl) camera. The simulation was set to mimic a 60 s measurement. ....	28
Fig. 2-17. Linear fit of the cone fluctuation (with the 662 keV $\pm$ 10% energy window) versus the simulated measurement time. The standard deviations observed ranged from approximately 5 to 15. ....	28
Fig. 2-18. Image of a 1.65 mCi Cs-137 source centered 100 m in front of the system (including the background). The simulation was set to mimic a 60 s measurement. ....	29
Fig. 2-19. Backprojection image of the 600-700 keV bin for a 1-min simulated measurement. The angular coordinates of the source are (90°,90°). ....	31
Fig. 2-20. MLEM image of the 600-700 keV bin for a 1-min simulated measurement after 25 iterations. ....	32
Fig. 2-21. Measurement setup with a Na-22 source at x=-30 cm, y=50 cm, and z=0 cm. The origin of the coordinates is at the center of the front face of the scatter plane. ....	33
Fig. 2-22. Comparison of backprojection images from simulated (top) and measured (bottom) data. Only energies between 400 and 600 keV were imaged. The angular coordinates of the source are (121°,90°). ....	34
Fig. 3-1. Schematics of a neutron-scatter camera with a neutron event depicted and the associated backprojection cone. ....	37
Fig. 3-2. Various fits of the light output for neutron energy deposited. ....	41
Fig. 3-3. Relative difference between simulation and measurements of a Cf-252 source. ....	42
Fig. 3-4. Side (a) and front (b) views of the MCNPX-PoliMi model of the small-scale prototype and the source location. ....	43
Fig. 3-5. Reconstructed energy spectra obtained from a Cf-252 source for a 10-h measurement and the corresponding simulation. Error bars were omitted as they were indistinguishable from the data points. ....	45
Fig. 3-6. Backprojection images of all neutron counts obtained from a Cf-252 source for a 10-h measurement (a), the corresponding simulation (b), and difference between both images normalized to their maximum intensity (c). ....	45
Fig. 4-1. Schematics of the DPI system, showing a photon type 1-3 event and a neutron type 1-2 event, along with the information used for image reconstruction. A backprojection cone is illustrated for the photon event. ....	50
Fig. 4-2. List of all events measurable with the DPI system. ....	51
Fig. 4-3. Once-collided neutron flux entering plane 2 for different incoming spectra (a) and comparison with the type 1-2 recorded counts for 2-MeV neutrons (b). ....	52
Fig. 4-4. Photograph of the prototype DPI system. ....	54
Fig. 4-5. Energy spectrum of a Cs-137 source measured with a NaI scintillator. ....	55



Fig. 4-6. Tail integral versus total integral plot used for PSD purposes. The color scale is logarithmic. ....	56
Fig. 4-7. Time delay between two 7.62-cm thick EJ-309 scintillators, obtained with a Na-22 source. ....	57
Fig. 4-8. CAEN VME crate containing 4 V1720 digitizers connected for time synchronization. ....	57
Fig. 4-9. Sampling clocks of the 4 synchronized digitizers. ....	58
Fig. 4-10. Diagram of the run command synchronization method. ....	59
Fig. 4-11. Delay between the first slave in the daisy chain and the master board. 'A' is the delay between the pulses within the data-acquisition window (leading-edge timing), 'B' is the delay between the time stamps, and 'A+B' is the global time delay between the boards. ....	59
Fig. 4-12. Architecture of the data-acquisition software. 'Proc thread' refers to a thread writing the data to the hard drive or a thread processing the data in real time. ....	60
Fig. 4-13. Neutron (a) and photon (b) images from the measurement of the Cf-252 source. The neutron image displays a hotspot in the direction of the source, while the photon image is overwhelmed by the background radiation. ....	62
Fig. 4-14. Photon (a) and neutron (b) images from the measurement of the Cs-137 source. ....	63
Fig. 4-15. Neutron reconstructed spectrum from the measurement of the Cf-252 source. ....	65
Fig. 4-16. Correlated photon spectrum from the measurement of the Cf-252 and the Cs-137 source, and a background measurement. ....	65
Fig. 5-1. Diagram of the two-plane DPI system. Gamma-ray and neutron events are illustrated, along with the information used for image reconstruction. ....	68
Fig. 5-2. Optimized DPI system used for the measurement campaign. A, B, and C are the distances investigated in the final optimization study. ....	69
Fig. 5-3. MCNPX-PoliMi simulation of the photon angular resolution measure (a) and correlated photon counts (b), for various geometries. The units of the color bars are degrees and counts, respectively. The values displayed here were averaged over the 5 plane separations investigated. ....	71
Fig. 5-4. MCNPX-PoliMi simulation of the angular resolution measure (a) and correlated counts (b), for various plane separations. The intra-plane detector separations used are 15 cm in the front plane and 25 cm in the back plane. ....	72
Fig. 5-5. Setup of the field of view measurements. ....	74
Fig. 5-6. Photon (1) and neutron (2) backprojection images for $\theta = 90^\circ$ (a), $\theta = 30^\circ$ (b), and $\theta = -70^\circ$ (c) ....	75
Fig. 5-7. Backplane event image for $\theta = -70^\circ$ (a), $\theta = 70^\circ$ (b), and standard photon image for $\theta = 70^\circ$ (c). ....	76
Fig. 5-8. Neutron efficiency map for the range of angles measured. ....	77
Fig. 5-9. Photon efficiency map for the range of angles measured. Only standard events are used for the calculation. ....	77

Fig. 5-10. Isotopic composition of the MOX1 sample (a) and corresponding neutron emission rates (b). SF denotes spontaneous fission.....	78
Fig. 5-11. View of the 2 MOX canisters, with a 5° separation, placed at a distance of 2.5 m from the DPI system. The canisters are highlighted with the white square. ....	79
Fig. 5-12. Gamma-ray (a) and neutron (b) backprojection images of 2 MOX canisters separated by 5° measured for 90 minutes. ....	80
Fig. 5-13. Gamma-ray (a) and neutron (b) backprojection images of 2 MOX canisters separated by 15° measured for 75 minutes. ....	80
Fig. 5-14. Gamma-ray (a) and neutron (b) backprojection images of 2 MOX canisters separated by 30° measured for 120 minutes. ....	81
Fig. 5-15. Gamma-ray backprojection hot-spot slices for all measured angular separations. ....	82
Fig. 5-16. Comparison between backprojection (a), MLEM (b), and SOE (c) neutron images for the 15° separation case.....	83
Fig. 5-17. Measured (a) and simulated (b) neutron backprojection images for the 30° separation case and a visualization of the difference between the images normalized to their highest intensity (c). ....	84
Fig. 5-18. TOF-derived neutron spectrum from the 30° separation case. The spectrum is obtained from the energy deposited in the first scatter and the subsequent TOF.....	85
Fig. 5-19. Emitted spectrum (a) and TOF-reconstructed spectrum (b) from MOX and plutonium metal.....	85
Fig. 5-20. Gamma-ray backprojection images for the summed energies between 300 and 800 keV (a) and for all other summed energies (b).....	86
Fig. 6-1. Venn diagrams of current imaging systems. ....	91

## **List of Tables**

Table 2-I. Results for the different camera configurations. ....	30
Table 3-I. Decrease, by order of magnitude, of the number of detectable particles for an added inch of shielding.....	46
Table 4-I. Expected performance of imaging methods in different desirable capabilities. ....	49
Table 4-II. Simulated counts obtained from $10^6$ incident 2 MeV neutrons and $10^6$ 662 keV photons. ....	53
Table 4-III. Principal gamma-ray signatures of SNM isotopes [43]. ....	64
Table 5-I. Relative differences of the optimization parameters to the chosen plane separation. .	73

## **List of Appendices**

Appendix A – Sample MCNP input file.....	94
Appendix B – Sample MPPost Input file.....	103
Appendix C – MPPost source code extract.....	109
Appendix D – Quick Acquisition source code extract.....	143

# Chapter 1. Introduction

## 1.1. From Nuclear Physics to Nuclear Nonproliferation

Nuclear physics started in the late 1800s with the discovery of radioactivity. Further discoveries led to the atom that we know today and the discovery of nuclear fission in the 1930s. Fig. 1-1 shows the evolution of the atom model throughout the years. Nuclear fission was at the origin of the problem this work aims to help with, as the discovery of fission chain reaction and the large amount of energy released per fission led to the invention of the nuclear bomb.

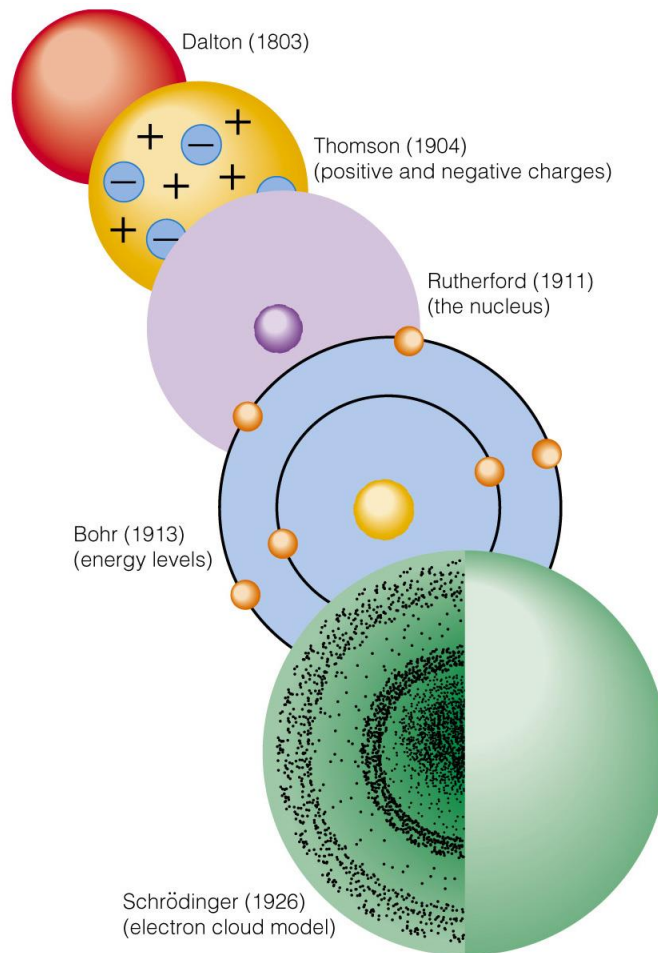


**Fig. 1-1. Evolution of the atom model through the years [1].**

As with any innovative work, research and development surrounding nuclear physics contained an inherent risk. The context of the cold war in the second part of the 20<sup>th</sup> century pushed people to put performance before safety, which resulted in deadly accidents. These events, coupled with the nuclear weapons used to end World War II resulted in a stigmatization of radiation, leading to an atmosphere of fear associated with nuclear topics.

While nuclear physics and radiation can be a fearsome endeavor, many peaceful nuclear applications have been created. Two applications are particularly well known: energy production and medical applications. Nuclear energy is based on the same nuclear chain reactions as nuclear weapons making it particularly risky to be diverted towards military use, as both most common technologies use the same original material (uranium and plutonium). Medical applications of nuclear radiation have been successful in helping both diagnostics with imaging, and cures, with radiation treatment. While these two civil applications make the headlines, radiation is helpful in many other fields. Food and agriculture uses radioisotope tracers to assess the performance of fertilizers, as well as to preserve food. Insect control has also benefitted from radiation by sterilizing insect eggs to reduce insect populations. Radiation is also used to assess air and water quality, as well as to date ancient artifacts in archeology. With the use of radiation becoming an important part of various fields, and nuclear energy making up more than 10% of the world electricity generation, the risk associated with nuclear radiation is a part of modern societies. As such, effort is carried out in keeping that risk under control, especially in the case of nuclear weapons.

## **1.2. Nuclear Nonproliferation**

Any discussion of nuclear nonproliferation should start with a clear explanation of what nuclear proliferation is. Nuclear proliferation is defined as “the process by which one nation after

another comes into possession of, or into the right to determine the use of, nuclear weapons" [2]. It results in the fact that "each nation becomes potentially able to launch a nuclear attack upon another nation" [2]. Nuclear proliferation can be enacted through a transfer of knowledge, technology, material, or actual weapon. A country can also develop nuclear weapons through its own effort and research.

Nuclear proliferation has been heavily opposed by many nations since the end of World War II, for the fear that more countries with nuclear weapons increases the risk of nuclear warfare. This opposition resulted in the creation of the International Atomic Energy Agency (IAEA) in 1957 and of the Treaty on the Non-Proliferation of Nuclear Weapons, commonly known as the Non-Proliferation Treaty (NPT), in 1968 [3]. This treaty recognizes five nuclear-weapon-possessing states: the United States (acquired in 1945), Russia (1949), the United Kingdom (1952), France (1960), and China (1964), while four other states have shown or are suspected to have nuclear weapons: India (acquired in 1974), Pakistan (1998), North Korea (2006), and Israel (suspected since 1979). The NPT is based on non-nuclear-weapon states agreeing to not acquire, and nuclear-weapon states agreeing not to transfer nuclear weapons. In exchange, the non-nuclear-weapon states receive the benefits of peaceful nuclear technology, obtained with the help of nuclear-weapon states. It also includes the goal to move towards nuclear disarmament for the nuclear-weapon states.

Three main nuclear detection activities derive from nuclear nonproliferation effort: the safeguarding of existing nuclear materials of interest, the verification of existing nuclear weapon stockpiles and their dismantlement, and the search for missing material and possible threat objects.

Nuclear safeguards rely on each state declaring its own nuclear material. These declarations include such information as how much material exists, and its location. Information on the design

of a state's nuclear facilities is also required. These declarations are verified by the IAEA with inspections of facilities, including nuclear measurements, to ensure all material is accurately accounted for.

Nuclear weapon verification relies on the accurate assessment of nuclear weapons. This implies being able to tell if the measured object is a nuclear warhead, and how many payloads it contains. This task can prove particularly difficult when states want to keep information about their weapons (such as the isotopes of the nuclear material used) secret.

The search for nuclear material or possible threat objects requires rugged and robust equipment that can be used in any environment. This application can be particularly time sensitive, which raises a need for detection systems capable of surveying large areas in a very short time. This search is further helped by the use of portal monitors at borders to prevent threat objects from moving freely between nations.

### **1.3. Radiation Imaging**

Imaging can be defined as “making a visual representation of something” [4]. In radiation imaging, it relates to creating a visual representation of the radiation emitted, or transmitted, by an object, an area, or a person. Radiation imaging has historically been linked to two main fields: medicine and astrophysics.

In the medicine field, imaging is used to inspect the body of a patient for possible ailments. Medical imaging encompasses various techniques that often include an outside source of radiation. The outside source can be a particle accelerator, generator, or a given radioisotope. Radioisotopes can even be ingested by the patient. The radiation is then attenuated or reacts in a certain way that is detected after the fact and reconstructed using imaging algorithms.



In the astrophysics field, imaging is used to map sources of radiation in the sky. This type of imaging relies on a passive detection system that receives radiation from the source it is trying to image. Such detection systems are typically called cameras and fall under three categories: pinhole, coded aperture, and coincidence cameras. A pinhole camera is a simple design used to image light as far back as ancient China [5]. It consists of a detection plane and a screen with a single pinhole. The image is projected through the pinhole onto the screen, reversed (flipped upside down and side to side). The small opening of the pinhole results in a low efficiency. A coded aperture relies on the same concept, but uses a screen with multiple holes. This greatly improves the efficiency of the camera at the cost of more advanced image processing. Finally, a coincidence camera relies on the detection of multiple interactions from the same particle. The physical laws governing these interactions are used to image the source. The coincidence camera concept, used for the imaging system presented in this work, will be introduced and discussed in chapters 2 and 3.

#### **1.4. Radiation Imaging in Nuclear Nonproliferation**

Radiation imaging has become, over the years, of interest in the nuclear nonproliferation field. All three of the main nuclear nonproliferation activities, namely safeguards, warhead verification and wide-area search, can benefit from imaging. The localization of missing material or radioactive objects, for example, is an application for which an imaging system is particularly suited [6]. Such an application requires a system capable of imaging sources at a large standoff in a short amount of time. Nuclear safeguards on the other hand require a constantly operating imaging system providing the localization of the materials of interest at all time, keeping track of their movements [7]. In such an application, the efficiency of the system would be of much lesser importance than the accuracy. In the case of nuclear-weapon verification, the system needs to be

precise enough to correctly identify a warhead and distinguish multiple payloads within a weapon [7, 8], but have very limited spectroscopic capabilities.

The use of nuclear imaging for nonproliferation applications has mostly stayed at the stage of research and conjectures, as imaging systems have not seen much use in the field. In the past, this research has focused on imaging gamma-rays emitted in large amounts by nuclear material of interest [6, 7, 8]. Neutron imaging has been further researched lately to image fissile material [9]. Both types of particle imaging present advantages and drawbacks that will be introduced in future chapters. Most of the imaging systems that have been developed have focused on a specific particle and application. As a consequence, detection systems capable of imaging and spectroscopy on both neutrons and gamma rays are scarce in the available technology and research on such systems is seldom present in the literature. One system similar to the one presented in this work is currently researched [10]. These imaging and spectroscopic capabilities, coupled with a large field of view, would make a system versatile and applicable to several nonproliferation areas.

It is in this context that I began my research work on an inexpensive versatile imaging system, suited for most nuclear nonproliferation tasks. My research started by focusing on both Compton and neutron-scatter imaging before combining them into the Dual-Particle Imaging (DPI) system. The DPI system was not designed with a particular application in mind, but with a focus on versatility and scalability, so that it can be adapted to all nuclear nonproliferation applications.

This thesis describes the different steps of the development of the DPI system. Extensive simulation work was originally performed on Compton camera design as part of a project funded by DTRA. Chapter 2 goes over this simulation work and the tools created to obtain realistic simulations. Chapter 3 describes the workings of a neutron-scatter camera and the additions

required to the data processing for dealing with neutrons. Chapter 4 introduces the DPI system and highlights the data acquisition software developed along with the first measured dual-particle imaging results obtained. Chapter 5 investigates the optimization of a two-plane DPI design, and presents measured results obtained with category-III special nuclear material (SNM).

## **Chapter 2. Compton Imaging – The iFind Project**

### **2.1. Premise**

Extensive work in astronomical and medical imaging has led to considerable knowledge of Compton cameras [11, 12, 13]. While these fields continue to experience development, there is an increasing body of work being generated for applications of Compton cameras in nuclear nonproliferation, where the focus is balanced between detection efficiency and angular resolution [14, 15]. Coded aperture imaging is an alternative for high efficiency applications that is particularly suited for low-energy gamma rays (below 400 keV) [16]. Compton cameras have an advantage at higher energies, where scattering cross-sections are dominant (until pair production takes over) [16]. They also typically possess a larger field of view and can derive more location information from each count than a coded aperture system.

In the nuclear-nonproliferation field, an important application is the localization of possible threat objects at large distances in any type of environment. This application requires a field-capable system able to image a source in a short amount of time. The system must either have a high efficiency, or be able to find the object location from a low number of recorded events. The iFind project, a DTRA-sponsored project involving ICx Technologies, Sandia National Laboratory, and the University of Michigan, was part of an effort to develop robust imaging solution for the localization of threat objects. The project started in the summer of 2009.

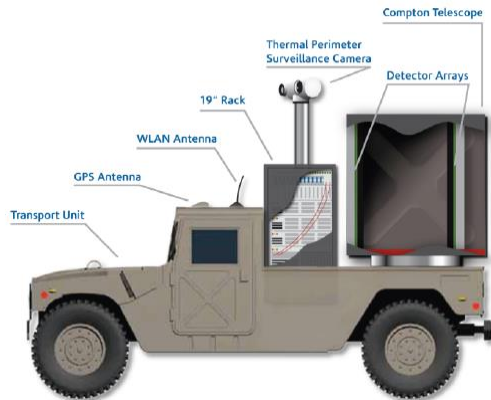


**Fig. 2-1. Artist rendition of the Compton-camera set-up on the back of a truck.**

The iFind project aimed at developing a large-scale Compton camera for nuclear nonproliferation applications. The system had to be robust enough to be used in the field, carried on the back of a truck for example, as shown in Fig. 2-1. It also had to be able to locate material of interest at large distances. Materials of interest included SNM (such as plutonium and highly-enriched uranium) as well as more common radioactive sources, such as Cs-137 or Co-60, which can be used for dirty bombs. Given the low energies emitted by SNM (186 keV for  $^{235}\text{U}$ , 300 to 400 keV for plutonium) the project began with the investigation of possibly using a hybrid imaging system using both coded aperture and Compton imaging [16]. This idea was quickly abandoned and the project focused solely on Compton imaging, as long-distance coded-aperture imaging systems were already the subject of existing research [6].

In this chapter, I present the tools developed for the research on the iFind system, the optimization of the different components of the system, and the analysis of the performance of the system for locating a source at a standoff of 100 meters.

## **2.2. Two-Plane Compton Camera Concept**

Compton cameras utilize Compton-scattering physics to find the possible origin of the detected particles. In simple backprojection methods, a cone is created from an axis defined by the

location of two separate interactions and a scatter angle. The scatter angle is calculated from the energy of the scattering event. The surface of the cone then represents the possible locations of the source. To correctly obtain the scatter angle, the incoming energy of the photon must be accurately measured. This is done by inducing a full-energy deposition after the scatter.

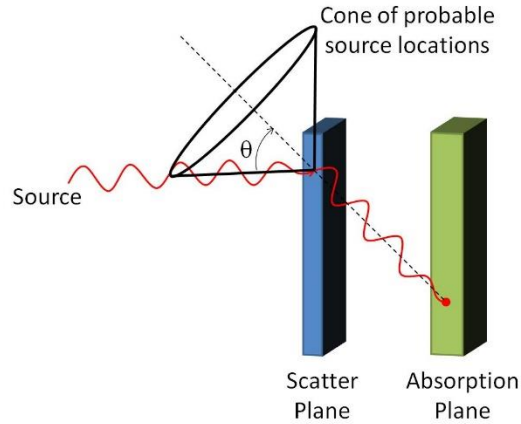


**Fig. 2-2. Principle of source localization with a two-plane Compton camera; the ‘location-probability’ cone is created using Compton-scattering physics. The source can be located anywhere on the surface of the cone; therefore, the intersection of several cones is required.**

Two-plane Compton cameras aim at maximizing the desirable events (single scatter followed by full-energy deposition) by having dedicated scatter and absorption planes. This principle is shown in Fig. 2-2, with the Compton formula relating the scatter angle to the deposited energies:

$$\cos \theta = 1 - \frac{m_e c^2 E_1}{E_0 (E_0 - E_1)}, \quad (1)$$

where  $E_0$  is the incoming photon energy,  $E_1$  the energy deposited in the scattering interaction, and  $m_e c^2$  the electron rest mass. The axis of the cone is determined from the locations of the two separate interactions.

The scintillator materials considered for this study were selected based on the ratio of Compton scatter to total interaction probabilities. Materials with favorable scatter-plane characteristics are generally low-Z materials which have a higher ratio, as shown in Fig. 2-3.

Although these materials are limited by their low energy resolutions, they are desirable due to the higher probability of Compton scattering. The scatter-plane materials selected for this study are  $\text{CaF}_2$  and  $\text{C}_9\text{H}_{10}$ . Conversely, due to high photoelectric absorption probabilities,  $\text{LaBr}_3$  and  $\text{NaI}$  were selected as the candidate absorption-plane materials.

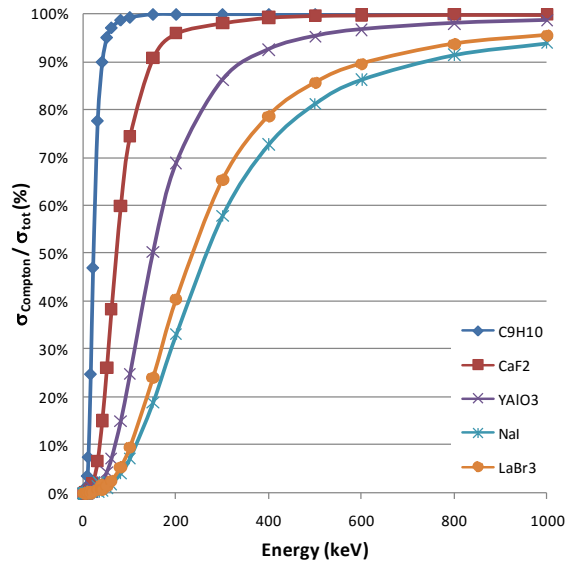


**Fig. 2-3. Relative Compton scatter to total interaction cross-sections for several scintillators at energies up to 1000 keV. For the energy range shown, pair-production is not an option so the photoelectric absorption cross-section is the remaining part of the total cross-section.**

## 2.3. Tools and Methodology

### 2.3.1. MCNPX-PoliMi and MPPost

Systems able to detect sources at large standoffs require a significant amount of active detector material and complex electronics, making it costly to carry out an appropriate performance assessment. To correctly estimate the response of a large-scale system, a simulation methodology was developed based on MCNPX-PoliMi's features [17]. The methodology includes realistic detector modeling, detection uncertainties, and terrestrial and intrinsic radiation backgrounds.

MCNPX-PoliMi creates an ASCII list-mode output file containing interaction information on user-specified cells of interest. An excerpt of this file is shown in Fig. 2-4. The information that is of particular importance to our endeavor is the energy deposited (column 7), the time of the interaction (column 8), the position (columns 9, 10, and 11), and cell of the interaction (column 6).

History Number	Particle Number	Projectile Type	Interaction Type	Target Nucleus (atomic number)	Cell Number of Collision Event	Energy Deposited (MeV)	Time (Shakes)	Collision Position (X) (Y) (Z)			Particle Weight	Generation Number	Number of Scatters	Code	Incoming Energy
67	1	2	1	28	424	0.062272	6.77E+09	10.77	39.45	5.57	1.00E+00	0	0	0	1.00E+00
67	1	2	3	53	312	0.909119	6.77E+09	-3.27	-29.31	13.35	1.00E+00	0	1	0	9.38E-01
67	1	2	3	53	312	0.028609	6.77E+09	-3.27	-29.31	13.34	1.00E+00	0	1	0	2.86E-02
89	1	2	1	28	444	0.203497	2.52E+09	11.99	27.42	-14.51	1.00E+00	0	0	0	1.00E+00
91	1	2	1	6	133	0.048103	8.08E+09	4.18	21.72	-2.96	1.00E+00	0	0	0	1.00E+00
91	1	2	1	28	534	0.037798	8.08E+09	3.42	14.85	-4.38	1.00E+00	0	1	0	9.52E-01
95	1	2	1	1	123	0.768787	2.37E+09	4.52	20.37	7.02	1.00E+00	0	0	0	1.00E+00
95	1	2	1	28	424	0.109532	2.37E+09	13.07	25.64	4.62	1.00E+00	0	1	0	2.31E-01
100	1	2	1	6	132	0.745951	7.95E+08	-4.71	21.04	-7.13	1.00E+00	0	0	0	1.00E+00
100	1	2	1	6	132	0.105172	7.95E+08	-7.03	23.62	-3.14	1.00E+00	0	1	0	2.54E-01
100	1	2	1	1	132	0.013707	7.95E+08	-6.7	22.01	-2.84	1.00E+00	0	2	0	1.49E-01

**Fig. 2-4. Excerpt from the MCNPX-PoliMi output file. The time value, truncated here to 3 significant numbers for ease of reading, has a precision of  $10^{-2}$  shakes ( $10^{-1}$  ns).**

Intrinsic spatial, energy, and time resolutions have to be added to the output data as they are not inherently included in the Monte Carlo simulations. A dedicated algorithm was written to compute a realistic detector response from the data file output of MCNPX-PoliMi [18]. Realistic parameters such as the pulse-generation time, energy and time broadening, and dynamic ranges (lower and upper energy discrimination levels) are applied to the data. This approach results in a detector response with an output line for each pulse containing information such as the pulse height, the time of the pulse, and the detector number. Fig. 2-5 shows the flow chart of the algorithm, from the MCNPX-PoliMi data output to the image reconstruction.



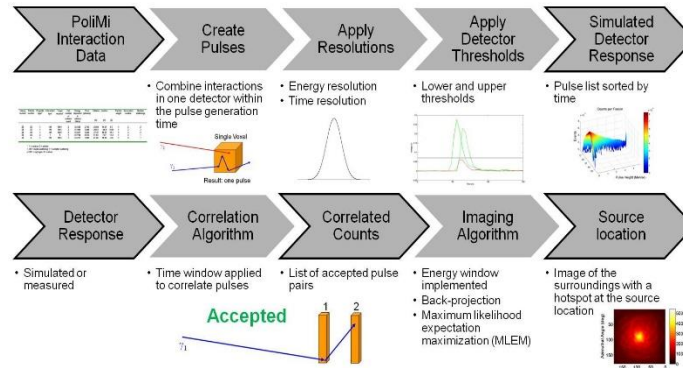


**Fig. 2-5. Flow chart of the data-analysis algorithm.**

The accuracy of the measured position of each interaction is limited by the detector size because the scintillators used are not position sensitive. As such, the coordinates of the interaction given by MCNPX-PoliMi were translated into the detector number.

When a photon undergoes more than one interaction within a detector, light pulses are created at approximately the same time, resulting in a single measured pulse combining the energy deposited from all the interactions. This effect is due to the time a pulse takes to be created: the pulse generation time (PGT). This phenomenon is included in the post processing by using a PGT window on the first interaction detected, and summing all the energy depositions happening within that time window. The PGT was set to 10 ns, based on the time properties of a typical photomultiplier tube (PMT).

The energy and time resolutions of detectors are Gaussian random processes, and as such need to be sampled from a Gaussian distribution. This procedure was carried out by using the Box-Muller transform [19] on a standard random number generator available in FORTRAN. The standard deviations of the Gaussian distributions were then calculated depending on the detector type.

Energy resolution equations were defined experimentally for each material of interest [20]:

C<sub>9</sub>H<sub>10</sub>:

$$\frac{fwhm}{E} = \left( \frac{129.6}{\sqrt{E}} + \frac{500}{E} + 2.7 \right) \% \quad (2)$$

CaF<sub>2</sub>:

$$\frac{fwhm}{E} = \left( \frac{51.86}{\sqrt{E}} + \frac{500}{E} + 3.1 \right) \% \quad (3)$$

NaI(Tl):

$$\frac{fwhm}{E} = \left( 811 \times E^{-1.06} - 5 \times \left( \frac{E}{4000} \right)^{1.8} + 6.2 \right) \% \quad (4)$$

LaBr<sub>3</sub>:

$$\begin{aligned} E \geq 100 \text{ keV} &\Rightarrow \frac{fwhm}{E} = \left( \frac{811}{E} - 5 \times \left( \frac{E}{3000} \right)^5 + 2.2 \right) \% \\ E < 100 \text{ keV} &\Rightarrow \frac{fwhm}{E} = \left( \frac{100}{\sqrt{E}} \right) \% \end{aligned} \quad (5)$$

The time uncertainty is particularly important to this application, as it can have a significant impact on the time correlation between pulses. Appropriate values in the nanosecond to tens of nanosecond range were chosen for each material based on their published properties [21]. While the time resolution will vary with the size of the pulse, which is proportional to the energy deposited, it was kept constant at a value that matched the range of desirable energies (hundreds of keV). Specifically, I used 1 ns for C<sub>9</sub>H<sub>10</sub> and LaBr<sub>3</sub>, 10 ns for NaI(Tl), and 24 ns for CaF<sub>2</sub>.

Several important simulation steps were required to simulate a Compton camera realistically. Gamma-ray background has to be included as it presents the main challenge to an accurate source localization. Two kinds of background radiation were considered: terrestrial background and intrinsic background from one of the detector materials (namely <sup>138</sup>La). Cosmic background was found to be negligible compared to terrestrial background and omitted from the study.

### 2.3.2. Terrestrial Background Model

A background model designed by Sandia National Laboratories (SNL) [22] was applied to the iFind simulations. The model consists of a relatively complex source term, shown in Fig. 2-6, which was isotropically distributed within a SiO<sub>2</sub> soil cube. This model was simulated with an HPGe detector model and compared to measured data from SNL. Fig. 2-7 shows the resulting energy spectra, which show a good agreement.

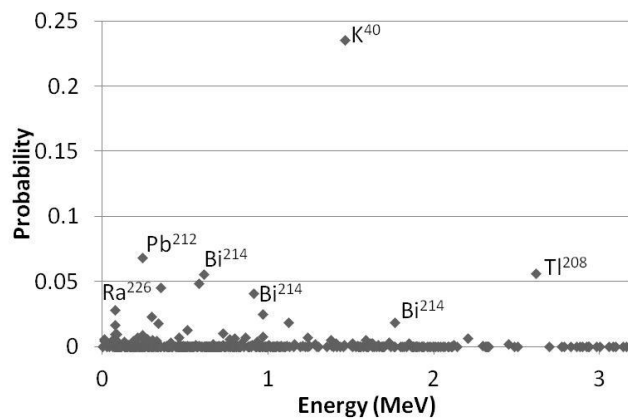


Fig. 2-6. MCNP source term implemented to the background model.

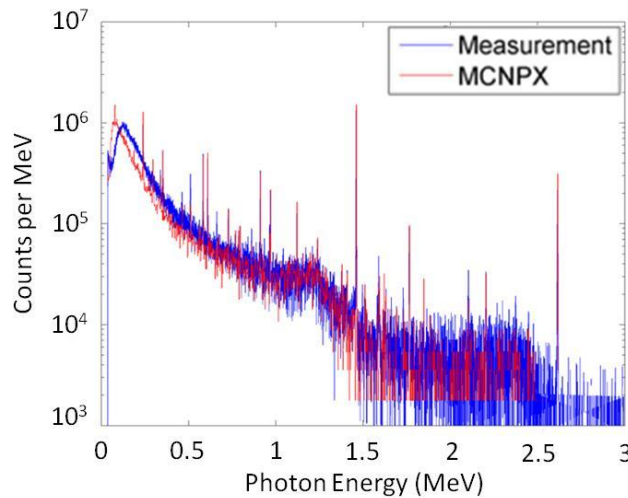
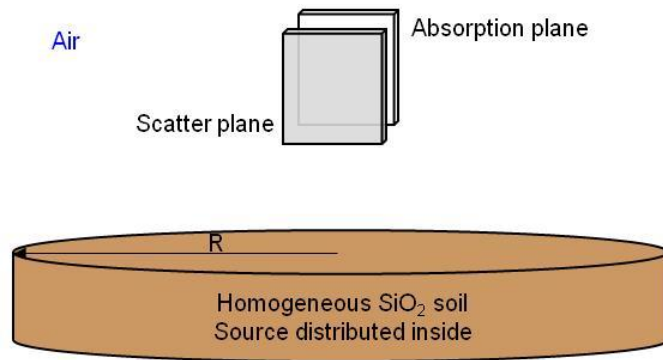


Fig. 2-7. Comparison of simulated and measured background data collected with an HPGe detector. The measured background data was obtained from SNL.

In order to keep the self-shielding effect from the SiO<sub>2</sub> soil cube and scale the background model to a large-scale system, the source was modeled as a volume source set in a large cylindrical

plane of soil as shown in Fig. 2-8. The soil disk needs to be considered as infinite from the point of view of the detection system. This means having a large enough diameter that further increasing its size will not affect the response (single counts) from the detection system; however, increasing its size also increases the computation time needed for a given simulated-measurement time. As such, the size selected was the smallest size at which the system response stops increasing, which was computed to be 12 m.



**Fig. 2-8. Model of the background source. The soil cylinder was located 1 m below the system. The radius R was set to 12 m in the simulations.**

### ***2.3.3. Lanthanum Intrinsic Background Model***

Of the scintillation materials evaluated with this simulation study, LaBr<sub>3</sub> presents the particularity of having its own intrinsic background radiation. This radiation comes from the <sup>138</sup>La isotope, which makes up 0.09% of the weight of natural lanthanum. Modeling this contribution to the response of the detection system is of great importance as the <sup>138</sup>La emits several correlated particles that can be mistaken as source (imageable) events. The <sup>138</sup>La isotope has the decay modes (with a half-life of  $1.02 \times 10^{11}$  years) shown in the following equation:

$$\left\{ \begin{array}{l} {}^{138}_{57}\text{La} \xrightarrow{65.6\%} {}^{138}_{56}\text{Ba} + \bar{\nu}_e + X + \gamma \left\{ \begin{array}{l} E_\gamma = 1436 \text{ keV} \\ E_{X_1} = 37.4 \text{ keV (65\%)} \\ E_{X_2} = 5.7 \text{ keV (31\%)} \end{array} \right. \\ \\ {}^{138}_{57}\text{La} \xrightarrow{34.4\%} {}^{138}_{58}\text{Ce} + \nu_e + \beta^- + \gamma \left\{ \begin{array}{l} E_\gamma = 789 \text{ keV} \\ E_\beta^{\text{max}} = 255 \text{ keV} \\ \bar{E}_\beta = 94 \text{ keV} \end{array} \right. \end{array} \right. \quad (6)$$

The source was modeled by using the MCNPX-PoliMi “single-decay option” that allows radioactive decay to be directly specified as a source term [17].

Once realistic detector responses, including background radiation components, are obtained for the system, events can be correlated and imaged. These two steps correspond to the second row of the flow chart in Fig. 2-5.

#### **2.3.4. Detection of Imageable Events**

The scatter plane was chosen as the trigger for the identification of correlated counts because it receives fewer counts per second than the absorption plane when including the background counts. Given the time resolution of the scintillators used, a pulse from a scattering interaction can sometimes be detected in the front plane after the pulse from the corresponding absorption interaction was detected in the back plane. As a consequence, the time window is centered on the trigger. If only one other pulse occurs in the back plane during the time window, it is paired with the trigger as a correlated count. Therefore, the size of the applied time window will directly affect the number of correlated counts. A study was carried out to determine the optimum width of the correlation window. Fig. 2-9 shows the evolution of the correlated counts rate for a varying correlation window. The ‘Mixed’ component corresponds to correlated events constructed from pulses with different origins, such as a pulse in the scatter plane from the source simulation and a pulse in the absorption plane from the background simulation. The system simulation included a 1 mCi Cs-137 source at a distance of 100 m along with the appropriate

background radiations with a CaF<sub>2</sub>/LaBr<sub>3</sub> camera. The effect of the <sup>138</sup>La intrinsic background was analyzed separately from other sources of correlated counts. Only the correlated counts with a summed energy within ± 10% of 662 keV are shown Fig. 2-9.

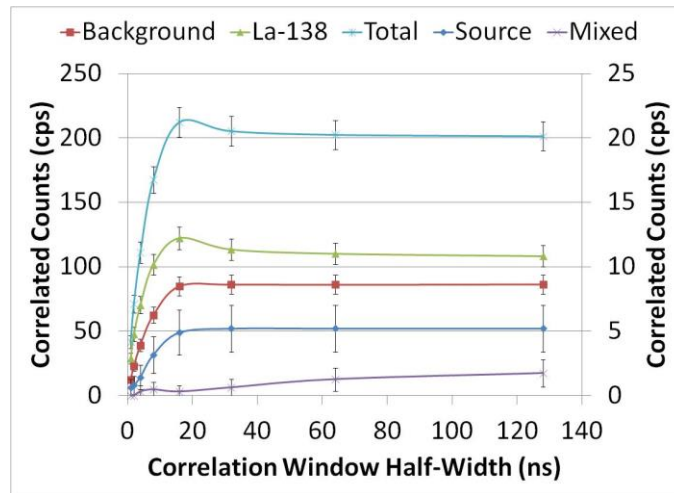


**Fig. 2-9. Number of correlated counts per second for a varying time window half-width with a CaF<sub>2</sub>/LaBr<sub>3</sub> camera. All other systems displayed similar trends. The secondary axis corresponds to the ‘Source’ and ‘Mixed’ curves.**

Fig. 2-9 shows that the number of correlated counts reaches a maximum at approximately 20 ns. Past this value, the number of correlated counts decreases slightly until reaching a plateau at approximately 35 ns. Based on the correlation method used, increasing the correlation window can result in a loss of correlated counts since the likelihood of having multiple counts within the correlation window will increase. This effect affects counts from the <sup>138</sup>La decays which produce multiple correlated particles. A half-width of 50 ns, which is clearly within the plateau seen on Fig. 2-9 and avoids the spike of <sup>138</sup>La correlated counts at lower values, was used in the rest of this chapter. This value will depend on the count rate ‘seen’ by the system. In a high-count-rate environment, the window half-width should be set around the minimum of the plateau, around 35 ns.

### 2.3.5. Backprojection Imaging

After applying all relevant uncertainties and the correlation window described above, the correlated counts are processed using a backprojection algorithm. The axis of the Compton-scattering cone is constructed from the positions of the detectors of interaction (see Fig. 2-2). For each correlated event, the pulse in the scatter plane is assumed to be a single scatter, and the pulse in the absorption plane is assumed to be the subsequent full-energy deposition, regardless of their order. The incoming energy is given by the sum of the two energies deposited. The cone angle is determined using the incoming energy along with the energy deposited in the scatter plane as shown in equation (1). If the equation has a real solution for  $\theta$  (as opposed to a complex number), one cone is created. A window can be specified by the user to restrict the cones being imaged to a specific energy range.

Looking at a point source with a perfect imaging system (no uncertainties on the energy deposition or the system geometry) all cones will intersect at a single point, which is the source location. In a realistic case, however, the source location will not be on the constructed cone most of the time. Therefore, a certain thickness to the cone walls needs to be added, to represent the uncertainties, and the intersection of the volumes created by that thickness will give an approximate source location. The thickness of the cones will have a direct effect on the image, as thicker cones can yield a converged hotspot quicker, while thinner cones will yield a sharper hotspot more accurately linked to the angular resolution of the system.

Our application focuses on the imaging of sources at large standoffs. In this situation, the size of the imaging system is negligible compared to the distance to the source. The system can therefore be simplified to an origin from which cones will be created. A meshed sphere centered on this origin is used to display the overlapping cones. Since the cones are created from the center of the sphere, the radius of the sphere will not affect the image. The cones should then overlap in

the same direction, pointing out the source direction. Similar methods have been applied and validated previously [23].

## **2.4. Results**

The simulation tool enabled us to perform optimization tasks using simple models and F1 surface tallies, to track the photons entering and leaving the detection planes. We also used it to realistically simulate the system to have an indication of the performance of a system prototype. Below are the results that were acquired throughout the duration of the project, presented in chronological order.

### ***2.4.1. Scatter-Plane Optimization***

The scatter-plane optimization was carried out using a model similar to that shown in Fig. 2-2, with a  $1 \times 1 \text{ m}^2$  plane source of mono-energetic photons modeled directly in front of and perpendicular to the scatter plane. Both the scatter and absorption planes are  $1 \times 1 \text{ m}^2$  slabs with a distance of 30 cm between them and surrounded by air. For simplicity, the simulations did not include PMT and electronics models.

Photons incident on the front surface of the absorption plane were tallied by the number of interactions occurring within the scatter plane. The simulations were run for different scatter-plane thicknesses. Fig. 2-10 shows the fractions of photons either reaching the absorption plane uncollided ( $\phi_0$ ), or scattered a given number of times in the scatter plane and reaching the absorption plane: single scatter ( $\phi_1$ ), double scatter ( $\phi_2$ ), and triple scatter ( $\phi_3$ ).



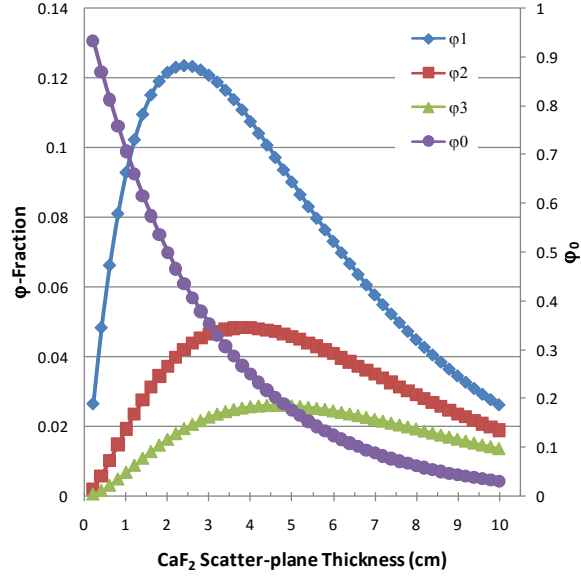


**Fig. 2-10. Uncollided (shown on right axis), single-scattered, and multiple-scattered (shown on left axis) photon flux incident on the absorption-plane; incident photon source energy of 300 keV.**

The uncollided and scattered fractions of 300-keV incident photons are plotted for varying thickness of a CaF<sub>2</sub> scatter-plane in Fig. 2-10. The number of uncollided photons decreases with increasing CaF<sub>2</sub> thickness while the scattered photons peak at different thicknesses (depending on the number of scatters), and then decrease with increasing plane thickness.

Multiple-scatter events in the same detector within a short time (nanoseconds at most) are detected as single-scatter events. They can reduce image quality and introduce error in the estimation of source position. In practice, such events are combined as one pulse in the detector and thus are considered as a single-scatter event by the system. As a consequence, the optimization of the scatter-plane thickness was based on maximizing the occurrence of single-scatter events while minimizing the number of multiple scattered photons. A scatter-plane figure of merit (FOM) was chosen to aid in the selection of an optimum scatter-plane thickness:

$$FOM_S = \frac{\varphi_1^2}{\sum_{i=1}^n \varphi_i} \quad (7)$$

In the equation above,  $\varphi_1^2$  is the square of the single-scatter fraction while  $\varphi_i$  is the  $i^{\text{th}}$ -scatter fraction. Specifically, the FOM is the ratio of the single-scatter events squared to all scattered events [24]. The FOM is plotted for 100-400 keV photons incident on  $\text{CaF}_2$  and  $\text{C}_9\text{H}_{10}$  in Figs. 2-11 and 2-12, respectively. An optimal region can then be defined where the FOM peaks for the different energies. It is shown in blue in Figs. 2-11 and 2-12.

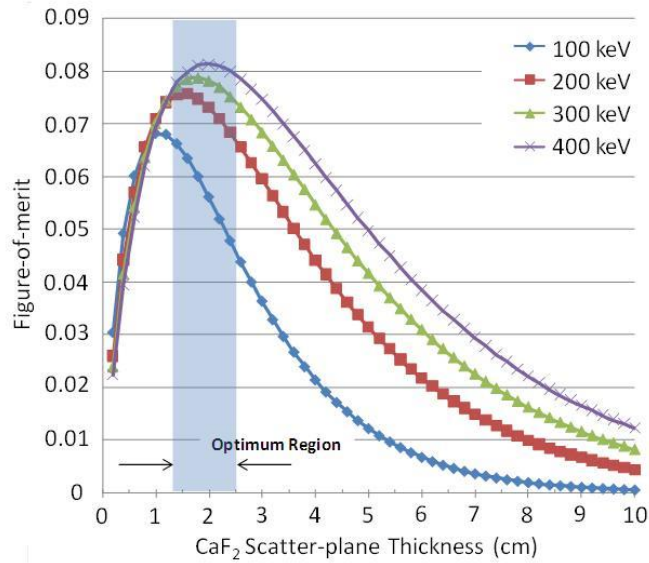


**Fig. 2-11. Figure of merit plotted as a function of  $\text{CaF}_2$  scatter-plane thickness for monoenergetic photons with energies between 100 and 400 keV. A region of optimum scatter-plane thickness can be identified around the peaks of the curves (1.5 to 2.5 cm).**

As we can see when comparing Figs. 2-10 and 2-11, the FOM peaks at a smaller thickness than the single-scattered flux fraction. This result can be quantified by considering the thickness at which the peak in the FOM and single-scatter fraction occur; 1.8 cm and 2.4 cm, respectively, for 300 keV photons (Figs. 3 and 4). Relative to a thickness of 2.4 cm, the single-scatter fraction of a 1.8-cm thick slab of  $\text{CaF}_2$  is reduced by only 3.6%, while the multiple-scatter events are reduced by approximately 23%.

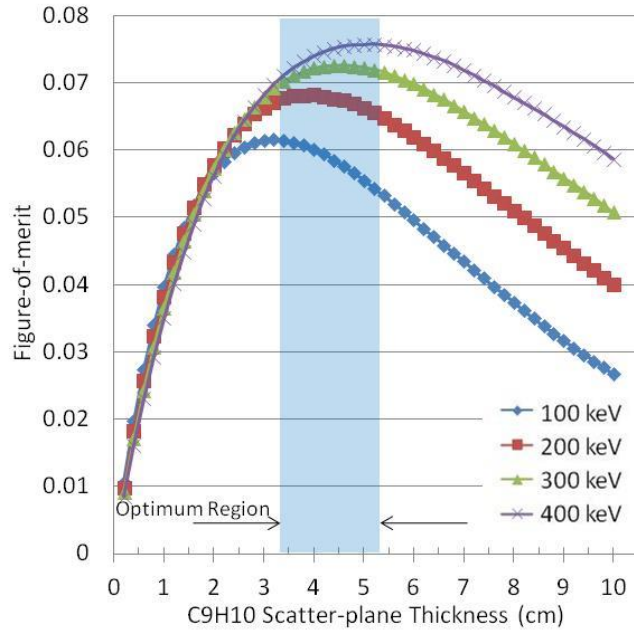


**Fig. 2-12. Figure of merit plotted as a function of  $C_9H_{10}$  scatter-plane thickness for monoenergetic photons with energies between 100 and 400 keV. A region of optimum scatter-plane thickness can be identified around the peaks of the curves (3.3 to 5.3 cm).**

#### ***2.4.2. Absorption-Plane Optimization***

Two parameters were optimized for the absorption plane: the detection efficiency and the angular uncertainty. The efficiency of the absorption plane relies entirely on the probability of a full-energy deposition, through a combination of interactions ending with a photoelectric absorption. The thickness of the plane will have a direct effect on the efficiency. A thicker plane results in degradation of the angular resolution of the system, because uncertainty on interaction location is increased. The cross-sectional size of the detectors will also affect the efficiency as a succession of scatters in one detector could amount to a full-energy deposition, whereas it would result in two pulses if the scatters occurred in different detectors. However, it may be possible to use those multiple-detector events by setting the interaction location in the middle of the two detectors centers.

Various absorption-plane thicknesses were modeled with the intent of quantifying the ratio of photon absorptions to the number of incident single-scattered photons. In these simulations, the

scatter-plane thickness and distance between planes were fixed. A specialized algorithm was utilized to characterize events that underwent a single scatter within the scatter plane and interacted within the absorption plane. Absorption events were considered to be any event depositing energy within the detector that resulted in a full-energy deposition. The planes were divided into separate detectors by the algorithm.

The absorption-plane efficiency  $\varepsilon_{abs}$  is defined as the fraction of the incident single-scattered photons that undergo a full-energy deposition within a single detector. With  $N_a$  being the number of full-energy depositions in the absorption plane and  $\varphi_1$  the once-scattered flux incident on the absorption plane, we have the following equation:

$$\varepsilon_{abs} = \frac{N_a}{\varphi_1} \quad (8)$$

Using a method developed by Ordonez et al. [25], the angular uncertainty associated to the dimensions of the absorption plane was calculated using the following equation:

$$[\Delta\theta]^2 = \frac{1}{R_z^2} [(\Delta x \cos \theta)^2 + (\Delta y \cos \theta)^2 + (\Delta z \sin \theta)^2] \quad (9)$$

In equation (9),  $R_z$  is the interplanar distance (30 cm),  $\Delta x$  and  $\Delta y$  are the detector cross-sectional lengths,  $\Delta z$  is the plane thickness, and  $\theta$  is the angle of the scatter in the front plane, as shown in Fig. 2-13. The angular uncertainty was then averaged over the different possible scatter angles for a source facing the system at a large standoff (100 m).

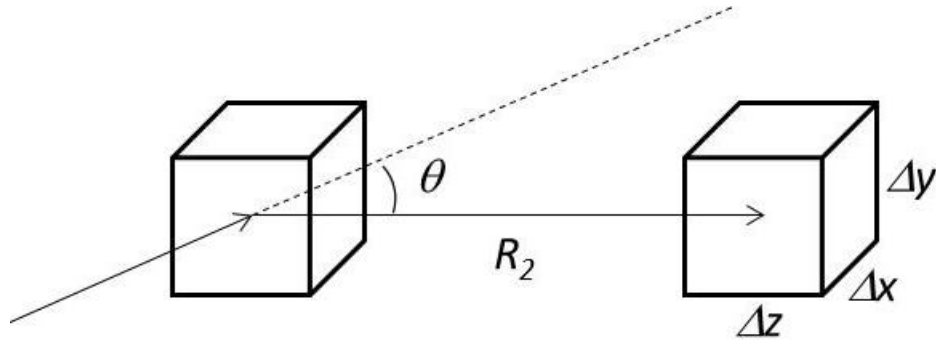


**Fig. 2-13. Illustration of the variables in the calculation used for the angular uncertainty associated to the absorption plane.**

With the efficiency and angular uncertainty defined, a FOM was used to define a region from which the dimensions of an absorption-plane would have a favorable trade-off between the two parameters. An emphasis was put on the efficiency of the system given our application of standoff imaging:

$$FOM_{abs} = \frac{\varepsilon_{abs}^2}{\Delta\theta} \quad (10)$$

Fig. 2-14 shows results for the optimization of a  $\text{LaBr}_3$  absorption plane for 400-keV photons; the combination of both efficiency and angular resolution in the FOM gives us a well-defined optimum region. We can see the cross-sectional size of the detector affects the angular resolution more than the efficiency. Once we have detectors wide enough to contain the colliding particle, the efficiency does not keep increasing while the angular resolution keeps decreasing. This should warrant the use of detectors as small as  $2 \times 2 \text{ cm}^2$ , were it not for cost considerations. The use of smaller detectors results in a larger number of detectors and electronics, making the system significantly more expensive for the same detection volume.

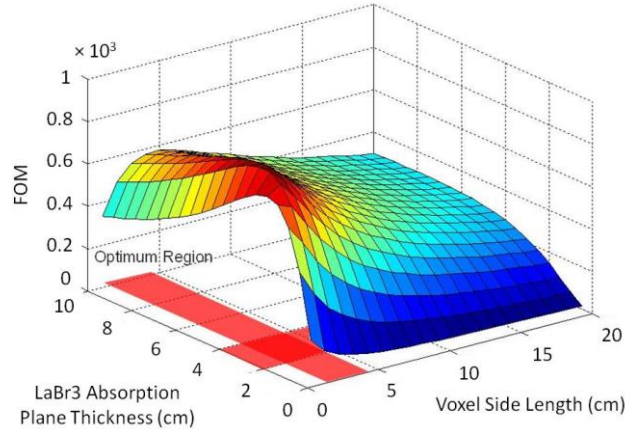


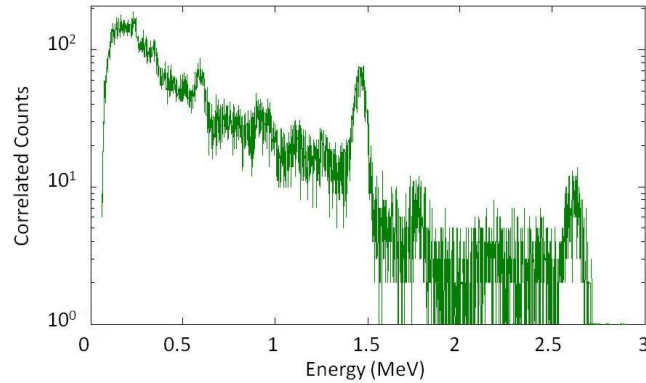
**Fig. 2-14. FOM<sub>abs</sub> plotted for LaBr<sub>3</sub> as a function of thickness and detector side length for 400-keV photons.**

To further work towards a system prototype, we chose standardized detector thicknesses (7.62 cm for C<sub>9</sub>H<sub>10</sub>, 2.54 cm for CaF<sub>2</sub>, 7.62 cm for NaI, and 5.08 cm for LaBr<sub>3</sub>) and set a limitation to the maximum number of detectors in a 1×1-m<sup>2</sup> plane for cost considerations. This resulted in the use of 5.08 × 5.08-cm<sup>2</sup> and 7.32 × 7.32-cm<sup>2</sup> wide detectors in the simulations.

Effort was then put towards obtaining an indication of the minimum detectable activity of a single energy gamma source at a standoff of 100 m. This was performed by analyzing the simulated background.

### ***2.4.3. Minimum Detectable Activity Study***

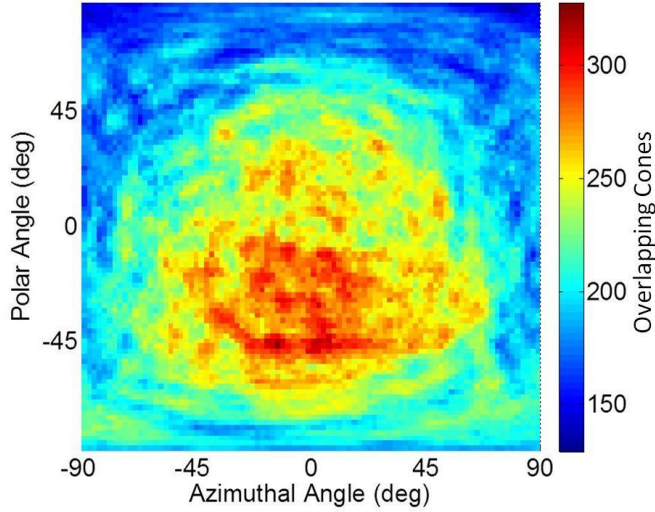
Fig. 2-15 shows the correlated counts generated by the gamma-ray background model presented previously. Gamma-ray sources will most often only have discrete energy distributions (for instance 662 keV for Cs-137) allowing the user to only image the events with a summed energy in an appropriate energy window (SNM emit both multiple decay lines and a continuous distribution of photons).



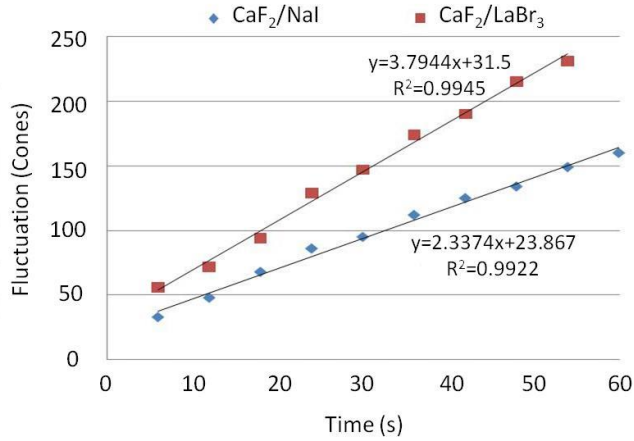
**Fig. 2-15 Energy distribution of the correlated counts produced by background radiation, collected by a CaF<sub>2</sub>/ NaI(Tl) camera. The error bars (on the order of 10 %) were omitted from the plot for clarity.**

Fig. 2-16 shows the backprojection image obtained from the gamma-ray background. The color bar shows the number of cones overlapping in a given mesh point of the sphere. The image presents a higher intensity at negative polar angles, which was expected considering that the background source is located below the system. The feature is also dictated by the geometry of the system, the threshold effect, and the energy gating around 662 keV. The image is not fully converged given the relatively short simulated measurement time of 60 seconds.

This background was then characterized by studying the variation of intersecting cones over the 2- $\pi$  hemisphere in front of the imaging system. The cone fluctuation was defined as the difference between the maximum and the minimum number of intersecting cones in the backprojected image. Fig. 2-17 shows the evolution of the cone fluctuation over 10 seconds increments of simulated measurement time: the increase is linear, as expected. This analysis is important because it allows us to define how the background contributes to the backprojection results.



**Fig. 2-16. Backprojection image of the background with the 662 keV energy window for a  $\text{CaF}_2/\text{NaI}(\text{Tl})$  camera. The simulation was set to mimic a 60 s measurement.**



**Fig. 2-17. Linear fit of the cone fluctuation (with the 662 keV  $\pm$  10% energy window) versus the simulated measurement time. The standard deviations observed ranged from approximately 5 to 15.**

To accurately obtain the source location, a large number of cones created from the source events are needed relative to the number of the background cones. A threshold can be set on the number of cones intersecting in the hotspot to define a minimum detectable activity (MDA). This threshold and the following MDA were inspired from standard MDA definitions [21]:

$$L_C = N_{cf} + 1.645\sqrt{N_{cf}} \quad (11)$$

$$N_D = L_C + 1.645\sqrt{N_D} \quad (12)$$



where  $L_C$  is the threshold,  $N_{cf}$  the background cone fluctuation, and  $N_D$  the minimum number of counts needed for detection. A hotspot with  $N_D$  counts intersecting should then be distinguishable in any position of the half-universe plotted in Fig. 2-16.

The MDA for a 1-minute measurement of a Cs-137 source at 100 m was calculated. A 1 mCi Cs-137 source at 100 m produces 2.1 hotspot cones per second for a  $\text{CaF}_2/\text{NaI}(\text{Tl})$  camera. With the threshold defined previously, using the linear fit to obtain the  $N_{cf}$ , and scaling the 1 mCi Cs-137 case accordingly, the minimum detectable activity within 1 minute is 1.65 mCi. The image of the 1.65 mCi source for a 60 s simulated measurement is shown in Fig. 2-18.

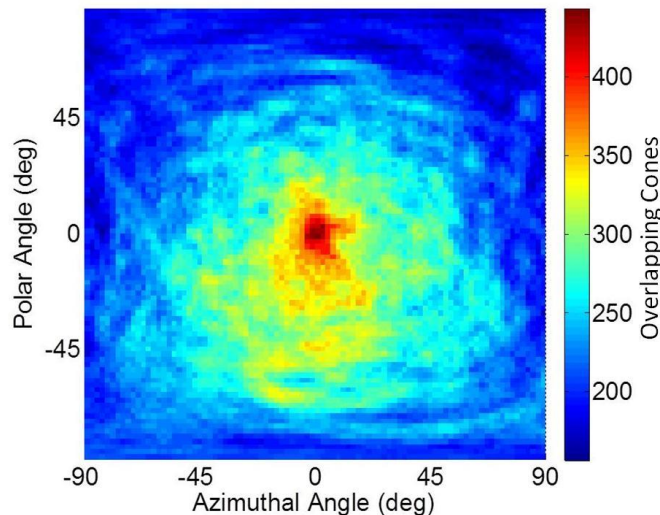


**Fig. 2-18. Image of a 1.65 mCi Cs-137 source centered 100 m in front of the system (including the background). The simulation was set to mimic a 60 s measurement.**

Results for all four camera configurations are shown in Table 2-I. The  $\text{CaF}_2/\text{NaI}(\text{Tl})$  camera yielded the lowest MDA. Replacing  $\text{CaF}_2$  in the scatter plane by  $\text{C}_9\text{H}_{10}$  increased the MDA by  $\approx 0.2$  mCi while replacing  $\text{NaI}(\text{Tl})$  by  $\text{LaBr}_3$  in the absorption plane increased the MDA by  $\approx 0.5$  mCi. The most appropriate materials for a Compton camera are  $\text{CaF}_2$  for the scatter plan and  $\text{NaI}(\text{Tl})$  for the absorption plane. The results also indicate that  $\text{C}_9\text{H}_{10}$  is an appropriate low-cost replacement for  $\text{CaF}_2$ . On the other hand,  $\text{LaBr}_3$  is disadvantageous as its good spectroscopic capability does not seem to overcome the larger cone fluctuation created by the  $^{138}\text{La}$  intrinsic background.

The MDA values shown in the table correspond to a 1 minute simulated measurement of a Cs-137 source located in front of the system. Results for any source position could then be derived from efficiency calculations, computing the relative hotspot cones per second.

**Table 2-I. Results for the different camera configurations.**

	CaF2/ NaI(Tl)	C9H10/ NaI(Tl)	CaF2/ LaBr3	C9H10/ LaBr3
Hotspot cone rate (cps) for a 1 mCi Cs-137 source	2.1 ± 0.1	2.2 ± 0.1	2.4 ± 0.2	2.5 ± 0.2
Cone fluctuation increase (cps)	2.3 ± 0.3	3 ± 0.2	3.8 ± 0.2	4.4 ± 0.3
MDA (mCi)	1.65	1.84	2.18	2.32

For cost considerations, further research was focused on the C<sub>9</sub>H<sub>10</sub> /NaI(Tl) camera with detector cross-sectional sizes increased to 7.62×7.62 cm<sup>2</sup>. With a system selected, advanced imaging methods were investigated.

#### **2.4.4. MLEM – Backprojection Comparison**

A study to investigate two image reconstruction algorithms, backprojection [23] and maximum likelihood expectation maximization (MLEM) [26], was performed with system consisting of two 13×13 planar arrays of 7.62×7.62×7.62 cm<sup>3</sup> square detectors separated by 30 cm. The source modeled was a 1-mCi Cs-137 source located 100 m away from the system. The background radiation model was implemented in the study. The angular space was meshed with 10-degree intervals and the energy spectrum between 0 and 2 MeV was binned with 100-keV steps.

Because our PMTs are not position-sensitive and the energy resolution of our system is not excellent, we can bin our data in an acceptable number of bins without requiring the use of list-mode MLEM. We used a bin-mode algorithm with inputs formatted in 10-degree scatter-angle bins and 100-keV energy bins. The detector coordinates inside the planes were used to calculate axis coordinates, which were subsequently binned. In order to keep the size of the system matrix down, we only used the energy bin of interest in our calculations. The system matrix was calculated using large Monte Carlo simulations, for each point of the angular space mesh. The energy used was the center of the bin of interest, 650 keV.

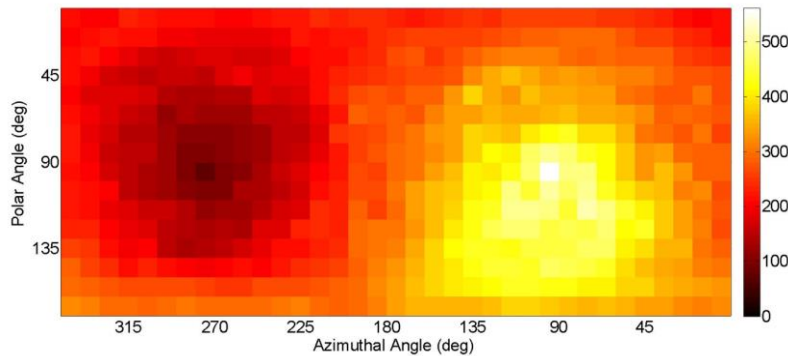


**Fig. 2-19. Backprojection image of the 600-700 keV bin for a 1-min simulated measurement. The angular coordinates of the source are (90°,90°).**

Fig. 2-19 shows the backprojection image obtained from a 1-min simulated measurement. The mesh size was increased to 10°, compared to the 2° mesh of the previous images, to facilitate a direct comparison to later results. The simulated measurement yielded 291 source correlated counts and 4,325 background correlated counts in the 600-700 keV bin. The source is accurately located although the background significantly deteriorates the quality of the image.

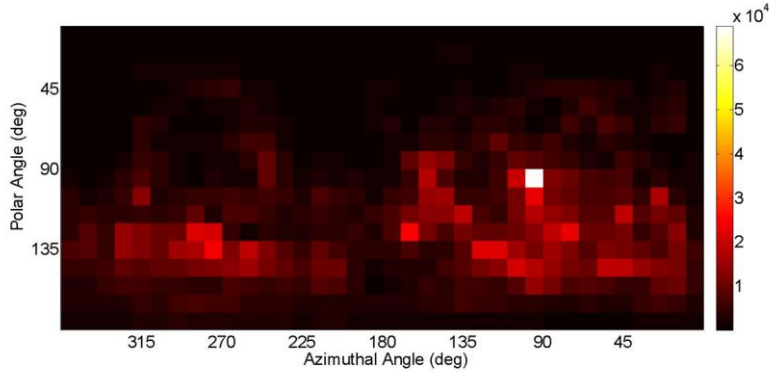


**Fig. 2-20. MLEM image of the 600-700 keV bin for a 1-min simulated measurement after 25 iterations.**

The MLEM reconstruction of the same simulated measurement is shown in Fig. 2-20. As we can clearly see, the background features are reduced and the source can be located more easily. With enough processing power, the MLEM could also be used on all the correlated data (instead of only the 600-700 keV bin shown here), yielding both the accurate source position and its energy.

#### **2.4.5. Validation Measurements**

Validation of the simulation methodology presented was previously carried out with a small-scale prototype system. The prototype consists of two 2×2 planes of scintillators. The scatter plane is made up of four  $\text{Ø}7.62 \times 7.62 \text{ cm}^3$  cylindrical EJ-309 liquid organic scintillators instead of the  $\text{C}_9\text{H}_{10}$  used in the iFind project. The absorption plane is made up of four  $\text{Ø}7.62 \times 7.62 \text{ cm}^3$  cylindrical NaI scintillators. The two planes are separated by 10 cm. A 20 minute measurement was performed using a 30- $\mu\text{Ci}$  Na-22 source positioned to the front-left of the system, as shown on Fig. 2-21.

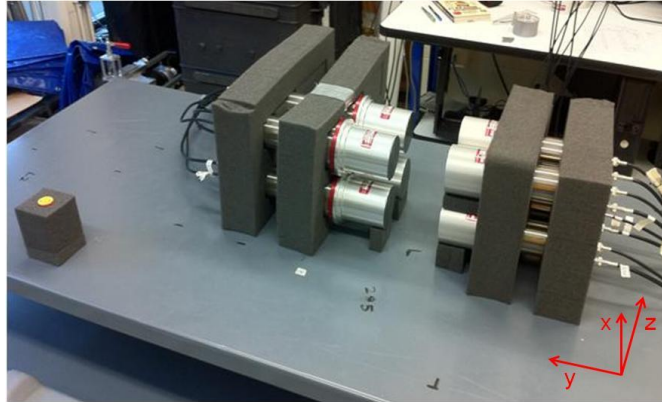


**Fig. 2-21. Measurement setup with a Na-22 source at  $x=-30$  cm,  $y=50$  cm, and  $z=0$  cm. The origin of the coordinates is at the center of the front face of the scatter plane.**

The hardware used to acquire the data was an 8-channel, 12-bit, 250-MHz digitizer (CAEN V1720). The trigger for acquisition over all channels was set on the four channels of the absorption plane with a 70-keV threshold, and “empty” waveforms were filtered out (zero suppression) to minimize data-collection waste. The zero-suppression technique is based on deleting waveforms below a given threshold after a trigger: The same 70-keV threshold is used on non-trigger waveforms in the absorption plane, while a 10-keV threshold is applied to the scatter-plane waveforms. PMT voltages were set to obtain the same gain for all the detectors, yielding a dynamic range maximum value of 2.14 MeV.

The waveforms collected were processed off-line with a MATLAB script. The script applies pulse shape discrimination to the scatter-plane pulses to remove the background neutron counts, extracts time and pulse height information from the waveform, and converts the pulse height to keV. The output of the MATLAB script is formatted as a detector response, similar to the one processed in the simulations. This output can then be used with our data-analysis algorithm to correlate counts and image the source.

The same system setup was then modeled using MCNPX-PoliMi and compared to the measured results. The background radiation model was omitted given the strength and proximity of the Na-22 source. The comparison shown in Fig. 2-22 confirms the validity of the simulation

methodology as the same features can be distinguished in both images. Only 511-keV photons were simulated. The large difference in the intensity shown on the image derives from an inaccurate PMT model which has since been improved, and will be discussed in chapter 5, and a large amount of noise from the NaI(Tl) which was reduced with the use of a pulse shaper. In both images, the source can easily be located from the image hotspot.

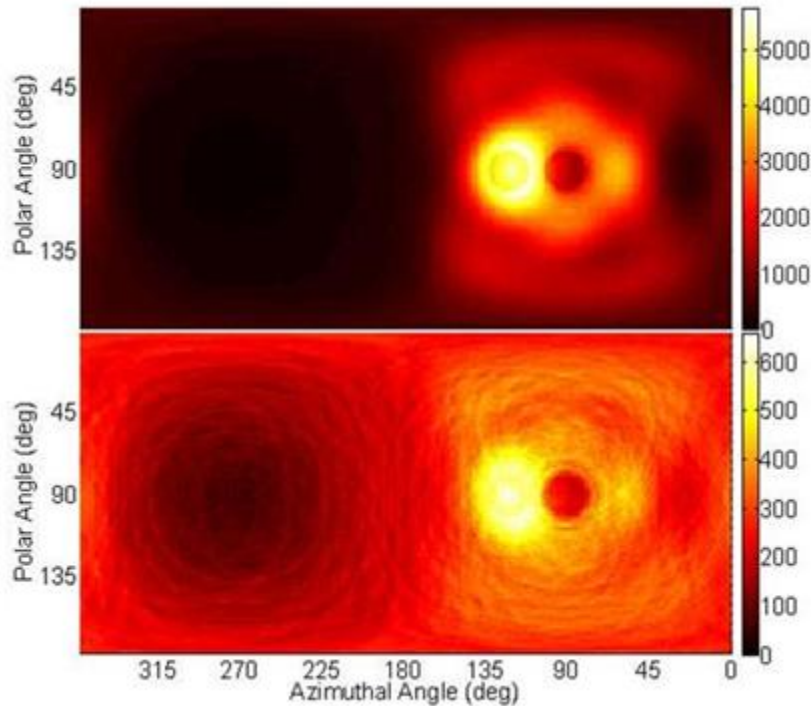


**Fig. 2-22. Comparison of backprojection images from simulated (top) and measured (bottom) data. Only energies between 400 and 600 keV were imaged. The angular coordinates of the source are (121°,90°).**

## 2.5. Advantages and Limitations of Compton Imaging

In this chapter, I introduced a new simulation and optimization methodology for two-plane Compton cameras using the MCNPX-PoliMi code. The methodology was used to assess the performance of preliminary Compton-camera designs. Validated background data were implemented in the simulations along with appropriate detector parameters and uncertainties. A data-analysis software was developed and a backprojection imaging algorithm was used to enable

comparison of the different cameras investigated. This methodology was particularly helpful for our application as the building of a large-scale prototype for long distance imaging would come at a significant cost.

The simulation methodology was used to evaluate four types of scintillation detectors including  $C_9H_{10}$  and  $LaBr_3$ . It was shown that  $C_9H_{10}$  is an adequate scatter-plane material (especially considering the low price and availability), while the superior energy resolution of  $LaBr_3$  did not offset its cost and intrinsic background radiation to warrant use in a large-scale camera. Based on the simulation results, the best Compton-camera material configuration (outside of price considerations) was found to be  $CaF_2/NaI(Tl)$ . The  $C_9H_{10}/NaI(Tl)$  camera was selected for further research due to lower cost. Backprojection and MLEM were investigated, with MLEM greatly reducing background features.

The iFind project offers a relatively low cost photon imaging option for nuclear-nonproliferation applications. However, it presents some limitations. As we have seen throughout the backprojected images in this chapter, background can greatly impair the quality of the image, and thus, the localization of a source. Another drawback that was not discussed in this chapter is the ease of shielding photons using lead. Assuming a threshold of 20 keV in both planes and a 2-MeV photon source, the number of detectable photons will decrease by an order of magnitude per inch (2.54 cm) of lead shielding. While those issues are not avoidable when imaging photon sources, SNM also emits neutrons, which are much less affected by background radiation, as neutron background is negligible.

## Chapter 3. Neutron Imaging

### 3.1. Premise

Localizing SNM is of particular interest in nuclear nonproliferation efforts. Using photon detection exclusively to locate or characterize SNM has been shown to have its drawbacks. The impact of background radiation on the photon imaging system is non negligible and high-Z material such as lead can effectively shield photons. The imaging system presented in chapter 2 is also not ideal for low-energy photons such as those emitted by  $^{239}\text{Pu}$  and  $^{235}\text{U}$ . As such, in situations where heavy shielding can be used without prompting suspicion, an alternative to photon imaging is necessary. Neutron imaging is a good candidate, since neutrons are less affected by high-Z shielding and they are one of the characteristic emissions of SNM. Neutron imaging seems particularly well-suited to carry out tasks involving SNM.

Three main technologies are currently investigated in fast neutron imaging: neutron-scatter cameras relying on the elastic scattering of neutrons on hydrogen [9], coded apertures with a mask built to shield neutrons [27], and time-encoded imaging, which relies on a moving component [28]. Sandia National Laboratories have been actively working on these technologies, and each presents various advantages and drawbacks. Typically, time-encoded imaging has the highest detection efficiency but the worse angular resolution. On the other hand, neutron-scatter cameras have the lowest efficiency but better angular resolution, as well as spectroscopic capabilities. Coded apertures have a higher efficiency and resolution than neutron-scatter cameras but carry



less position information per single event. For a coded aperture, a single event will have its possible source locations dictated by the mask used, while for a neutron-scatter camera, the possible source locations will be a single cone.

Building upon the iFind project presented in chapter 2, I started conducting research on neutron-scatter cameras as it follows similar principles to a Compton camera. The aim of this work was to acquire experience in processing neutron events, with the focus on combining both imaging systems into one.

### 3.2. Neutron-Scatter Camera Concept

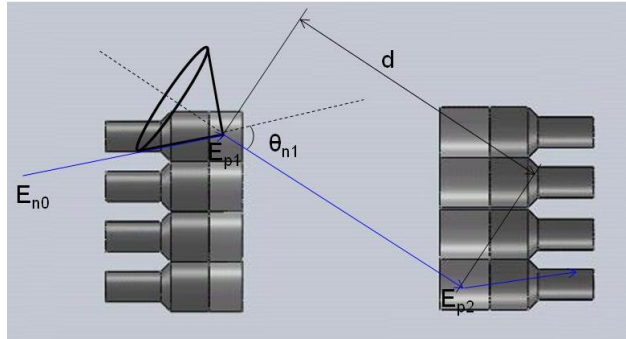


**Fig. 3-1. Schematics of a neutron-scatter camera with a neutron event depicted and the associated backprojection cone.**

Neutron-scatter imaging is similar to Compton imaging, relying on the detection of an elastic scatter on hydrogen instead of a Compton scatter. The physics of neutron elastic scattering relates the angle of the scatter to the energy of the incoming neutron and the energy of the recoil proton [9]. The principle applied to a two-plane camera design is shown in Fig. 3-1. The equation linking the angle to the energies of the particles is as follows:

$$\cos^2 \theta_{n1} = \frac{E_{n1}}{E_{n0}}, \quad (13)$$

where  $\theta_{n1}$  is the scattering angle,  $E_{n0}$  is the incoming neutron energy, and  $E_{n1}$  is the remaining neutron energy after the scatter. A neutron event, with the corresponding energies and

angles is shown in Fig. 3-1. The axis of the cone of probable source locations is given by the interaction positions, while the energy of the neutron after its first scatter is calculated using the time of arrival (time of flight; (TOF)):

$$E_{n1} = \frac{m_n}{2} \times \frac{d^2}{TOF^2}, \quad (14)$$

where  $m_n$  is the rest mass of a neutron and  $d$  is the distance traveled by the neutron between interactions. The detectors used throughout this work are not position sensitive, so  $d$  is simplified to the distance between the centers of the detector cells where the interactions take place. The incoming neutron energy can be calculated from the energy after the first scatter and the energy deposited in that scatter. Because the second interaction is only used for timing and position purposes, it is not required for it to be a scatter off of hydrogen.

### 3.3. Tools and Methodology

While the experience obtained on Compton cameras was very helpful in getting research started on neutron-scatter cameras, a few important issues required particular attention to make the transition. Specifically, a focus was put on how to model neutron sources and neutron interactions in the detector cells, as well as taking the timing of neutrons into account for our correlation algorithm.

The “single-decay option” that was introduced in chapter 2 is a small part of the extensive library of correlated sources available in MCNPX-PoliMi [17]. Various spontaneous-fission and (alpha,n) sources are available to the user. All those sources emit multiple particles per history, with each MCNP history corresponding to a decay event. The particles are correlated according to empirical models, with the number of emitted neutrons and photons randomly sampled in the

multiplicity distribution of the simulated source material. The directions of the particles emitted are also sampled from a pre-defined distribution based on the chosen model.

Photon production from neutron interactions is also associated to the interaction type, as opposed to standard MCNP which produces photons for all neutron interactions (including neutron elastic scattering). This ensures a more realistic event-by-event particle-transport simulation, which is particularly desirable for an imaging system.

Another aspect of neutron modeling that is required for realistic simulations is the scintillation response to neutron interactions. In organic scintillators, neutrons interact with protons that then deposit some amount of the received energy to the scintillator's electrons via excitation and ionization. Recoil protons deposit their energy much more densely than recoil electrons, resulting in an ionization quenching effect that reduces the number of singlet excited states that decay in a light-producing manner [29]. This quenching effect is even stronger for neutron scatters on carbon, resulting in very small pulses (compared to the energy deposited). These pulses are not further discussed in this work, as they are less likely than scatters on hydrogen for neutron energies below 5 MeV, and unused for image reconstruction. While the overall pulse height is reduced, the quenching effect leaves the triplet states and thus the tail component of the pulse largely unchanged (compared to electron recoil pulses). This effect has the benefit of differentiating neutron pulses from photon pulses, but the drawback of yielding a non-linear relation between the energy deposited and the pulse height collected. Pulse-shape discrimination (PSD) will be further described in chapter 4. In order to simulate accurate pulse height distributions (PHD) from organic scintillators, this energy-to-light conversion is carried out in the post-processing of MCNPX-PoliMi simulations. The conversion occurs just before combining interactions within the pulse generation time into a pulse.

Neutron-scatter imaging requires the incoming energy of the neutron, which is the sum of the energy deposited in the first interaction, and the remaining energy, calculated by TOF. As such, the energy deposited must be derived from the pulse height. This energy information is acquired by reversing the relation between light output and energy.

Four different functions have been used throughout my Ph.D. research [30]. The first function used was a binomial form with 3 coefficients:

$$L = aE^2 + bE + c \quad (15)$$

It was inverted in the following form to obtain the energy deposited from the pulse height:

$$E = \frac{\sqrt{b^2 - 4a(c - L)} - b}{2a} \quad (16)$$

The second function was an exponential form with 3 coefficients:

$$L = aE + b(1 - e^{cE}) \quad (17)$$

This form could not be inverted without the use of a lambert W function which had to be implemented in an iterative way.

$$E = \frac{c(L - b) - aW\left(-\frac{bce^{\frac{c(L-b)}{a}}}{a}\right)}{ac} \quad (18)$$

with W the lambert W function defined as such:

$$z = W(z)e^{W(z)}, \quad \forall z \in \mathbb{C} \quad (19)$$

The third and fourth functions are physical fits from Birks [29] and Voltz [31] which rely on the calculation of an integral using the proton stopping power. Birks's form is:

$$L = \int_0^E \frac{S}{1 + kB \frac{dE}{dx}(E)} dE \quad (20)$$

While Voltz's form is:

$$L = \int_0^E S \left( (1 - F) e^{-kB(1-F)\frac{dE}{dx}(E)} + F \right) dE \quad (21)$$

with S linked to the gain of the operated detector, kB linked to the quenching of the detection material, and F the fraction of deposited energy that gets turned to light without being subject to the ionization quenching. These forms were implemented as pre-calculated look-up tables that can be easily reversed.

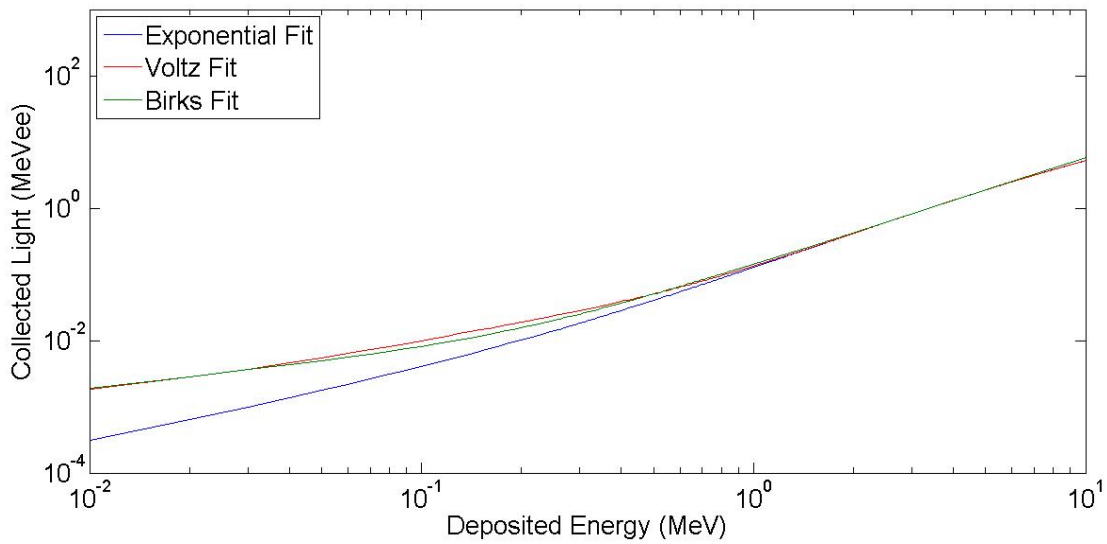


**Fig. 3-2. Various fits of the light output for neutron energy deposited.**

Fig. 3-2 shows the various fits investigated and Fig. 3-3 shows the results from a simple one-detector simulation with the 3 latest fits [32].

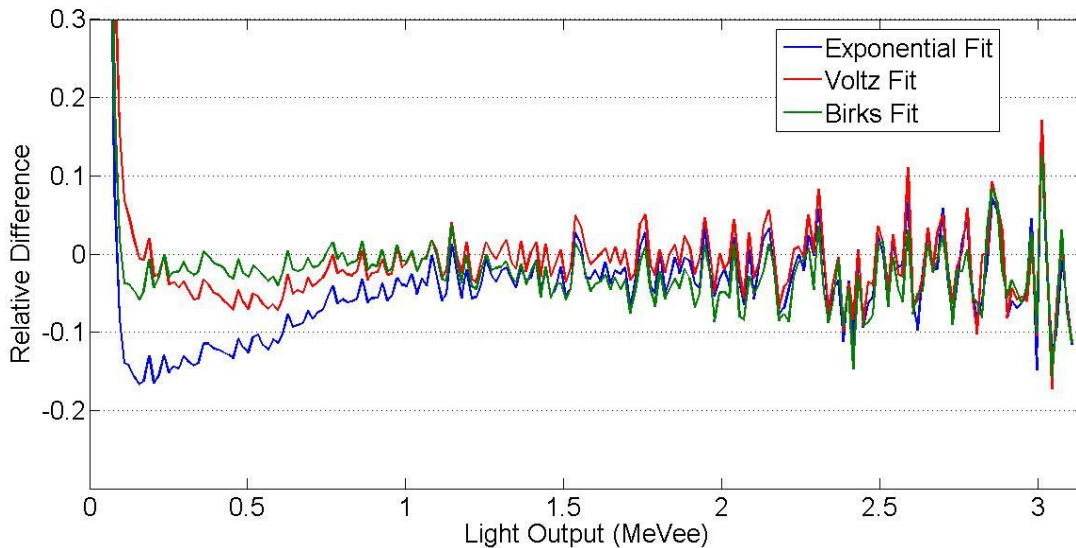


**Fig. 3-3. Relative difference between simulation and measurements of a Cf-252 source**

Once the neutron sources were modeled appropriately and the physics of the neutron interactions were taken into account, the final aspect of data analysis to investigate was timing. While photons travel at the speed of light, neutrons are much slower, with their velocity proportional to their energy. As a consequence, neutrons required a modification of the correlating window. The photon window was centered on one of the interactions because the time resolution of the detectors is too low to account for the TOF of the photon between the two planes. Neutrons have a lower velocity, so the window can be started after the first interaction. An additional window is opened in the front plane to discard any double scatter events that are not as useful for reconstructing the source(s) location.

### 3.4. Simulation validation

In order to verify the accuracy of the MCNPX-PoliMi neutron simulations and the data post-processing described in chapter 2, a small-scale neutron-scatter camera was constructed using 8 EJ-309 liquid scintillators. The small-scale system was modeled using MCNPX-PoliMi and measured and simulated data were processed using the same post-processing algorithm.

### 3.4.1. Measurement Setup

The system set up also included a third plane of NaI(Tl), as shown in Fig. 3-4, which will not be discussed in this chapter. The distance between planes 1 and 2 was set at 43.18 cm to accommodate for the PMTs, electronics and cables of plane 2. The distance separating detectors within a plane was 3.81 cm. The detector signals were collected directly from the PMTs with waveform digitizers. The detectors were calibrated to have a dynamic range of 20 keVee to 2.73 MeVee. A low threshold is important to detect events from a source facing the system as correct events will most likely be low-energy scatters. However, accurate PSD is not possible at pulse heights below approximately 50 keVee, so we expect non-negligible particle misclassification, the effect of which should be decreased when detecting time-correlated particles.

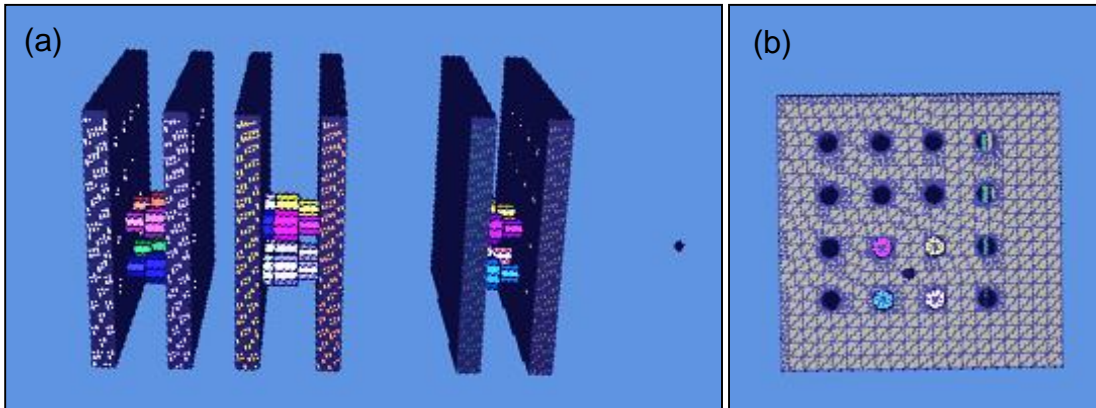


**Fig. 3-4. Side (a) and front (b) views of the MCNPX-PoliMi model of the small-scale prototype and the source location.**

Pulses were collected and processed to obtain the same information obtained from simulations. The pulse height is originally obtained in Volts, and then converted to light output based on the calibration carried out before measurements are taken. The global time information is obtained from the time information carried by the digitizer and constant fraction discriminator (CFD) applied to the pulses collected. Finally, the particle type is set to photons for NaI pulses,

and is obtained by charge integration PSD for the EJ-309 pulses. The list obtained can then be processed by the same algorithm as the simulated data.

### ***3.4.2. Results Comparison***

The 10-h measurement yielded 53,188 correlated neutron counts. A 10-h background measurement yielded 128 correlated neutron counts, a negligible amount compared to the source measurement. The corresponding simulation yielded 64,037 correlated neutron counts. This accounts for a 21% overestimation of the neutron counts. This overestimation can be explained by the absence of the glass window in the detector simulation models (the glass window is located between the PMT and the liquid scintillator to ensure good light transmission when the detector is aimed downwards and the air bubble locates itself between the liquid and the PMT).

Fig. 3-5 shows the reconstructed energy spectra of the validation measurement and simulation. We can see overall good agreement between the measured and simulated data with some discrepancies at low energies. The simulated neutron spectrum stays within  $\pm 50\%$  boundaries of the measured neutron spectrum. The discrepancies between the neutron spectra are due to misclassified particles: some low-energy neutrons are misclassified as photons while some photons are misclassified as higher-energy neutrons due to their faster TOF. This is expected since low thresholds (20 keVee) were applied to the EJ-309 detectors to maximize the collection of low-energy scatters. Further improvements in PSD techniques would improve this result [33].



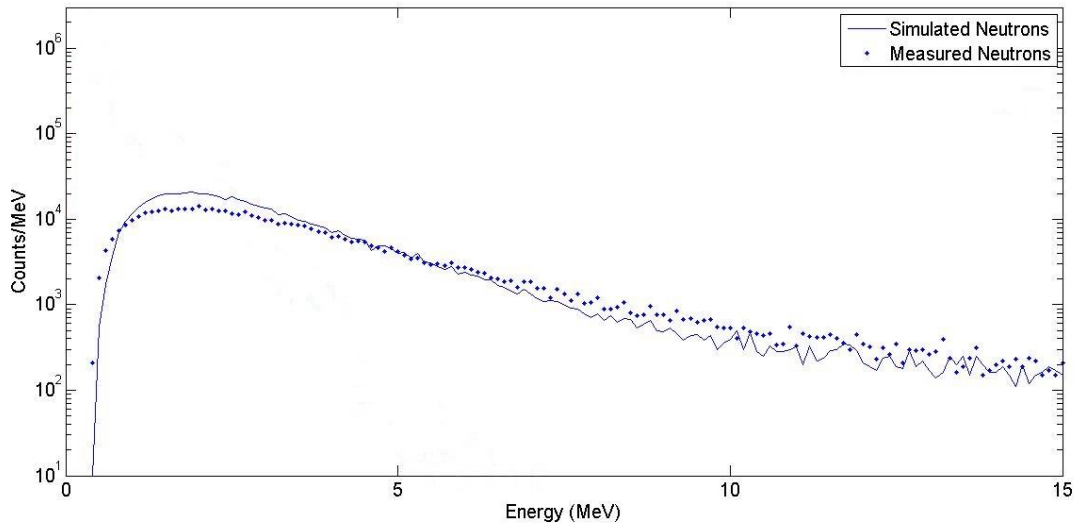


**Fig. 3-5. Reconstructed energy spectra obtained from a Cf-252 source for a 10-h measurement and the corresponding simulation. Error bars were omitted as they were indistinguishable from the data points.**

Fig. 3-6 shows the comparison between the neutron backprojection images. While the source seems positioned higher in the measured image, the same features are noticeable in the measured and simulated images. The overestimation from the simulation is on par with that seen on the energy spectrum, due to the model discrepancy and the PSD imperfections.

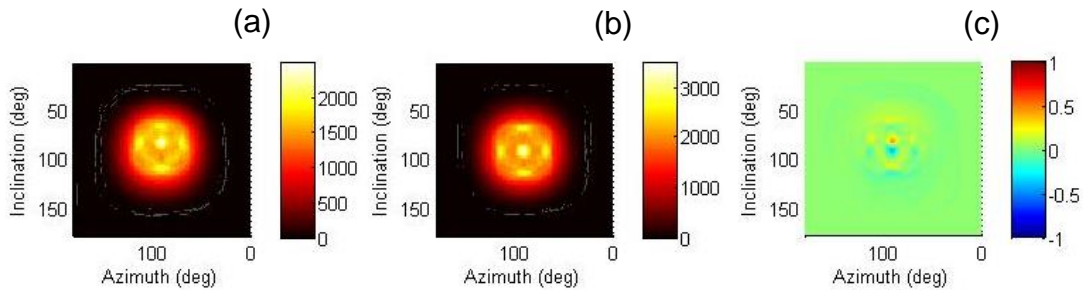


**Fig. 3-6. Backprojection images of all neutron counts obtained from a Cf-252 source for a 10-h measurement (a), the corresponding simulation (b), and difference between both images normalized to their maximum intensity (c).**

A more in-depth comparison of these images can be carried out by investigating the difference between the measured and the simulated images as shown in Fig. 3-6c. The difference was obtained from images normalized to their maximum. This enables us to clearly see the small

shift to lower inclination (higher position) present in the measured images which is due to the relatively large uncertainties on the positions of the different elements of the measurement setup.

### 3.5. Advantages and Limitations of a Neutron-Scatter Camera

Neutron imaging has been actively researched and has proven itself as an alternative to Compton imaging when dealing with neutron-emitting sources [9, 27, 28]. The relatively weak neutron background enables neutron imaging systems to locate sources with a relatively low number of counts [34]. This advantage is unfortunately offset by the fact that neutron signals are usually lower intensity than photon signals (a Cf-252 source emits approximately twice as many photons as neutrons).

Effectively shielding neutrons requires different materials than shielding photons. Photons can be shielded effectively by a relatively thin layer of a high-Z material, such as lead, while neutrons can be shielded effectively by large quantities of low-density hydrocarbons, such as polyethylene. Table 3-I illustrates how shielding affects neutrons and photons. As such, depending on whether volume or weight is a limiting shielding factor, evading detection could prove easier for one type of particle or the other.

**Table 3-I. Decrease, by order of magnitude, of the number of detectable particles for an added inch of shielding.**

	<i>2-MeV Neutrons</i>	<i>1-MeV Photons</i>
Lead	0.01	0.8
Polyethylene	0.25	<0.01

The main limitation of neutron imaging is that, while neutron sources always emit photons, photon sources do not emit neutrons. In the case of SNM, all uranium isotopes have low neutron-emission rates and would, as a consequence, be relatively difficult to detect using (and easy to shield against) neutron detection techniques alone.

We can see that the advantages and limitations of neutron and photon imaging are very complementary. Rather than settle for an alternative to Compton imaging, this investigation of neutron imaging yielded tools that enabled me to work towards a system combining a neutron-scatter camera and a Compton camera.

## Chapter 4. Dual Particle Imaging System

### 4.1. Premise

To monitor the flow of materials of interest and to detect undeclared SNM activities, extensive research has been conducted on various types of suitable detectors and detection systems [9, 35 – 38]. Among those detection systems, photon- and neutron-imaging systems have the advantage of locating radiation sources in complex background environments. Photon imaging is a commonly used technique for standoff detection of radioactive sources with a particular focus on coded apertures [36]; however, photons can be shielded with high-Z material and naturally occurring background radiation is composed primarily of photons. Therefore, neutron imaging has been extensively researched as a technique to further improve detection of SNM, especially in a strong and/or temporally variant photon-background environment [9, 37]. A combination of photon and neutron imaging systems is particularly appealing because neutron imaging also has some disadvantages: materials usually yield significantly fewer neutrons than photons, and neutrons can be shielded with low-Z material.

Spectroscopy is also of particular interest, as being able to characterize a source will allow the user to adjust his response accordingly (e.g. the detection of SNM will be more scrutinized than the detection of common isotopes). This is a particular advantage that a neutron coincidence system will have over a coded aperture. Compton and neutron-scatter cameras both require full-energy information to correctly reconstruct the event, while coded apertures can use any detected interactions to image a source. This is highlighted in Table 4-I which shows the expected

capabilities of the three imaging technologies introduced in chapter 2 in different desirable capabilities. As shown in the table, the DPI system aims at versatility and robustness.

**Table 4-I. Expected performance of imaging methods in different desirable capabilities.**

Imaging Method	Imaging			Spectroscopy		
	Field of View	Efficiency	Event Angular Resolution	System Angular Resolution	Neutron	Photon
Coincidence Imaging (DPI)	good	bad	good	average	yes	yes
Coded Aperture	average	average	bad	good	unlikely	possible
Time-Encoded Imaging	average	good	bad	bad	unlikely	possible

In this chapter, I investigate a transportable DPI system for imaging SNM and other radiation sources. Such a system could be transported in a vehicle to areas of interest where it would then image and characterize the source(s) of radiation. The system is capable of imaging and characterizing neutron and photon sources simultaneously; the combination of those capabilities is particularly desired when dealing with shielded SNM.

#### 4.2. Three-Plane Dual-Particle Imaging Concept

The DPI system described in this chapter uses the concepts of a Compton camera [11] (to image photons) and a neutron-scatter camera [9] (to image fast neutrons) in a single instrument. Few other systems able to image photons and fast neutrons have been researched [10, 38].

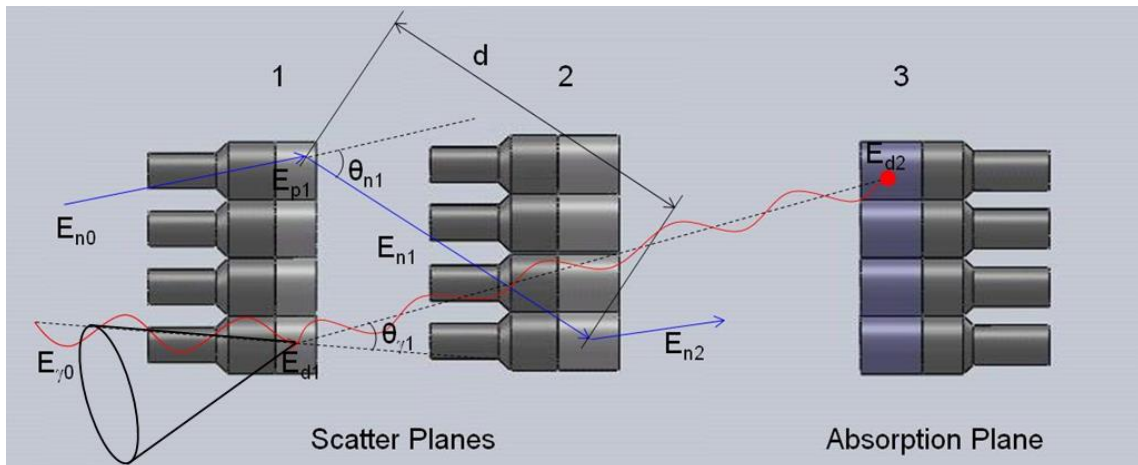
The intrinsic principles of a Compton camera have been explained in chapter 2. Various Compton-camera designs have been explored, but they all use the same underlying physics. Fig. 4-1 shows this three-plane imaging system, which is related to two designs: two-plane and three-plane Compton cameras. In two-plane Compton cameras, source photons are scattered by the front

(scatter) plane into the back (absorption) plane. As a consequence, it is preferred to use a low-Z material in the front-plane detectors, and a high-Z material in the back-plane detectors.

In three-plane Compton cameras, events require source photons to scatter once in each plane [39]. This method has the advantage of not requiring a full energy absorption to find their incoming energy; however, the two required scattering events coupled with another interaction (scatter or absorption) are less likely to be recorded (double coincidence). This is especially the case for low-energy photons which will need to have 3 energy depositions above threshold to be imaged. The system's detection efficiency is decreased when the number of required coincident interactions is increased. The incoming energy can be calculated using the Compton equation:

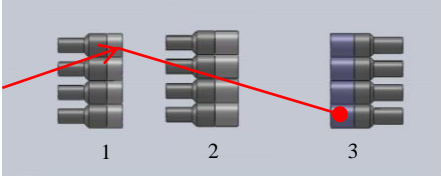
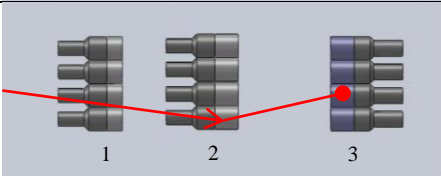
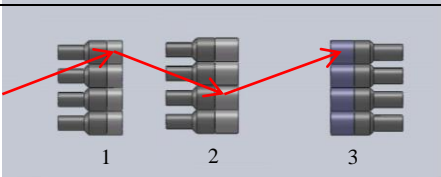
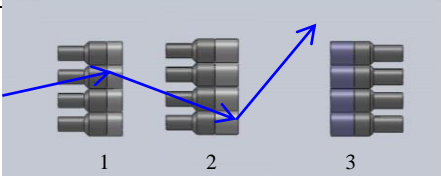
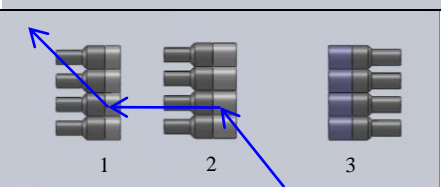
$$E_{\gamma 0} = E_{d1} + \frac{\sqrt{E_{d2}^2 + \frac{4m_e c^2 E_{d2}}{1 - \cos \theta_{\gamma 2}} - E_{d2}}}{2}, \quad (22)$$

where  $E_{\gamma 0}$  is the incoming energy,  $E_{d1}$  the energy deposited in the first plane,  $E_{d2}$  the energy deposited in the second plane,  $\theta_{\gamma 2}$  the second plane scatter angle, and  $m_e c^2$  the energy of an electron at rest.



**Fig. 4-1. Schematics of the DPI system, showing a photon type 1-3 event and a neutron type 1-2 event, along with the information used for image reconstruction. A backprojection cone is illustrated for the photon event.**

The principles of neutron-scatter imaging rely on single neutron scatters on hydrogen, as described in chapter 3. This warrants the use of liquid or plastic scintillators (both low- $Z$  materials) in a neutron-scatter camera. These materials also fit the requirements of the front plane of a two-plane Compton camera given their relatively high Compton scattering cross-sections. As such, the addition of a material with a high photoelectric-absorption cross-section behind the two planes of a neutron-scatter camera constitutes an adequate Compton camera.

	<p><b>Photon-Event Type 1-3</b>            Single Compton scatter in plane 1            Full-energy absorption in plane 3</p>
	<p><b>Photon-Event Type 2-3</b>            Single Compton scatter in plane 2            Full-energy absorption in plane 3</p>
	<p><b>Photon-Event Type 1-2-3</b>            Single Compton scatter in plane 1            Single Compton scatter in plane 2            Interaction in plane 3</p>
	<p><b>Neutron-Event Type 1-2</b>            Single elastic scatter in plane 1            Interaction in plane 2</p>
	<p><b>Neutron-Event Type 2-1</b>            Single elastic scatter in plane 2            Interaction in plane 1</p>

**Fig. 4-2. List of all events measurable with the DPI system.**

The resulting imaging system, shown in Fig. 4-1, can be used to record the five different types of events listed in Fig. 4-2. The photon-event types 1-3 and 2-3 correspond to the standard two-plane Compton-camera counts, while the photon-event type 1-2-3 corresponds to a three-plane Compton camera event. The two different types of neutron events are necessary to image the full  $4\pi$  universe surrounding the system as the largest neutron scatter angle for a single

interaction on hydrogen is 90 degrees (full-energy loss). The photon-event type 2-3 counts are expected to be the most numerous, while photon-event type 1-3 counts are expected to yield finer superior source direction information, and photon-event type 1-2-3 counts are expected to be low probability events.

The materials selected for this system are EJ-309 liquid scintillators for the scatter planes, and NaI(Tl) for the absorption plane. The plane thicknesses for similar materials (C<sub>9</sub>H<sub>10</sub> and NaI(Tl)) in a two-plane Compton camera have been investigated in chapter 2. Given the chapter 2 study, possible plane thicknesses were narrowed down to 5.08 and 7.62 cm for plane 2, and 7.62 cm for plane 3. This new study was focused on maximizing the number of type 1-2 neutron counts using a distance of 20 cm between each plane. A simplified system geometry, with full planes of detection materials, was modeled in MCNPX-PoliMi. A preliminary study was carried out by tallying the neutron flux entering plane 2 with collision bins. Fig. 4-3a shows that the optimized plane 1 thickness is located in a range of 2 to 5 cm. Standardized sized of 2.54 and 5.08 cm were further investigated.

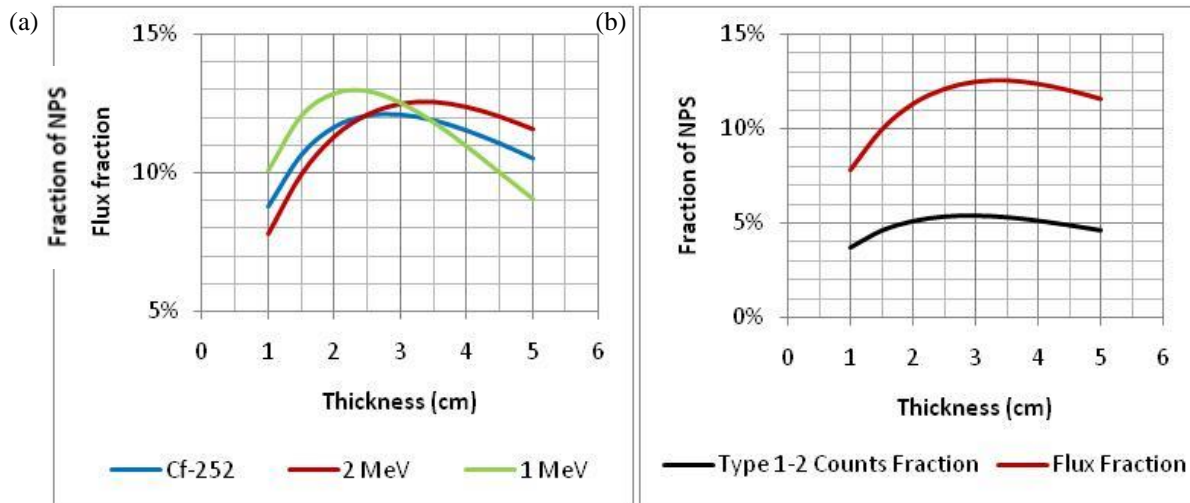


Fig. 4-3. Once-collided neutron flux entering plane 2 for different incoming spectra (a) and comparison with the type 1-2 recorded counts for 2-MeV neutrons (b).



In Fig. 4-3b, we show the fraction of type 1-2 neutron counts per particle simulated (in %) with realistic detector parameters. One can notice that the bump seen on the once-collided flux curve is much less pronounced when tallying actual events with realistic detector parameters. As a consequence, the options for plane 1 detector thicknesses were narrowed down to standardized 2.54 and 5.08-cm thicknesses.

Realistic simulations using mono-energetic sources of interest were then performed with the aforementioned thicknesses to determine the system with the highest efficiency. Counts from the different events types are presented for a sample of the simulations in Table 4-II.

**Table 4-II. Simulated counts obtained from  $10^6$  incident 2 MeV neutrons and  $10^6$  662 keV photons.**

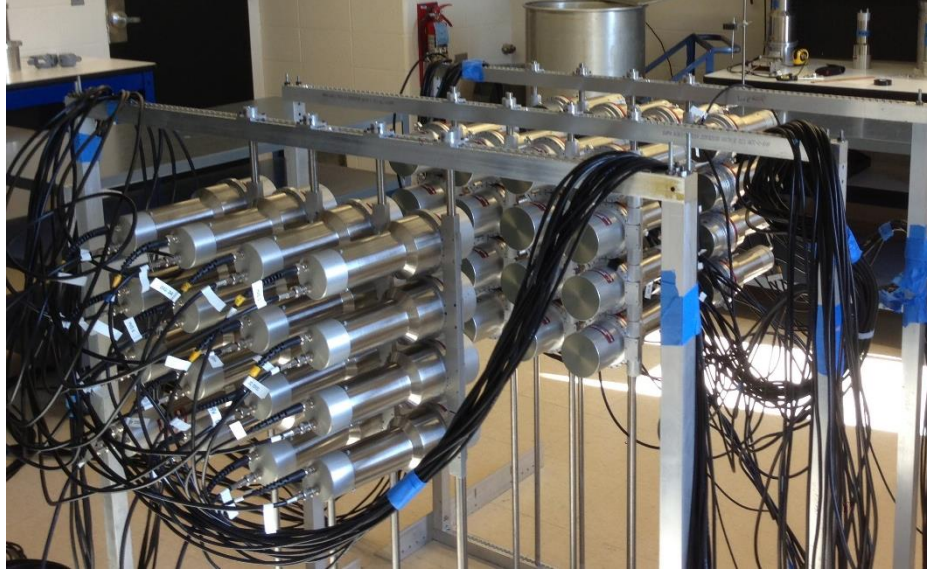
<i>Configuration</i>	<i>2.54-7.62-7.62</i>	<i>5.08-5.08-7.62</i>	<i>5.08-7.62-7.62</i>
Neutron Events	6397	7625	9098
Photon Events	11763	7787	10561

Table 4-II shows that the thicker plane 2 yields more neutron and photon events and is the obvious choice efficiency-wise. Plane 1 thickness displays a tradeoff, as a thinner plane 1 increases photon events but decreases neutron events. It was decided to maximize neutron events over photon events as the number of neutron emitted by a given material is typically lower than its photon emission. The final design consists of 4×4 arrays of 7.62-cm diameter detectors: 5.08-cm thick liquid scintillators for plane 1, 7.62-cm thick liquid scintillators for plane 2, and 7.62-cm thick NaI scintillators for plane 3.

### **4.3. Data-Acquisition Executable and Real-Time Processing**

#### ***4.3.1. Prototype Setup***

A prototype DPI system with 3 planar arrays of 16 detectors was built at the University of Michigan. The prototype is shown in Fig. 4-4.



**Fig. 4-4. Photograph of the prototype DPI system.**

The DPI prototype setup aimed at having planes of detectors with limited space between them. Detectors in each plane were separated by 6.38 cm along the width of the plane, and 2.38 cm along the height of the plane. The first and second planes were separated by 38.22 cm while the second and third planes were separated by 33.78 cm, measured from detection material to detection material. These separations were dictated by the supporting structure and the length of the photomultiplier tubes of the detectors.

Raw pulses from the EJ-309 and NaI(Tl) scintillators were collected using CAEN V1720 waveform digitizers without additional pulse shaping or amplification. EJ-309 pulses are very narrow, with a FWHM of approximately 5 ns, making fast digitizers a good option to obtain accurate energy and time information from the raw pulses. While this is common practice for EJ-309 pulses, it is unusual for raw NaI(Tl) pulses as they are quite noisy and their width requires large waveforms to capture the whole pulse. This approach provided better pulse timing (approximately one order of magnitude), but resulted in noisy pulses and worse energy resolution than is typical for the NaI(Tl) detectors (approximately 10% instead of 6% at 662 keV), as shown in Fig. 4-5. The detectors were gain matched with a Cs-137 source and kept at the resulting voltage

for future measurements. A remotely controlled MPOD unit from W-IE-NE-R was used to supply high voltage for the detectors [40].

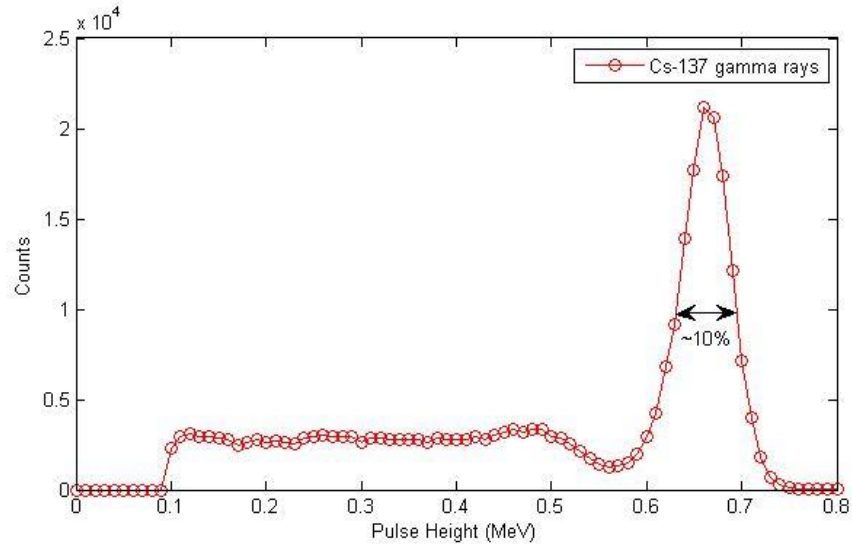


**Fig. 4-5. Energy spectrum of a Cs-137 source measured with a NaI scintillator.**

EJ-309 scintillators have the ability to differentiate between neutron and photon interactions based on the shape of the pulses: neutron pulses have a larger fraction of the pulse in the tail than photon pulses. In this work, we used a charge integration PSD technique, which consists of calculating two integrals for each pulse: one over the tail of the pulse (the tail integral), and one over the entire pulse (the total integral) [32]. The two integrals can then be plotted together as shown in Fig. 4-6. The two different clusters correspond to the two types of interactions in the detector, with the neutron interactions located in the cluster above the photon-interaction cluster.

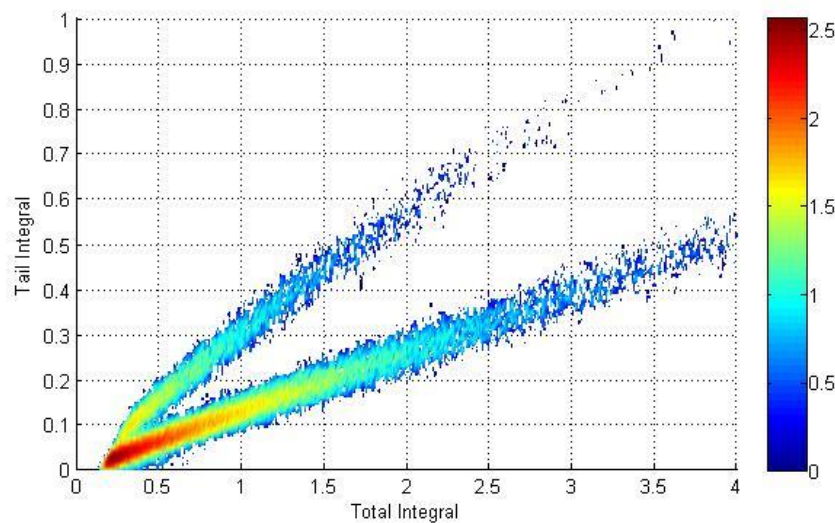


**Fig. 4-6. Tail integral versus total integral plot used for PSD purposes. The color scale is logarithmic.**

Another reason for the use of EJ-309 scintillators is their fast response time. Fig. 4-7 shows the delay between two liquid scintillators adjacent to a Na-22 source. The time resolution for EJ-309 scintillators is approximately 1 ns which allows for reasonable accuracy in neutron TOF calculations. The time resolution for NaI(Tl) scintillators is of lesser importance as photon timing is solely used for correlating events and has no impact on the energy and position uncertainty.

Digital-data-acquisition technology was used because it offers advantages over analog methods such as data-processing flexibility and storage. A new challenge arose as commercially available fast-waveform digitizers (with a sampling frequency above 100 MHz) typically utilize 8, 16, or 32 channels [41], which were not fully suitable for our application (48 channels). As a consequence, multiple digitizers had to be operated simultaneously to create a data-acquisition system able to read in pulses from all 48 detectors used in the DPI system. Accurate synchronization of the digitizers was paramount to achieve the time resolution necessary to obtain accurate TOF for the reconstruction of neutron events. Sub-nanosecond time resolution was required in order to have the time resolution of the EJ-309 detectors as the dominant component of the overall time resolution of the DPI system.

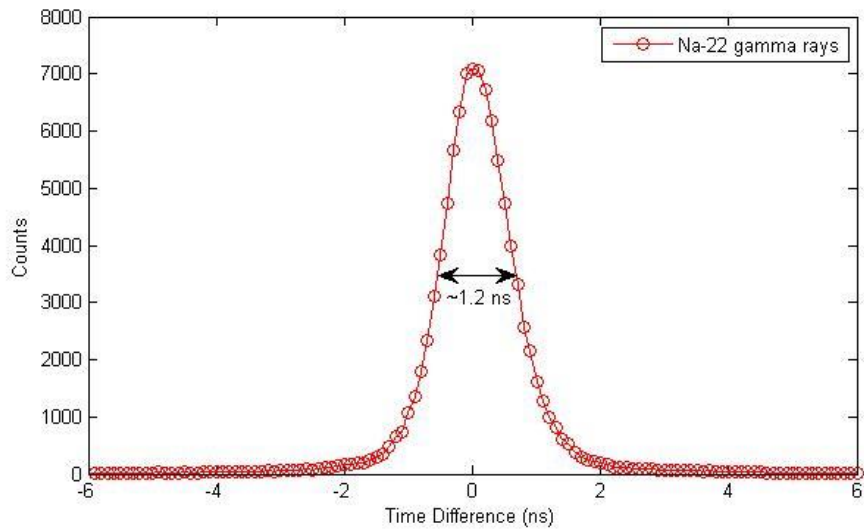


**Fig. 4-7. Time delay between two 7.62-cm thick EJ-309 scintillators, obtained with a Na-22 source.**

The fast waveform digitizers used in this work are CAEN V1720s. Six V1720s are required to read out all 48 detectors of the imaging system. Each board has 8 channels, a 2-Volt dynamic range with 12-bit resolution and a 250-MHz sampling frequency. Each channel can store up to 1024 waveforms before sending them to the acquisition computer. An optical link with a maximum throughput rate of approximately 80 MB/s is used to transfer the measured waveforms from all the digitizers to a data-acquisition computer. The data-acquisition system is shown in Fig. 4-8.



**Fig. 4-8. CAEN VME crate containing 4 V1720 digitizers connected for time synchronization.**

Several CAEN on-board capabilities such as data rejection and multi-trigger logic were implemented into a custom-made, data-analysis software to reduce the amount of data sent to the

data-acquisition computer. This allowed larger measurable count rates without paralyzing (introducing dead times for) the data-acquisition system.

#### 4.3.2. Synchronization Procedure

The system boards are synchronized using a daisy-chain approach, with the first board set as the ‘master’ and the other boards as ‘slaves.’ The synchronization is carried out in two steps. The first step is to synchronize the sampling clock of the boards, including the phase alignment of the individual board clocks. This step ensures that the signal sampling is the same way for all digitizers. The digitizer set as the master provides a reference clock to the slave using a built-in digitizer functionality. The phase of the clocks is then aligned by applying a delay to the reference clock sent to the slave. Fig. 4-9 shows the four sampling clocks of our system after the synchronization has been accomplished.

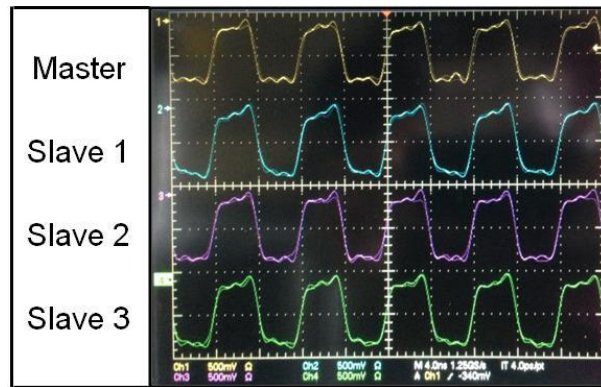


Fig. 4-9. Sampling clocks of the 4 synchronized digitizers.

In the second step, the start of the data acquisition needs to be synchronized to start all system boards at the same time, with sub-nanosecond resolution. This step ensures that the timestamps of the collected waveforms refer to the same absolute time. The start of the acquisition is propagated from master to slave. The synchronization is performed by delaying the start of the master to match that of the slave. This method is illustrated in Fig. 4-10.

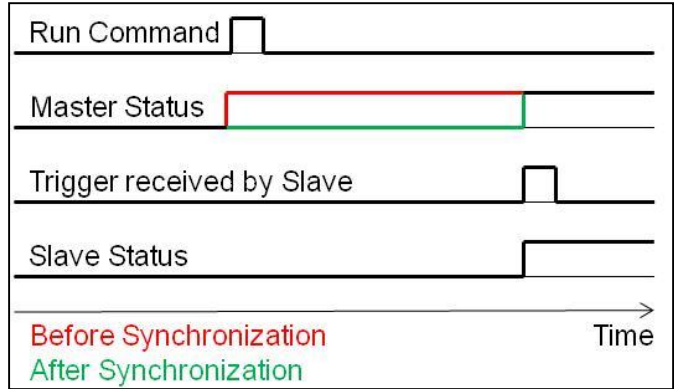


Fig. 4-10. Diagram of the run command synchronization method.

### 4.3.3. System Capabilities

The time resolution of the data-acquisition system was investigated with standardized pulses from an accurate waveform generator, and a sub-nanosecond resolution was achieved between the different boards. Fig. 4-11 shows the results obtained between a channel from the master digitizer, and a channel from the first slave. The global time delay is fixed at a value of -0.5 ns, and has a FWHM of approximately 300 ps.

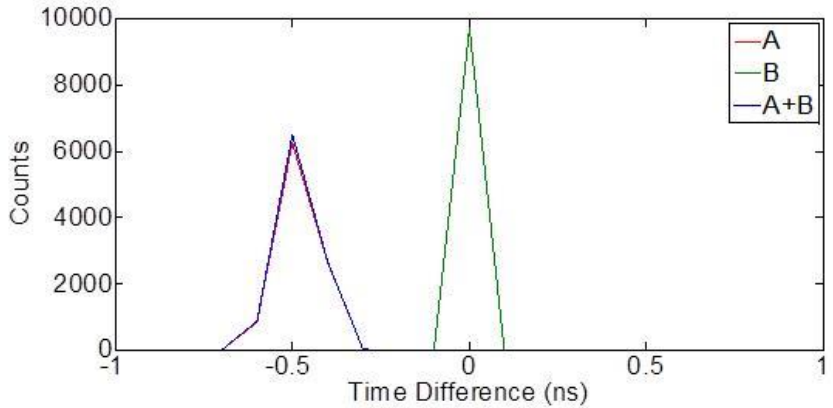
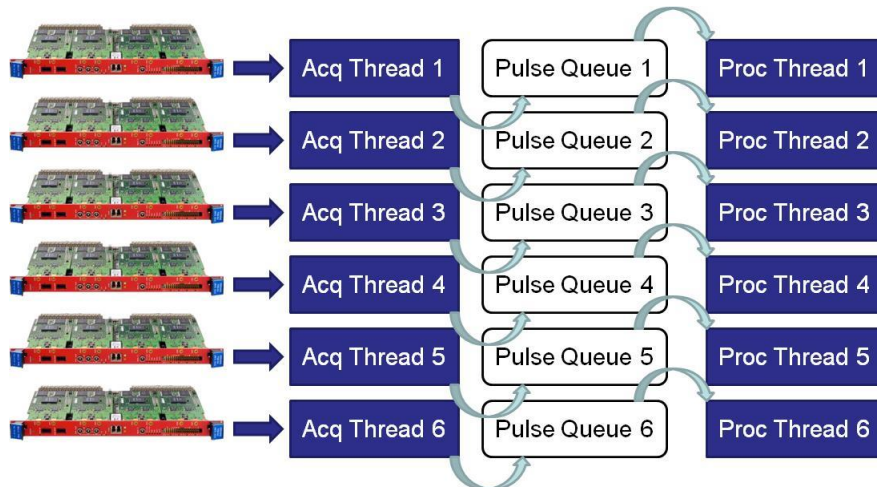


Fig. 4-11. Delay between the first slave in the daisy chain and the master board. 'A' is the delay between the pulses within the data-acquisition window (leading-edge timing), 'B' is the delay between the time stamps, and 'A+B' is the global time delay between the boards.

Once synchronized, the digitizers are operated individually by the data-acquisition software. However, because the boards are accurately synchronized in time and they always start



the data-acquisition at the same time, the collected data can be treated as acquired by a single multi-board system.



**Fig. 4-12. Architecture of the data-acquisition software. ‘Proc thread’ refers to a thread writing the data to the hard drive or a thread processing the data in real time.**

I then wrote the data-acquisition software in C++, using software libraries provided by CAEN. In order to maximize the data-transfer rate, transfer from the digitizer to the data-acquisition computer must be performed in parallel with writing and/or processing. Fig. 4-12 illustrates the architecture of the data-acquisition software. The data received by the computer in an acquisition thread is saved in a queue, which is then accessed by a separate thread dedicated to writing the data to the hard drive. While data transfer needs its own thread, it is not a resource-intensive task and can share a processor with a data-processing/writing thread.

The use of a parallel architecture also had the advantage of enabling real-time data processing: instead of writing the raw data to the hard drive, processing can be done in real time on a separate thread. This includes obtaining the pulse height (highest sample of the pulse), obtaining the pulse time using CFD, and applying PSD to the data from the liquid scintillators. While the integrals for the PSD are calculated in real time, the discrimination curve must be



provided as one of the user inputs. The data resulting from the data-processing thread are then the pulse height, pulse time, and particle type (photon or neutron).

The resulting data can then be either saved to the hard drive, or regrouped in a queue that can then be further processed to correlate the pulses into the events described in section 2 and obtain an image. This task is carried out by an additional thread that has a dedicated processor. The neutron and photon images can then be visualized in real time, along with the energy spectra. MATLAB software is used to print the output to the monitor [42].

#### **4.4. Three-Plane DPI Results**

Two measurements were performed with the three-plane prototype DPI system, with the objective of demonstrating the neutron and gamma-ray imaging capabilities of the system. An  $\approx 50,000$  fissions per second Cf-252 source and a  $\approx 90\text{-}\mu\text{Ci}$  Cs-137 source were measured at a distance of 2.5 m for 1 hour each. Both sources were located on the axis of the DPI system, directly in front. The backprojection images obtained from both measurements are shown in Figs. 4-13 and 4-14. As expected, the system was able to correctly locate the sources, thereby validating the DPI concept.

For the Cf-252 measurement, the neutron image (Fig. 4-13a) correctly provides the location of the source from 1,054 correlated neutron counts, while the photon image (Fig. 4-13b) is overpowered by background and cannot locate the source. The intrinsic efficiency can then be approximated to  $5.24 \times 10^{-4}$  correlated counts per incident fission neutron.

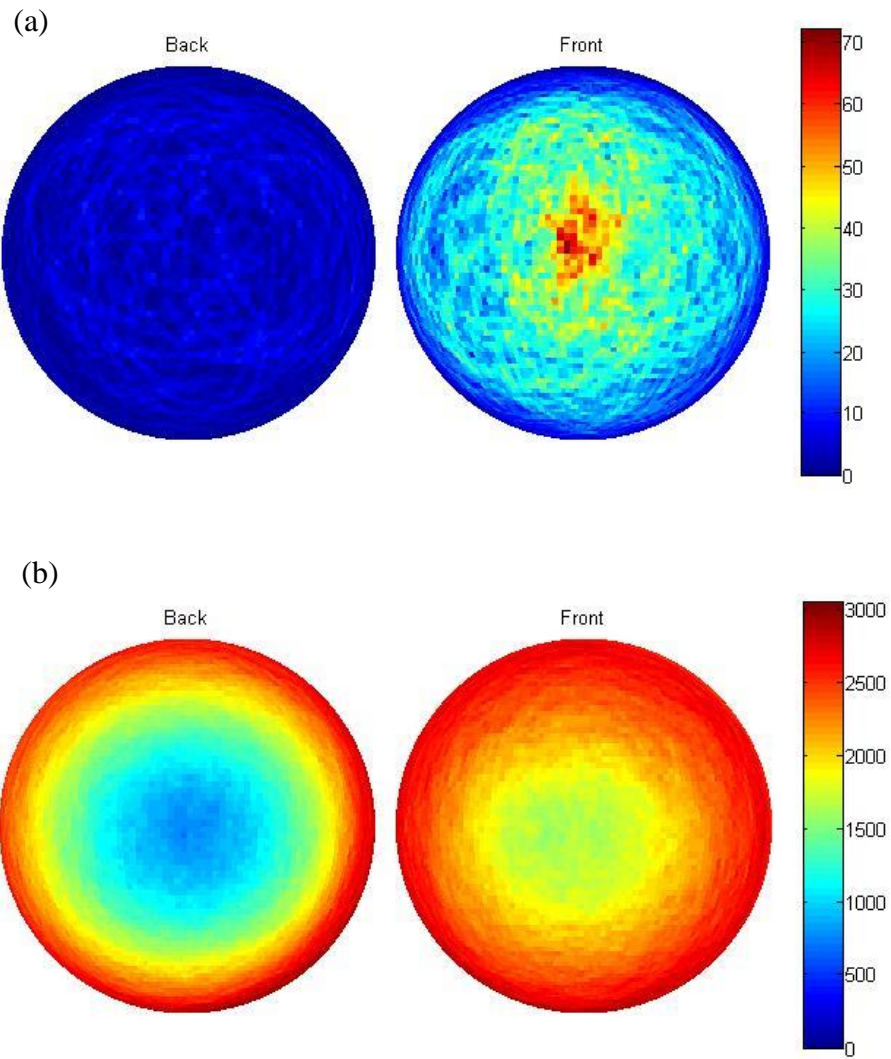


**Fig. 4-13. Neutron (a) and photon (b) images from the measurement of the Cf-252 source. The neutron image displays a hotspot in the direction of the source, while the photon image is overwhelmed by the background radiation.**

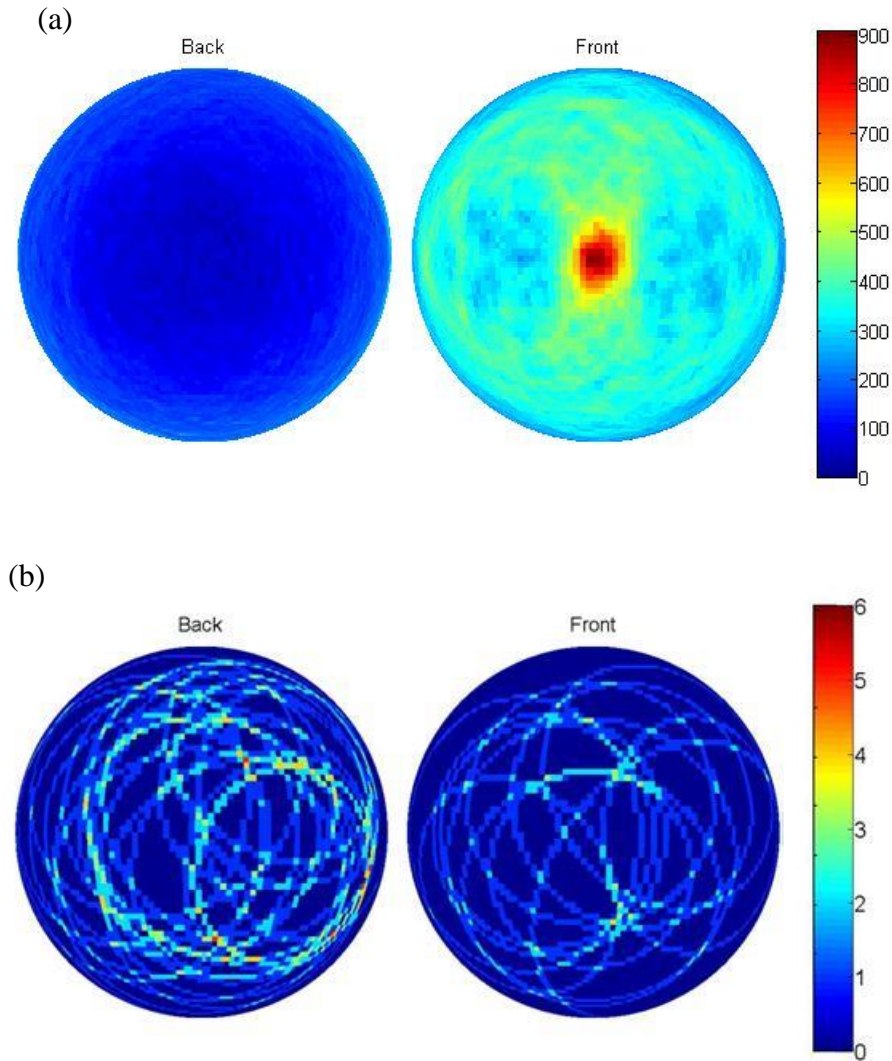


**Fig. 4-14. Photon (a) and neutron (b) images from the measurement of the Cs-137 source.**

Fig. 4-14 shows the photon and neutron images generated from the measurement of the Cs-137 source. As expected, very few neutron cones are created in this measurement. An energy filter is applied to the photon image, to only show cones created from events in a 600- to 700-keV bin. This energy filter can be selected from the energy data obtained from the DPI system. Whereas Cf-252 does not emit discrete gamma energies at high intensities, SNM like plutonium usually has several high-intensity gamma-ray lines, which would enable us to filter out background from the image. Common gamma-ray lines for SNM isotopes are shown in Table 4-III. A total of 45,038

correlated photon counts are collected by the system, with 10,260 counts within the energy filter. The intrinsic detection efficiency can then be approximated to  $1.51 \times 10^{-3}$  correlated counts ( $3.44 \times 10^{-4}$  full-energy depositions) per incident source photon.

**Table 4-III. Principal gamma-ray signatures of SNM isotopes [43].**

Isotope	Energy (keV)	Activity g/g-s
$^{234}\text{U}$	120.9	$9.35 \times 10^4$
$^{235}\text{U}$	143.8	$8.40 \times 10^3$
	185.7	$4.32 \times 10^4$
$^{238}\text{U}$	766.4	$2.57 \times 10^1$
	1001.0	$7.34 \times 10^1$
$^{138}\text{Pu}$	152.7	$5.90 \times 10^6$
	766.4	$1.387 \times 10^5$
$^{239}\text{Pu}$	129.3	$1.436 \times 10^5$
	413.7	$3.416 \times 10^4$
$^{240}\text{Pu}$	45.2	$3.80 \times 10^6$
	160.3	$3.37 \times 10^4$
	642.5	$1.044 \times 10^3$
$^{241}\text{Pu}$	148.6	$7.15 \times 10^6$
	208.0	$2.041 \times 10^7$
$^{241}\text{Am}$	59.5	$4.54 \times 10^{10}$
	125.3	$5.16 \times 10^6$

The spectra in Figs. 4-15 and 4-16 show the spectroscopic capabilities of the system as the use of NaI(Tl) scintillators enable us to see photoelectric peaks in the photon spectrum, while the two planes of EJ-309 scintillators enable us to reconstruct neutron energy using TOF. Fig. 4-16 shows that the Cf-252 photon spectrum does not present any particular feature that could be used to filter out background. The use of an energy filter also prevents from imaging events that did not deposit their full energy, which is once again not applicable to the Cf-252 spectrum with no absorption peak.

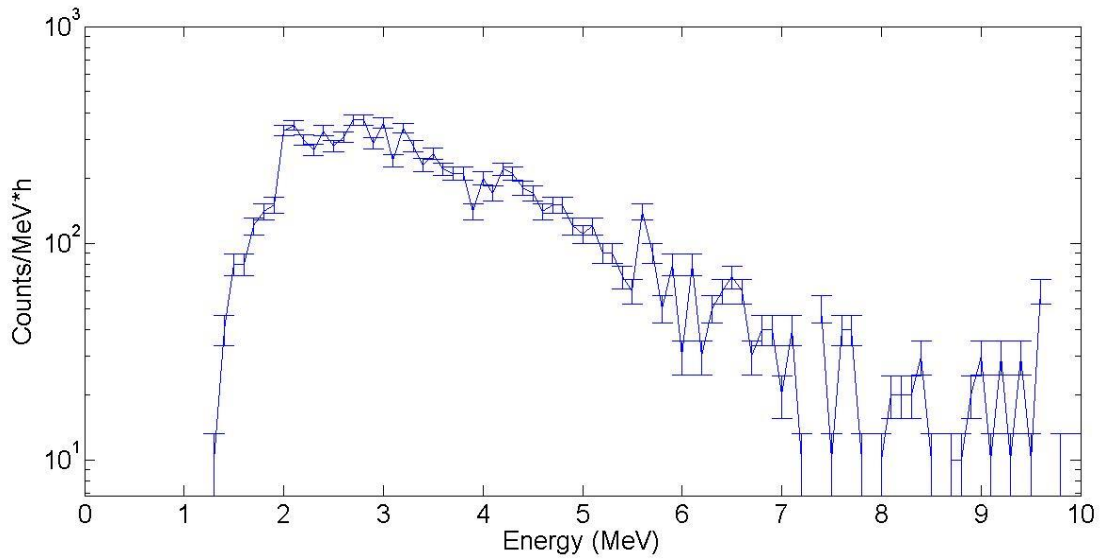


**Fig. 4-15. Neutron reconstructed spectrum from the measurement of the Cf-252 source.**

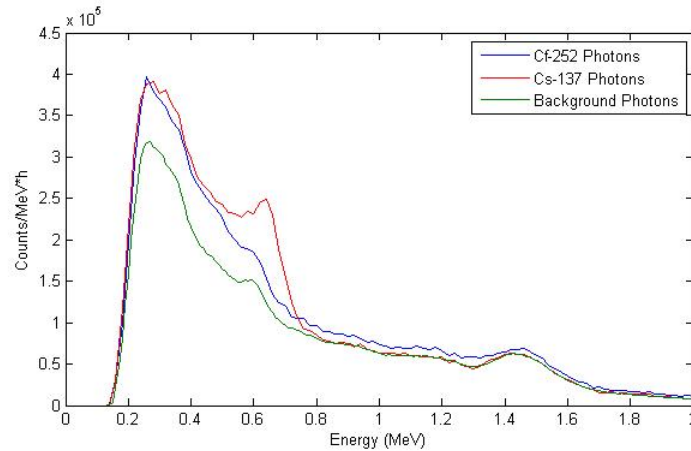


**Fig. 4-16. Correlated photon spectrum from the measurement of the Cf-252 and the Cs-137 source, and a background measurement.**

The measurement results show the ability of the DPI system to image both neutrons and photons. While the FWHM of the imaged hotspot is approximately  $30^\circ$ , the peak is always located within  $\pm 5^\circ$  of the true source location. A more converged image, obtained with a longer measurement time or a fit of the hotspot, should present less noise and more accurately estimate the source location. The photon image would benefit from a finer energy resolution. This is achievable with the use of a shaping amplifier for the NaI pulses; however, it comes at the cost of

poorer time resolution. This would further result in a need for a larger correlation window which could add accidental events.

#### **4.5. Advantages and Limitations of the Three-Plane DPI System**

The prototype DPI system, an instrument capable of imaging both fast neutrons and photons was built and operated successfully. The instrument consists of three planes of scintillators. Two planes of organic-liquid scintillators induce neutron and photon scatters, and give the possibility to use pulse shape discrimination. A plane of NaI(Tl) scintillators induces photoelectric absorptions while being highly insensitive to neutrons. The results show the advantage of imaging both particles as a Cf-252 source would be much more difficult to image with a Compton camera and a Cs-137 source would not be imageable with a neutron-scatter camera. This DPI system shows particular promise for imaging SNM as it has the ability to image both types of particles that are emitted by SNM.

For all its achievements, this system still presents a few drawbacks. The use of 3 planes forces us to have a particle flight path encumbered by the PMTs of the middle plane. The use of NaI(Tl) detectors without a pulse shaper also results in a high level of noise for the photon signal. Chapter 5 will investigate how to improve on these issues.

## Chapter 5. Two-Plane DPI System

### 5.1. Two-Plane DPI Concept & Optimization

#### 5.1.1. Concept Design

The two-plane DPI system combines the principles of a two-plane Compton camera and a neutron-scatter camera into a two-plane design with a combined back plane. EJ-309 and NaI(Tl) scintillators were selected to induce scatters in the front plane and to obtain gamma-ray absorptions and neutron scatters in the back plane. This design, originated from an idea to remove PMT material between detection planes, yielded comparable results to the three-plane design from chapter 4 with fewer detectors [44].

In a two-plane Compton camera, described in chapter 2, preferable events consist of a scatter in the front plane and an absorption in the back plane. A neutron-scatter camera is based on the elastic-scattering process, and the detection process is similar to that of a Compton camera, as described in chapter 3. Fig. 5-1 shows an example of neutron and gamma-ray interactions in the two-plane DPI system.

This system is based on a particle (neutron *or* gamma-ray) coincidence measurement. The use of a coincidence system instead of a coded aperture yields a significant advantage for neutron-spectroscopy capabilities, while sacrificing overall detection efficiency. Specifically, the measured TOF information enables the user to reconstruct the incoming energy of the neutron. The main drawback is lower detection efficiency, resulting from the necessity for one interaction in each detection plane.

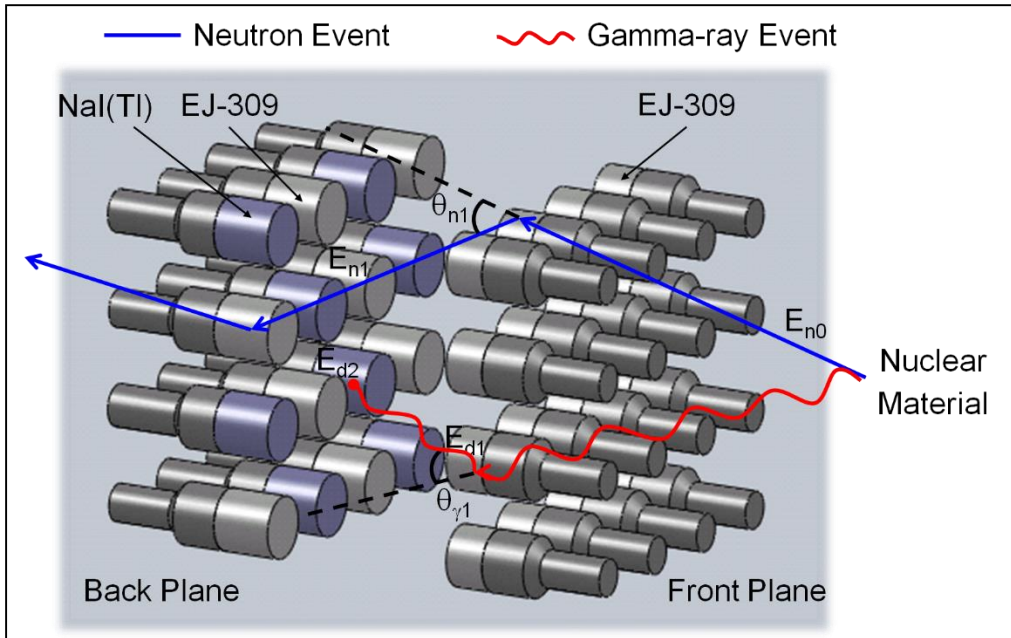


**Fig. 5-1. Diagram of the two-plane DPI system. Gamma-ray and neutron events are illustrated, along with the information used for image reconstruction.**

### **5.1.2. Optimization**

The configuration of detectors in the system shown in Fig. 5-2 was optimized by using the simulation code MCNPX-PoliMi [15]. The detector sizes were selected in chapter 4; the final study was focused on optimizing the distances between the detectors. Three distances were investigated: the separation between the detection planes, the separation between the detectors in the front plane, and the separation between the detectors in the back plane (respectively A, B, and C in Fig. 5-2). MCNPX-PoliMi simulations were performed for various distances and processed using a dedicated post-processing code [16].



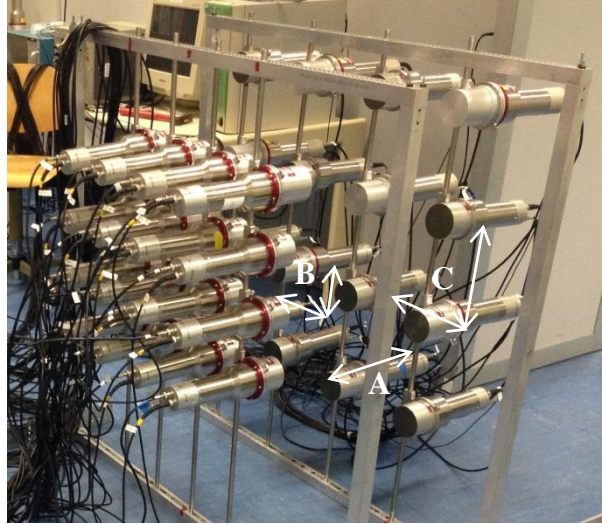


**Fig. 5-2. Optimized DPI system used for the measurement campaign. A, B, and C are the distances investigated in the final optimization study.**

The post processing applied to the simulation data has been introduced in chapter 2. MCNPX-PoliMi produces list-mode interaction data in the detectors, which is subsequently processed to obtain a realistic simulated detector response. Once detector effects, such as energy and time broadening, have been applied to the interaction data, the simulated detector response can be processed with a correlation algorithm. This algorithm outputs correlated counts that can be imaged through simple backprojection or other imaging techniques.

The optimization study was performed by modeling a single Cf-252 point source located 5 m from the center of the system, on the DPI's axis.  $3 \times 10^9$  particles (neutron or photon) were emitted in a cone covering the solid angle of the DPI system in each investigated geometrical configuration.

The study focused on two simulated quantities: the number of correlated counts detected by the system – i.e., the DPI's detection efficiency - and the angular resolution measure (ARM). The ARM is the difference in degree between the energy-calculated scattering angle, and the geometry-calculated scattering angle (knowing the source position). A high detection efficiency and low ARM is desired. Figs. 5-4 and 5-5 show the evolution of those parameters for various

geometries. The distance between the planes was varied between 10 and 50 cm, in 10-cm increments. The study investigated separations between 15 and 30 cm with a 2.5 cm increment. The separations correspond to the distances between two detector centers. Each combination was simulated for the five plane separations investigated.

Fig. 5-3 shows the intra-plane detector-separation results, which highlight a few geometries that optimize both efficiency and ARM. The overall trend of the data shows that the system benefits from having a front-plane detector separation smaller than the back-plane one. While only the photon data is displayed in Fig. 5-3, the neutron data followed the same trend. For a given back-plane separation, the detection efficiency decreases and angular resolution increases with an increase in front-plane detector separation. As such, the shortest separation of 15 cm was selected for the front-plane detectors. The use of a larger separation for the back-plane detectors increases the detection of large-angle scatters. It also decreases the detection probability for small-angle scatters which are likely for energy depositions below threshold in the front plane. A separation of 25 cm between the detectors in the back plane was selected as a tradeoff between the efficiency and the ARM .

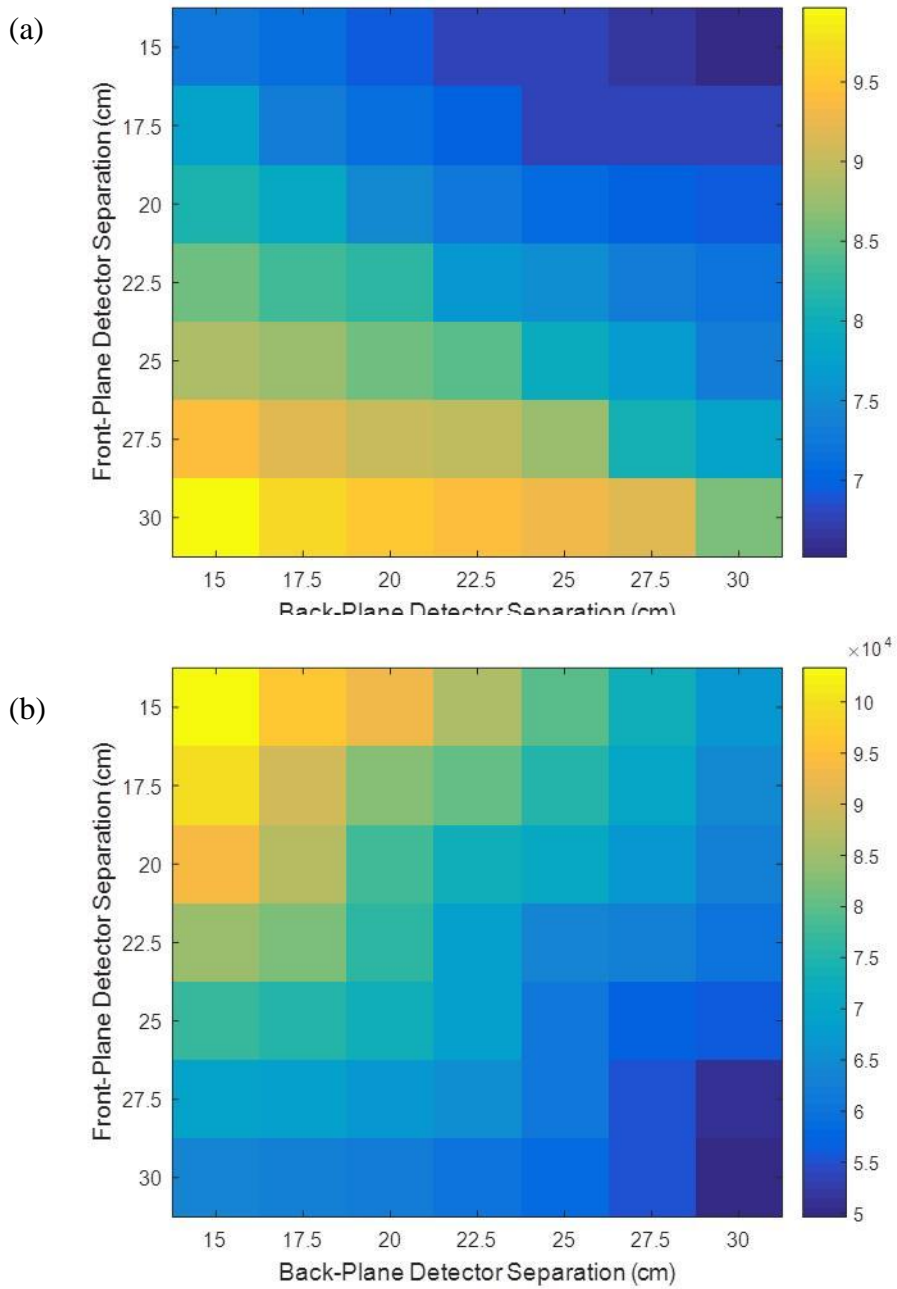


**Fig. 5-3. MCNPX-PoliMi simulation of the photon angular resolution measure (a) and correlated photon counts (b), for various geometries. The units of the color bars are degrees and counts, respectively. The values displayed here were averaged over the 5 plane separations investigated.**

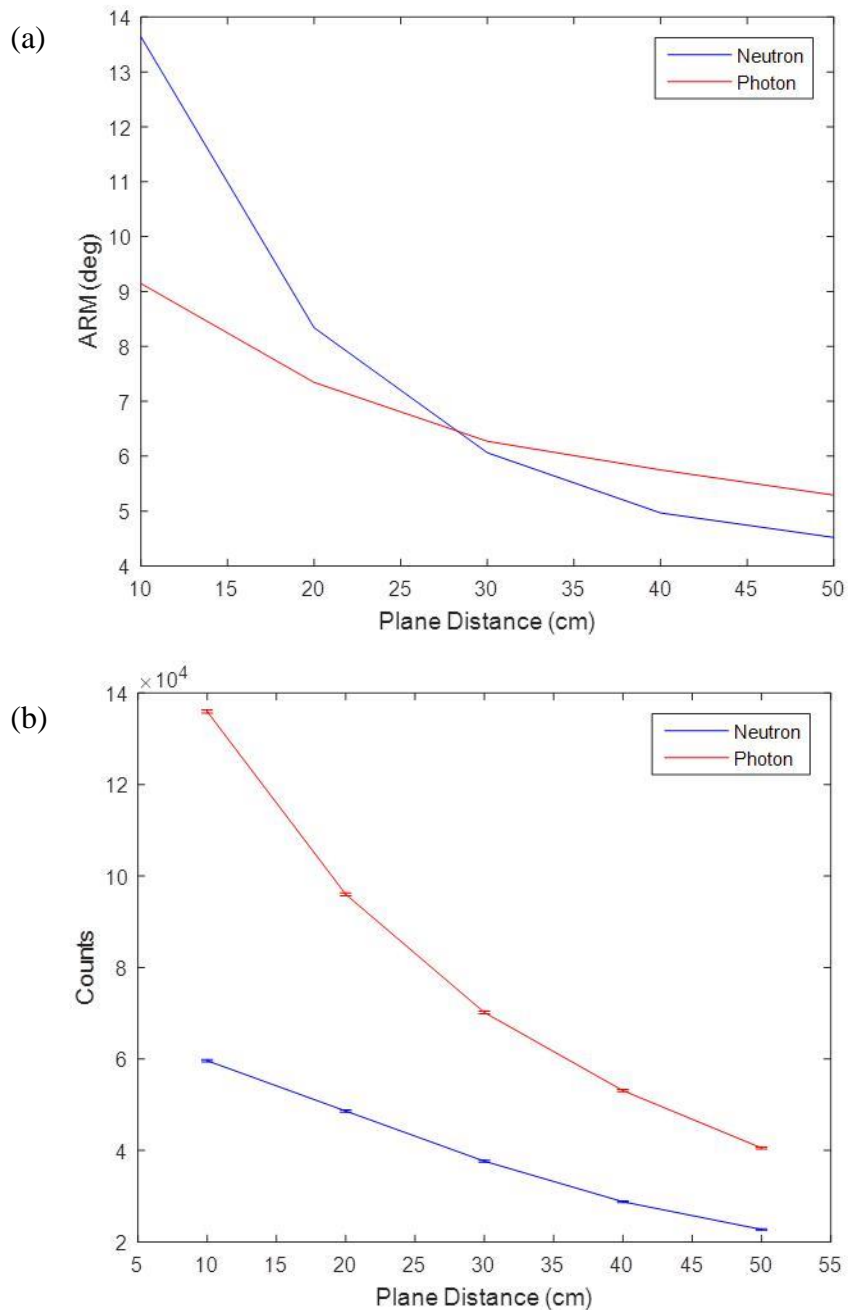


**Fig. 5-4. MCNPX-PoliMi simulation of the angular resolution measure (a) and correlated counts (b), for various plane separations. The intra-plane detector separations used are 15 cm in the front plane and 25 cm in the back plane.**

Fig. 5-4 shows the ARM and system efficiency as a function of the distance between the planes. The figure shows that there is a tradeoff between the efficiency and the angular resolution of the system. This result suggests that we can vary the plane separation depending on the

requirements: a higher-efficiency application will require the planes close together whereas a higher angular resolution can be achieved by moving the detection planes further apart. A plane separation of 30 cm was selected as a good tradeoff between the efficiency and the angular resolution of the system.

Table 5-I shows the relative differences of the parameters studied to the selected plane separation. This table highlights how the ARM varies at a lesser rate than the system efficiency as the plane separation increases. We can also notice that the neutron ARM is more affected by the plane separation than the photon ARM. This is expected since the calculation of the neutron scattering angle relies on the TOF.

**Table 5-I. Relative differences of the optimization parameters to the chosen plane separation.**

Plane Separation (cm)	Relative Neutron ARM Difference (%)	Relative Photon ARM Difference (%)	Relative Neutron Efficiency Difference (%)	Relative Photon Efficiency Difference (%)
10	+125.0	+45.8	+58.3	+93.8
20	+37.6	+17.1	+29.1	+36.8
30	0.0	0.0	0.0	0.0
40	-18.1	-8.3	-23.6	-24.3
50	-25.5	-15.7	-39.6	-42.2

Based on the aforementioned optimization studies aimed at finalizing the DPI system's configuration, the detectors in the front plane (5.08-cm thick EJ-309) are separated by 7.48 cm (15-cm separation minus 7.62-cm detector diameter). The detectors in the back plane (7.62-cm thick EJ-309 and NaI(Tl)) are separated by 17.48 cm (25-cm separation minus 7.62-cm detector diameter). Because one 5.08-cm thick detector was damaged, one of the front-plane detectors had to be replaced by a 7.62-cm thick EJ-309.

## 5.2. Results

### 5.2.1. Efficiency & Field of View

A field of view experiment was setup in the laboratory facilities at the University of Michigan. The experiment consisted in a series of 2-h measurements of a 35,000 fission per second Cf-252 source. The source was located at different azimuthal angles  $\theta$  shown in Fig. 5-5, 2 m from the center of the system.  $\theta$  was varied from  $-90^\circ$  to  $90^\circ$ . The inclination was held constant at  $90^\circ$ , which aligns with the system center. Given the symmetry of the system, this range can be extrapolated to draw conclusions on the full  $4-\pi$  universe.

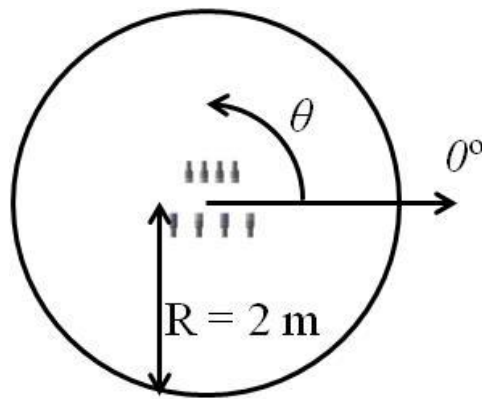
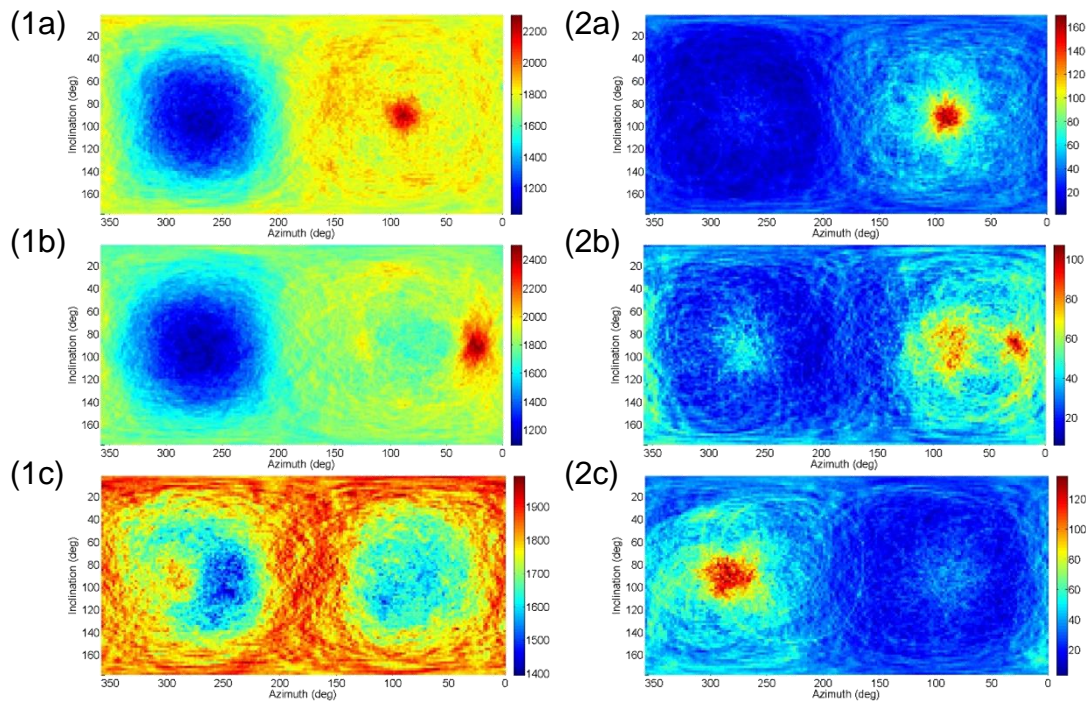


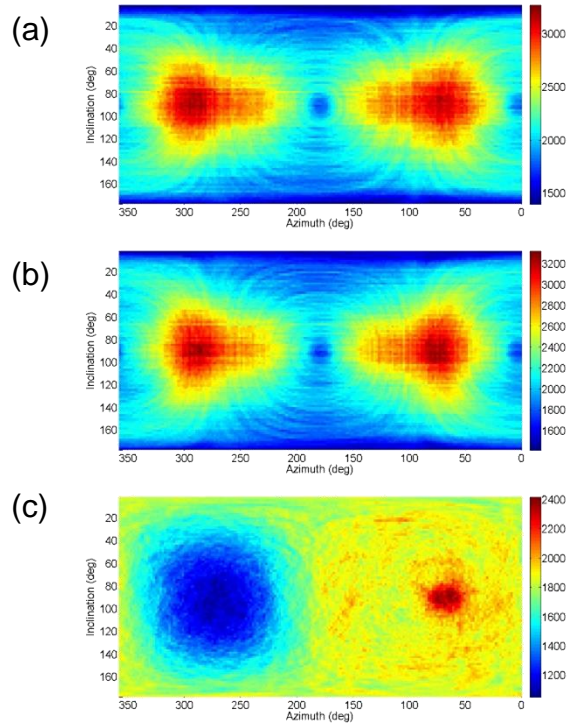
Fig. 5-5. Setup of the field of view measurements.

Fig. 5-6 shows the resulting backprojection images for various angles investigated. In most cases, both the neutron and photon images display a hotspot in the correct source location. When the source is located behind the system, we can notice that the source hotspot in the photon image is below the background feature. This could prove troublesome when trying to locate a photon source behind the system. A simple way to circumvent this problem is to correlate photon counts in the backplane, the same way this is carried out between plane 2 and plane 3 in the three-plane system. The liquids of the backplane acting as plane 2 and the NaI(Tl) of the backplane acting as plane 3. I will refer to those counts as backplane events, as opposed to standard events. Fig. 5-7a

shows the backplane event image for  $\theta = -70^\circ$ , with two very wide hotspots at  $\theta = -70^\circ$  and  $\theta = 70^\circ$ . This image is very similar to Fig. 5-7b which shows the backplane event image for  $\theta = 70^\circ$ . In the end, using both the backplane event image, and the standard event image gives the user a rough location of the source as the standard event image for  $\theta = 70^\circ$ , shown in Fig. 5-7c displays a single hotspot at  $\theta = 70^\circ$ . This result indicates that the DPI system has a  $4-\pi$  field of view for both particles.



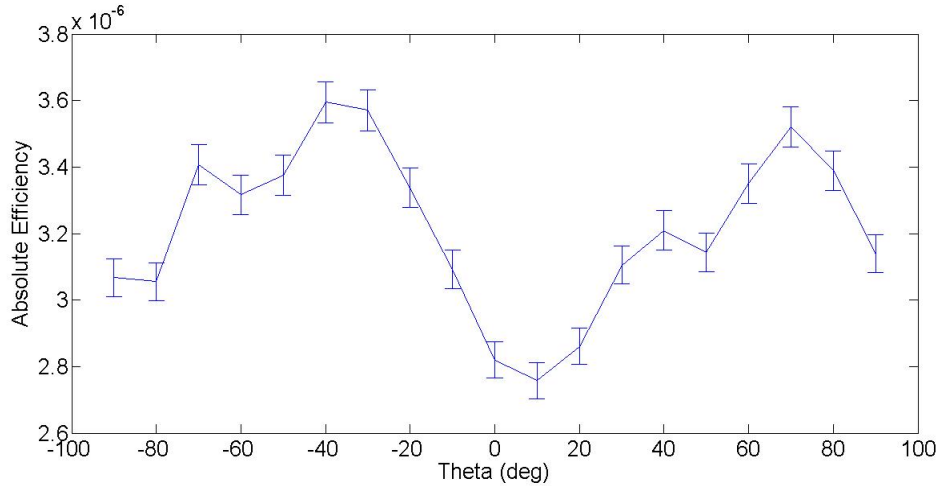
**Fig. 5-6. Photon (1) and neutron (2) backprojection images for  $\theta = 90^\circ$  (a),  $\theta = 30^\circ$  (b), and  $\theta = -70^\circ$  (c)**



**Fig. 5-7. Backplane event image for  $\theta = -70^\circ$  (a),  $\theta = 70^\circ$  (b), and standard photon image for  $\theta = 70^\circ$  (c).**

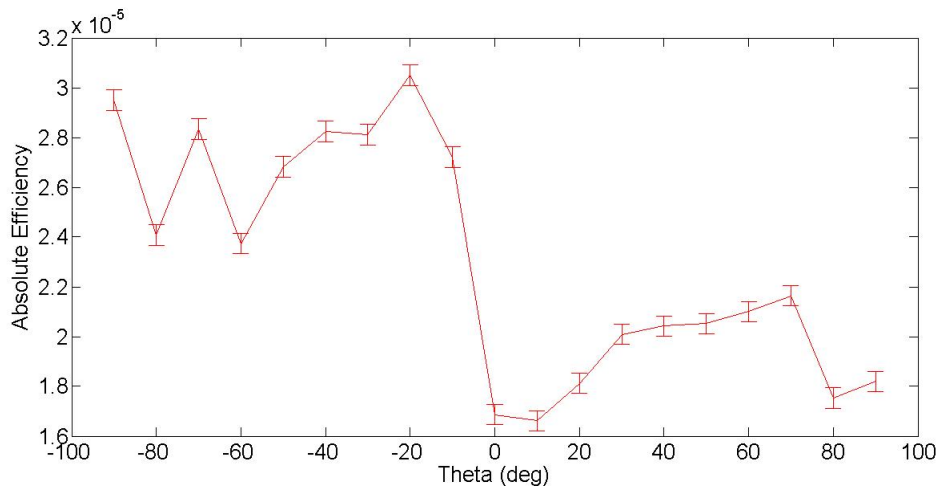
These measurements were also utilized to compute the efficiency of the system. The neutron efficiencies for the different source locations are displayed in Fig. 5-8. We can clearly see that the system is more efficient when the source is not exactly on-axis ( $\theta = 90^\circ$  and  $\theta = -90^\circ$ ). This is expected as the counts from an on-axis source that hit both planes will have a tendency to be low-angle scatters which can be under detection threshold. The dip around  $\theta = 0^\circ$  is also expected, as the imageable counts from that source position will have a tendency to be large-angle scatters, leaving little energy to deposit in the second interaction.





**Fig. 5-8. Neutron efficiency map for the range of angles measured.**

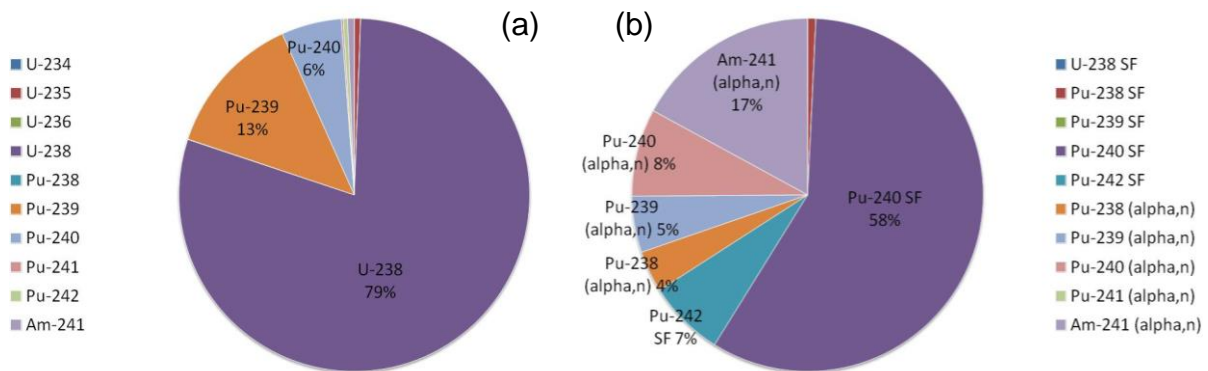
The photon efficiencies are shown in Fig. 5-9. A similar pattern as the one seen with neutrons is shown for  $\theta > 0^\circ$ . This is expected as the threshold affects both particles. We can see that the “efficiency” increases when the source is behind the system. This is due to the high efficiency of the NaI(Tl) coupled with the correlation process used. Since photons travel too fast to know which interaction happens first, events with first interactions in the NaI(Tl) are still recorded by the system. This is why, even though, the efficiency increases, the hotspot for a source behind the system is not as pronounced, as seen in Fig. 5-6 (1c).



**Fig. 5-9. Photon efficiency map for the range of angles measured. Only standard events are used for the calculation.**

### 5.2.2. MOX Measurements

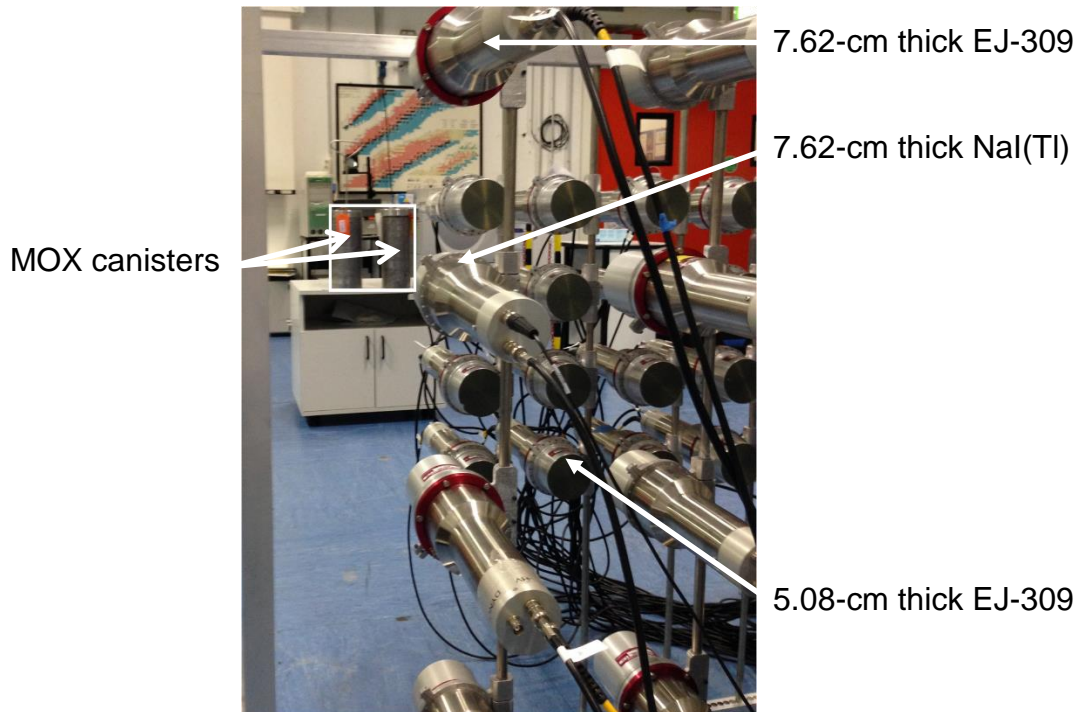
I performed experiments, with 2 fellow Ph.D. students, using the DPI system at the JRC Performance Laboratory (PERLA) in Ispra, Italy in May 2014. The objective of these measurements was to characterize the DPI system in the presence of nuclear fuel. Various SNM samples are available at PERLA, including uranium and plutonium mixed oxide (MOX), Pu oxide, and Pu metal. I focused the testing of the DPI system on 2 MOX canisters of approximately 1 kg each. Measuring MOX canisters offers two advantages. First, the radiation activity of the MOX sources enabled us to obtain an acceptable amount of data in a limited time (the measurement times were limited to 2 hours). Second, MOX is representative of the type of material, in both shape and composition, that the DPI system would be tasked with localizing/characterizing in nuclear-safeguards applications. Both canisters have very similar, well-known isotopic compositions, shown in Fig. 5-10a, and neutron production contributions, shown in Fig. 5-10b, with one canister containing slightly more material than the other. The isotopic abundances of MOX2 are within 2% of the ones from MOX1. The availability of two sources of similar composition provided us with an opportunity to analyze the angular resolution of the DPI system, as well as to assess its potential for characterizing category-3 SNM.



**Fig. 5-10. Isotopic composition of the MOX1 sample (a) and corresponding neutron emission rates (b). SF denotes spontaneous fission.**

### 5.2.3. Angular-Resolution Analysis

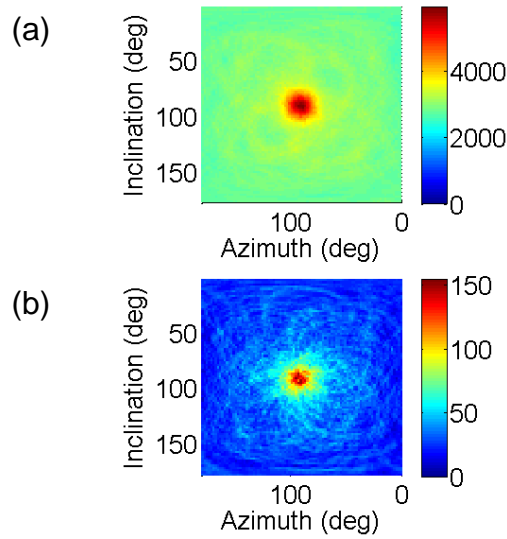
Measurements were set up with the two MOX canisters in front of the system, 2.5 m away from the center of the system, and angular separations ranging from  $5^\circ$  (21.8 cm) to  $30^\circ$  (129.4 cm) in  $5^\circ$  increments. The setups (from  $5^\circ$  to  $30^\circ$ ) were respectively measured for 90, 105, 75, 75, 120, and 120 minutes. The variability in these measurement times was due to facility constraints. Fig. 5-11 is a photograph of the  $5^\circ$  separation setup as seen from the DPI system. The acquired data were processed in real time, which gave us immediate feedback on the DPI system's performance and the opportunity adjust the system if needed.



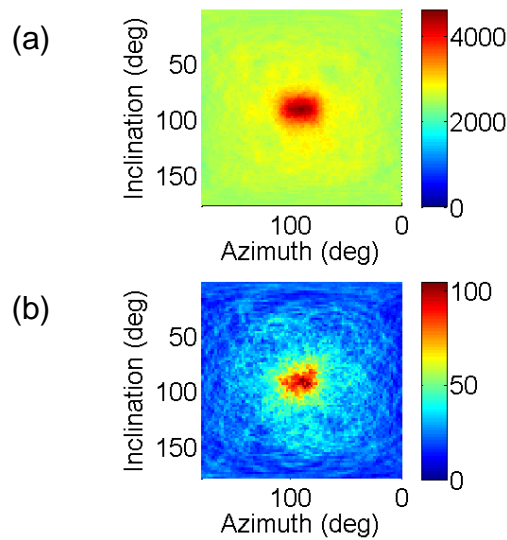
**Fig. 5-11. View of the 2 MOX canisters, with a  $5^\circ$  separation, placed at a distance of 2.5 m from the DPI system. The canisters are highlighted with the white square.**

Figs. 5-12 to 5-14 show the gamma-ray and neutron backprojection images obtained for  $5^\circ$ ,  $15^\circ$ , and  $30^\circ$  separations, respectively. All the backprojection images were obtained by projecting cones with a  $2^\circ$  angular thickness on a  $2^\circ$ -meshed sphere. The color bars highlight the number of cones intersecting in a given direction pixel, which we will refer to as the intensity. For each case,

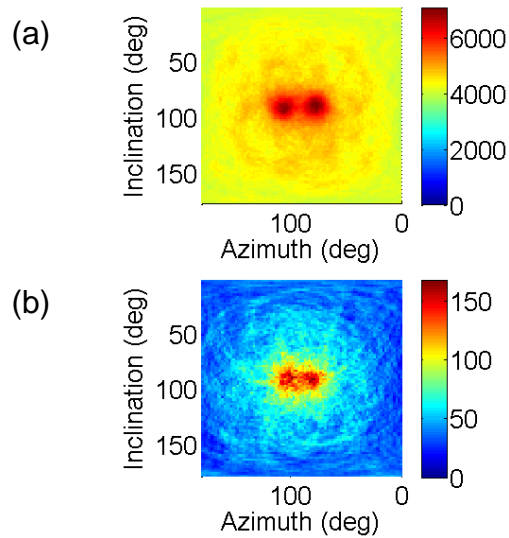
both images display hot spots at the source location with the neutron image not fully converged due to the relatively short measurement times. The evolution of the separation is noticeable on the images, as the single hot spot seen for the  $5^\circ$  separation (Fig. 5-12) starts extending along the azimuth, going through an oblong shape for the  $15^\circ$  separation (Fig. 5-13) and reaching two resolved peaks for the  $30^\circ$  separation (Fig. 5-14).



**Fig. 5-12. Gamma-ray (a) and neutron (b) backprojection images of 2 MOX canisters separated by  $5^\circ$  measured for 90 minutes.**



**Fig. 5-13. Gamma-ray (a) and neutron (b) backprojection images of 2 MOX canisters separated by  $15^\circ$  measured for 75 minutes.**



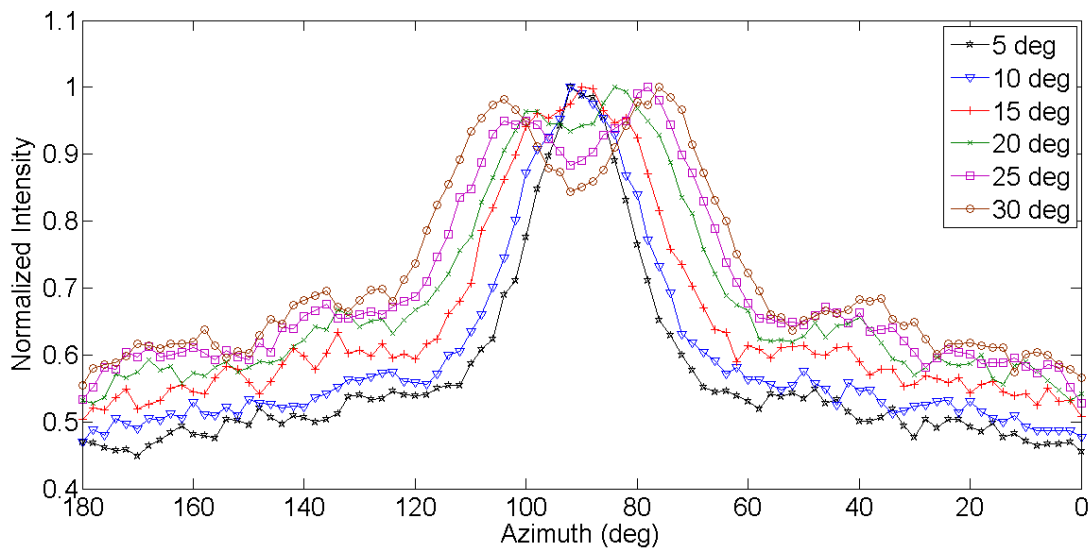
**Fig. 5-14. Gamma-ray (a) and neutron (b) backprojection images of 2 MOX canisters separated by 30° measured for 120 minutes.**

Fig. 5-15 shows the horizontal slice along the maximum intensity point of the gamma-ray image for each of the six investigated MOX configurations. We can see the formation of the two peaks start at the 20° separation case with the cases at lesser separation displaying a single hot spot. The 20° separation case displays two peaks with the left peak reaching 96.5% of the right peak intensity and a valley between them reaching a low of 93.4%. This result indicates an angular resolution between 15° and 20° which is underestimated by the ARM of 6.3° recorded during the optimization study. This ARM would have predicted an angular resolution between 10° and 15°. The underestimation can also be due to the volume of the sources, as the MOX canisters are not point sources. This is by design as those canisters are representative of the type of material the DPI system would encounter in the field.

As the separation between the canisters increases, the valley becomes lower, reaching 84.4% of the maximum intensity for the 30° separation, with a left peak at 98.7% of the maximum intensity. The intensity outside of the defined Gaussian peaks reaches a level of 69% of the maximum intensity at the base of the peaks. The intensity outside of the Gaussian peaks can be

attributed to background as well as accidental correlations such as events that interact in the photomultiplier tubes or do not deposit their full energy. Setting this value as the baseline of the Gaussian peaks, we can notice that the valley reaches the half maximum of the hot spot.

The study could not be carried out for the neutrons due to low statistics. A method to circumvent this is to increase the thickness of the projected cones. This was not further investigated as it would intrinsically degrade the angular resolution results by increasing the size of the hotspots. Fig. 5-14b does, however, show two separate hot spots in the neutron image. The neutron image has the advantage of being relatively unaffected by background radiation, allowing sources to be localized using a low number of counts.



**Fig. 5-15. Gamma-ray backprojection hot-spot slices for all measured angular separations.**

Two other imaging methods have been investigated with the DPI system: maximum-likelihood expectation-maximization (MLEM) and stochastic origin ensemble (SOE). SOE is an imaging method that creates its final image by sampling a point from each cone, and iteratively relocating points (on each cone) to denser areas of the image [45]. While both methods are very efficient in removing unnecessary features from the image, they are computation intensive. Fig. 5-16 shows a comparison between the images obtained for each method. We can see the advanced

imaging methods enable us to separate 2 hot spots in a case where backprojection does not, even with the relatively low number of neutron counts collected.

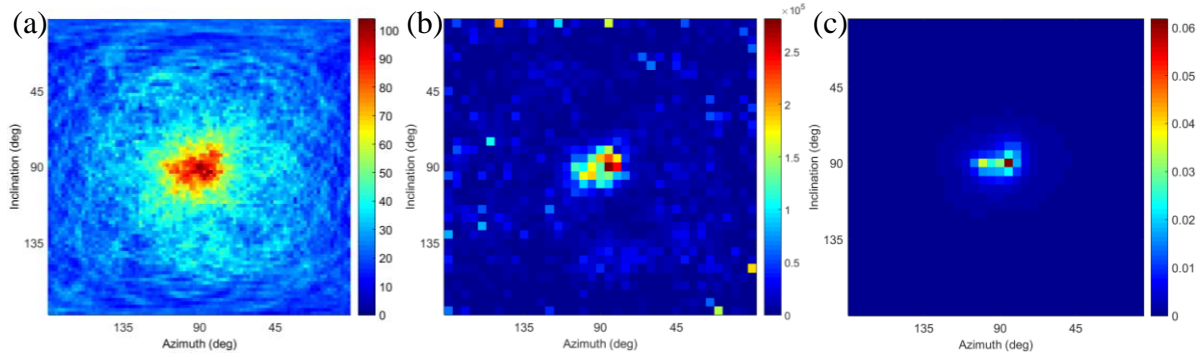


**Fig. 5-16. Comparison between backprojection (a), MLEM (b), and SOE (c) neutron images for the 15° separation case.**

#### **5.2.4. Simulation Validation**

The relative absence of neutron background also enables us to compare measured to simulated results using our simulation tool. Results show that our simulation tool can accurately simulate the neutrons emitted by MOX. Fig. 5-17 displays the measured and simulated images for a 30° separation case. The measurement yielded 90% of the correlated neutron counts recorded in the simulation. We can see matching features on both images, with the hot-spot intensity of the simulated image slightly higher than that of the measured image. This matches the discrepancy in the number of correlated neutron counts collected by the system. The clearer separation between the hot spots points to a slight underestimation of the resolution from the simulation. This discrepancy falls within the expected inaccuracies of our model. Those inaccuracies include the uncertainty on the source strength and isotopic concentrations, the uncertainty on the photomultiplier tube model, and the particle misclassification from PSD.

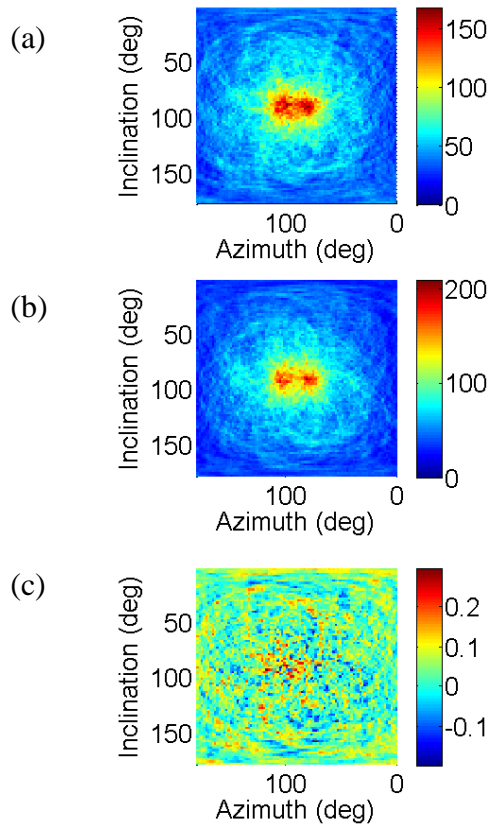


**Fig. 5-17. Measured (a) and simulated (b) neutron backprojection images for the 30° separation case and a visualization of the difference between the images normalized to their highest intensity (c).**

### 5.2.5. Material Characterization

The measured and simulated neutron energy spectra for the 30° separation case are shown in Fig. 5-18. While both spectra are noisy, due to a relatively low number of counts ( $\approx 3000$  counts), they both display the same shape. We expect a Watt spectrum for the spontaneous fission neutrons which make up 66% of the emitted neutrons. The remaining neutrons, which result from ( $\alpha,n$ ) reactions, are expected to have a higher average energy than the spontaneous fission neutrons. The spectrum collected has a bias towards higher energies due to the relatively high thresholds applied to the detectors. For a single neutron event, both energy depositions must be above the detection threshold to be recorded by the system.



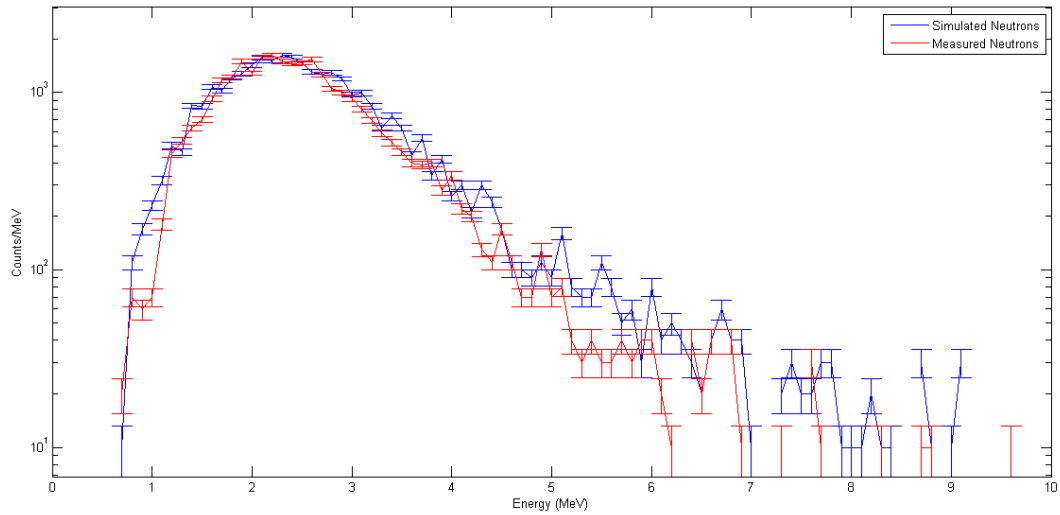


**Fig. 5-18. TOF-derived neutron spectrum from the 30° separation case. The spectrum is obtained from the energy deposited in the first scatter and the subsequent TOF.**

While neutron spectra do not have easily recognizable features, the slope of the spectrum between 2.5 and 6 MeV can be used to discern a pure spontaneous fission source from a mixed source like the MOX canisters as shown in Fig. 5-19. The spectra can also be smoothed to facilitate the differentiation [46]. This characterization can also be done by looking at single-detector neutron PHD [47].

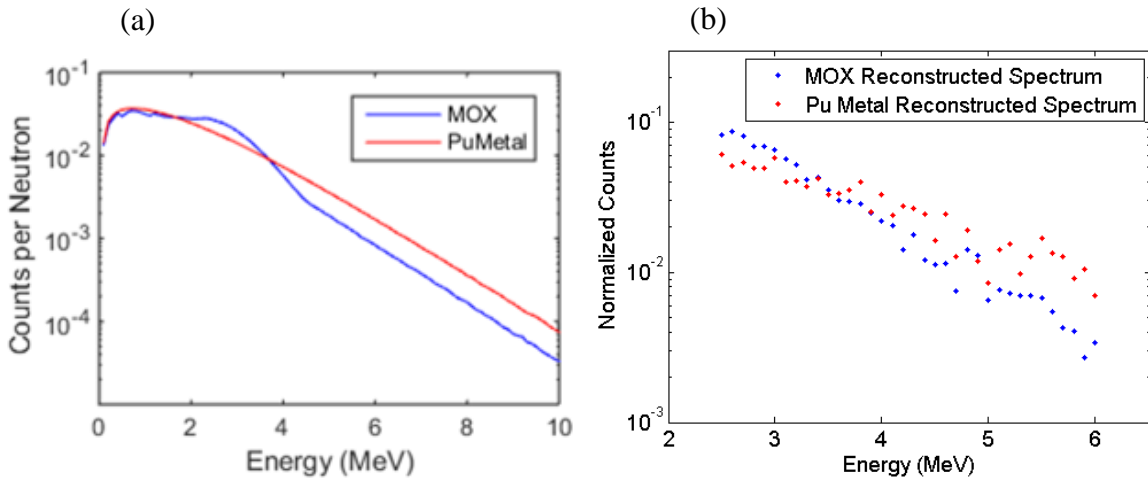


**Fig. 5-19. Emitted spectrum (a) and TOF-reconstructed spectrum (b) from MOX and plutonium metal.**

The measured photon spectrum does not provide substantial information on the source as it is dominated by the background radiation. If background data are not available to carry out a background subtraction, using energy considerations on the backprojection images can yield information about the energy of the source. Fig. 5-20 shows the backprojection images for different photon energies. We can clearly see that the 300-800 keV energy range yields most of the hot spot, which is consistent with the range of energies expected from plutonium and its fission products. This method could be further analyzed by observing the energy spectrum in different regions of the backprojection image. The use of an advanced imaging technique like MLEM would also give the user the opportunity to deconvolve both position and energy information at the same time [48].

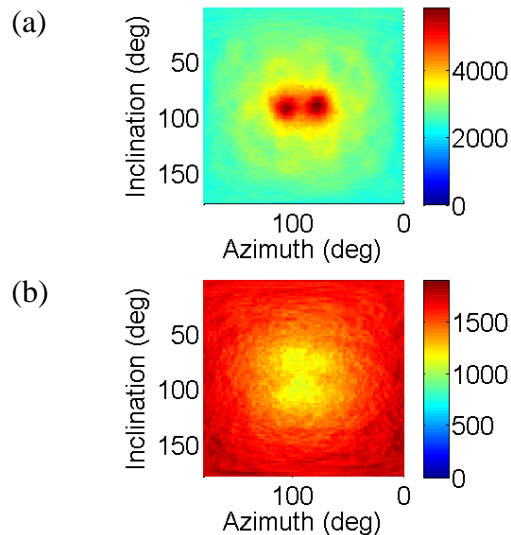


**Fig. 5-20. Gamma-ray backprojection images for the summed energies between 300 and 800 keV (a) and for all other summed energies (b).**

### 5.3. Summary, Advantages, and Limitations of the Two-Plane DPI System

A two-plane DPI system able design was derived from the three-plane system described in chapter 4. It consists of a front plane made of organic-liquid scintillators to detect gamma-ray and neutron scatters, and a back plane made of interlaced EJ-309 and NaI(Tl) to induce neutron scatters

and gamma-ray photoelectric absorptions. The DPI system's geometry was optimized using MCNPX-PoliMi to maximize detection efficiency while optimizing the angular resolution. The DPI system was subsequently characterized.

The field of view and the efficiency of the system were measured with a Cf-252 source. The system demonstrated the capability of imaging sources in the full  $4\pi$  universe. Absolute efficiencies were calculated for each source position, being approximately  $10^{-6}$  for neutrons and  $10^{-5}$  for photons. These efficiencies are of course linked to the energy of the particles measured. These low efficiencies are somewhat offset by the ability of coincidence systems to use a low number of counts to image a source. They are however a possible hindrance, particularly for standoff detection applications which will not see many particles reach the DPI system.

Measurements of two well-characterized MOX canisters placed at a distance of 2.5 m and with separation ranging from  $5^\circ$  to  $30^\circ$  were performed with the DPI system. The minimum separation that yielded two separate hot spots on the gamma-ray backprojection image was found to be approximately  $20^\circ$ . Given our  $5^\circ$  step, we can conclude that the angular resolution of the DPI system is between  $15^\circ$  and  $20^\circ$ . While the  $30^\circ$  case yielded a neutron image with two separate hotspots, the neutron images do not have enough counts to accurately obtain an angular resolution measurement. The comparison of measured and simulated results validated the use of our simulation tool for the optimization of the DPI system.

The system has demonstrated the ability to distinguish MOX canisters with an angular separation of at least  $20^\circ$ , which, for a distance to the source of 2.5 m, equates 86 cm. The system may have too low efficiencies to use for standoff detection, but should be appropriate for the preliminary localization of hot zones in nuclear facilities. The DPI system has also shown source characterization capabilities using both neutron and gamma-ray information. The neutron

information, using the TOF-derived neutron spectrum or single-detector PHDs, has the advantage of being relatively unaffected by background. The photon spectral information needs background subtraction, which was performed in this work by coupling it with the position information.

## **Chapter 6. Summary, Conclusion and Future Improvements**

### **6.1. Conclusions**

Throughout this work, I have designed, constructed and operated a detection system capable of imaging and characterizing nuclear material by using fast-neutron and gamma-ray signatures. This work began with simulations as the large scale of the systems under investigation required an extensive preliminary exploration to warrant the purchase of equipment. The simulations also provided the opportunity to gain familiarity with imaging systems, as the plethora of information available from each simulated interaction enabled me to fully understand the underlying physics. Monte Carlo simulations were utilized to investigate and optimize the final design of the system. A final design was selected with a front plane more compact than the back plane (15 cm between detectors center in the front plane versus 25 cm in the back plane), and a 30-cm distance between both planes. The expertise acquired throughout the optimization studies has significant value, as the design of the system should be adaptable to different applications.

Monte Carlo simulations were also utilized to model realistic measurement cases. I developed software to derive representative results from the simulated data. This enabled me to have a realistic idea of the system capabilities in situations that I could not measure. The realistic simulation tool was validated with measurement data for both neutron and photon imaging. Validation results showed good agreement as the simulated and measured images presented the same features. The resulting agreement was further corroborated by the successful use of a simulated system matrix for MLEM.

Once we acquired equipment to build the prototype, I developed the software to operate the system, and tested it extensively. This system has the advantage of being build from relatively inexpensive, readily available parts. It is also particularly modular and scalable, with the current design aimed towards versatility rather than a particular application.

The prototype system was used to image spontaneous fission sources such as Cf-252, ( $\alpha$ ,n) sources such as AmBe, as well as radioisotope sources such as Cs-137. Sources were correctly imaged with both neutron and photon signals (only photon in the case of radioisotopes), and the energy spectra collected enabled source characterization. Various examples of dual-particle imaging with the two prototype systems operated are shown in chapter 4 and 5. The prototype system efficiency and field of view were investigated. The system yielded absolute efficiencies of  $10^{-6}$  for neutrons and  $10^{-5}$  for photons. The efficiency was sufficient to obtain both neutron and photon images in a reasonable time at any location. The neutron and photon efficiencies differ by less than an order of magnitude as no particle bias was included in the design.

Dual-particle imaging demonstrated its ability to decrease the impact of shielding, as lead and polyethylene shielded sources were imaged successfully [49]. The system was also operated successfully in the presence of various SNM. MOX and plutonium metal were measured during a measurement campaign in Ispra, Italy. The system has since been part of a measurement campaign at the Device Assembly Facility where it successfully imaged weapon-grade plutonium. Results from this campaign were not analyzed in this thesis.

A quantitative comparison to the other current and developing imaging systems is unfortunately hard to achieve. Performance metrics for other systems are not readily available, and do not necessarily paint the whole picture. Fig. 6-1 shows the capabilities of the DPI and other state-of-the-art systems. I have demonstrated in this work that the DPI system, while lacking

efficiency and having an average angular resolution, can image and get spectral information from both neutron and photons. This fact, coupled with a large field of view, makes it one of the most versatile imaging systems being developed. With the current software development, we effectively have a robust and versatile detection system, capable of imaging photons and fast neutrons in real time. This system can also be scaled and optimized to perform any nuclear nonproliferation task with relative ease, thanks to the different tools developed throughout this work. My graduate research oversaw this system go from the concept of dual-particle imaging to a full-fledged prototype that performs according to our aspirations.

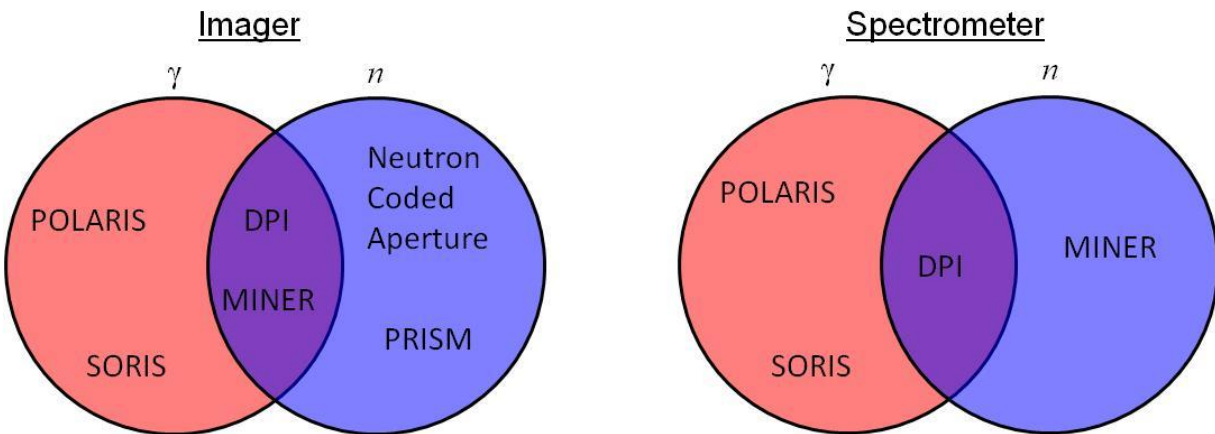


Fig. 6-1. Venn diagrams of current imaging systems.

## 6.2. Future Improvements

The optimization of the DPI system was carried out under constraints of the availability and cost of the equipment. Efficiency and angular resolution can be improved upon by a further monetary investment into the system. Efficiency can be increased by adding more detection material. While this is true of any detection system, it is particularly easy to perform for the DPI system given its scalability. The angular resolution can be decreased by changing the geometry of the system, as discussed in Chapter 5, and by using different detection material. Replacing the

NaI(Tl) scintillators with CZT crystals for example, would greatly improve the photon energy resolution, and thus the photon angular resolution, for a significant increase in price.

Further improvements could be made by using silicon photomultipliers instead of PMTs. This would not only reduce the amount of material particles have to go through to create a valid count, but also improve the time resolution of the system, thus improving neutron event reconstruction (for both energy and location) [50]. Silicon photomultipliers also offer the opportunity to pixelate the readout of the detector, and have position sensitivity within detector cells. This capability would further improve the angular resolution of the system, at the cost of more complex electronics. The EJ-309 liquid scintillators could also be replaced by solid scintillators with the same capabilities, such as stilbene [51] or the newly developed PSD-capable plastic scintillator [52]. Solid scintillators, while more expensive, should be more applicable to a rugged use of the DPI system.

Finally, a different evolution of the system could be the use of a single material to replace both EJ-309 and NaI(Tl) scintillators. Organic scintillators loaded with high-Z materials, such as tin-loaded polyvinyltoluene, bismuth-loaded polyvinylcarbazole or lead-loaded styrene, would be able to carry out this task [53]; the high-Z material can induce photoelectric absorptions on photons, and the organic scintillator PSD capabilities have been described previously. Such a system could then have a more uniform performance over the whole field of view.

The work presented in this thesis makes up the framework upon which the DPI system can expand. This inexpensive, scalable, and versatile system has proved its ability to image complex sources accurately and reliably. Advanced algorithms are now being used to characterize multiple sources within its field of view [54]. Along with the possible improvements of the DPI



system listed here, this project is an attractive alternative to the specialized imagers currently being researched.

## Appendices

### Appendix A – Sample MCNP input file

```
c DNNG: 2 MOX cannisters separated by 30 degree
c ~~~~~
c Cells
c ~~~~~
c Imager
c ~~~~~
c Front plane liquid
111 1 -0.935 -10 13 14 imp:n,p=1
112 like 111 but trcl=112
113 like 111 but trcl=113
c 114 broke, replaced with 3"
114 1 -0.935 -40 43 44 imp:n,p=1
121 like 111 but trcl=121
122 like 111 but trcl=122
123 like 111 but trcl=123
124 like 111 but trcl=124
131 like 111 but trcl=131
132 like 111 but trcl=132
133 like 111 but trcl=133
134 like 111 but trcl=134
141 like 111 but trcl=141
142 like 111 but trcl=142
143 like 111 but trcl=143
144 like 111 but trcl=144
c
c Front plane Al casing
150 9 -2.7 (-15:-16) 10 imp:n,p=1
151 like 150 but trcl=112
152 like 150 but trcl=113
c 153 like 150 but trcl=114
153 9 -2.7 -45 40 imp:n,p=1
154 like 150 but trcl=121
155 like 150 but trcl=122
156 like 150 but trcl=123
157 like 150 but trcl=124
158 like 150 but trcl=131
159 like 150 but trcl=132
160 like 150 but trcl=133
161 like 150 but trcl=134
162 like 150 but trcl=141
163 like 150 but trcl=142
164 like 150 but trcl=143
165 like 150 but trcl=144
c
c Front plane PMT
411 4 -0.51498 -12:-11 imp:n,p=1
412 like 411 but trcl=112
413 like 411 but trcl=113
414 like 411 but trcl=114
c 414 4 -0.51498 -42:-41 imp:n,p=1
421 like 411 but trcl=121
```

```

422 like 411 but trcl=122
423 like 411 but trcl=123
424 like 411 but trcl=124
431 like 411 but trcl=131
432 like 411 but trcl=132
433 like 411 but trcl=133
434 like 411 but trcl=134
441 like 411 but trcl=141
442 like 411 but trcl=142
443 like 411 but trcl=143
444 like 411 but trcl=144
c
c Back plane liquid
211 1 -0.935 -20 23 24 imp:n,p=1
212 like 211 but trcl=213
213 like 211 but trcl=222
214 like 211 but trcl=224
221 like 211 but trcl=231
222 like 211 but trcl=233
223 like 211 but trcl=242
224 like 211 but trcl=244
c
c Back plane casing
251 9 -2.7 -25 20 imp:n,p=1
252 like 251 but trcl=213
253 like 251 but trcl=222
254 like 251 but trcl=224
255 like 251 but trcl=231
256 like 251 but trcl=233
257 like 251 but trcl=242
258 like 251 but trcl=244
c
c Back plane PMT
511 4 -0.51498 -22:-21 imp:n,p=1
512 like 511 but trcl=213
513 like 511 but trcl=222
514 like 511 but trcl=224
521 like 511 but trcl=231
522 like 511 but trcl=233
523 like 511 but trcl=242
524 like 511 but trcl=244
c
c Back plane NaI
311 2 -3.67 -30 imp:n,p=1
312 like 311 but trcl=314
313 like 311 but trcl=321
314 like 311 but trcl=323
321 like 311 but trcl=332
322 like 311 but trcl=334
323 like 311 but trcl=341
324 like 311 but trcl=343
c
c Back plane NaI Casing
351 9 -2.7 -33 30 imp:n,p=1
352 like 351 but trcl=314
353 like 351 but trcl=321
354 like 351 but trcl=323
355 like 351 but trcl=332
356 like 351 but trcl=334
357 like 351 but trcl=341
358 like 351 but trcl=343
c
c Back plane NaI PMT

```

```

611 4 -0.51498 -32:-31 imp:n,p=1
612 like 611 but trcl=314
613 like 611 but trcl=321
614 like 611 but trcl=323
621 like 611 but trcl=332
622 like 611 but trcl=334
623 like 611 but trcl=341
624 like 611 but trcl=343
c
c Front plane Window
711 8 -2.51 -13:-14 imp:n,p=1
712 like 711 but trcl=112
713 like 711 but trcl=113
714 like 711 but trcl=114
721 like 711 but trcl=121
722 like 711 but trcl=122
723 like 711 but trcl=123
724 like 711 but trcl=124
731 like 711 but trcl=131
732 like 711 but trcl=132
733 like 711 but trcl=133
734 like 711 but trcl=134
741 like 711 but trcl=141
742 like 711 but trcl=142
743 like 711 but trcl=143
744 like 711 but trcl=144
c
c Back Plane Window
766 8 -2.51 -23:-24 imp:n,p=1
767 like 766 but trcl=213
768 like 766 but trcl=222
769 like 766 but trcl=224
776 like 766 but trcl=231
777 like 766 but trcl=233
778 like 766 but trcl=242
779 like 766 but trcl=244
c
c
c ~~~~~
c Imager Structure?
c ~~~~~
c
c ~~~~~
c Ground
c ~~~~~
903 10 -2.3 -500 -61 imp:N,P=1 $ concrete floor
c ~~~~~
c MOX1 Source
c ~~~~~
801 0 -73 87 -82 imp:n,p=1 $vacuum on top of powder
802 11 -0.7 -73 81 -87 imp:n,p=1 $MOX powder
803 12 -7.92 73 -74 81 -82 imp:n,p=1 $inner steel cylinder
804 12 -7.92 -74 80 -81 imp:n,p=1 $steel inner bottom
805 12 -7.92 -74 82 -83 imp:n,p=1 $steel inner top
806 0 74 -75 80 -83 imp:n,p=1 $surrounding vacuum cylinder
807 0 -75 79 -80 imp:n,p=1 $bottom vacuum
808 0 -75 83 -84 imp:n,p=1 $top vacuum
809 0 -72 84 -85 imp:n,p=1 $another top vacuum
810 12 -7.92 75 -76 79 -84 imp:n,p=1 $outer steel cylinder
811 12 -7.92 -76 89 -79 imp:n,p=1 $steel outer bottom
812 12 -7.92 72 -77 84 -85 imp:n,p=1 $steel cylinder top
813 12 -7.92 -77 85 -86 imp:n,p=1 $steel outer top
814 6 -11.34 -51 76 -84 52 imp:N,P=1 $lead shield

```

```

c ~~~~~
c MOX2 Source
c ~~~~~
821 0 -93 87 -82 imp:n,p=1 $vacuum on top of powder
822 13 -0.79807 -93 81 -87 imp:n,p=1 $MOX powder
823 12 -7.92 93 -94 81 -82 imp:n,p=1 $inner steel cylinder
824 12 -7.92 -94 80 -81 imp:n,p=1 $steel inner bottom
825 12 -7.92 -94 82 -83 imp:n,p=1 $steel inner top
826 0 94 -95 80 -83 imp:n,p=1 $surrounding vacuum cylinder
827 0 -95 79 -80 imp:n,p=1 $bottom vacuum
828 0 -95 83 -84 imp:n,p=1 $top vacuum
829 0 -92 84 -85 imp:n,p=1 $another top vacuum
830 12 -7.92 95 -96 79 -84 imp:n,p=1 $outer steel cylinder
831 12 -7.92 -96 89 -79 imp:n,p=1 $steel outer bottom
832 12 -7.92 92 -97 84 -85 imp:n,p=1 $steel cylinder top
833 12 -7.92 -97 85 -86 imp:n,p=1 $steel outer top
834 6 -11.34 -53 96 -84 52 imp:n,p=1 $lead shield
c ~~~~~
c Environment
c ~~~~~
902 3 -1.205E-3 52 -76 -89 imp:n,p=1
904 3 -1.205E-3 52 -96 -89 imp:n,p=1
901 3 -1.205E-3 -500 61 #813 (-52 :51 :84 )
(77 :-84 :86 ) #833 (-52 :53 :84 )
(97 :-84 :86 ) 10 11 12 15 16 20 21 22 25 30 31 32 33
#111 #112 #113 #114 #121 #122 #123 #124
#131 #132 #133 #134 #141 #142 #143 #144
#150 #151 #152 #153 #154 #155 #156 #157
#158 #159 #160 #161 #162 #163 #164 #165
#411 #412 #413 #414 #421 #422 #423 #424
#431 #432 #433 #434 #441 #442 #443 #444
#211 #212 #213 #214 #221 #222 #223 #224
#251 #252 #253 #254 #255 #256 #257 #258
#511 #512 #513 #514 #521 #522 #523 #524
#311 #312 #313 #314 #321 #322 #323 #324
#351 #352 #353 #354 #355 #356 #357 #358
#611 #612 #613 #614 #621 #622 #623 #624
#711 #712 #713 #714 #721 #722 #723 #724
#731 #732 #733 #734 #741 #742 #743 #744
#766 #767 #768 #769 #776 #777 #778 #779
imp:n,p=1
999 0 500 imp:N,P=0
c ~~~~~
c Surfaces
c ~~~~~
c Imager
c ~~~~~
10 RCC -22.5 -222.7 22.5 0.0 -6.3 0.0 3.81 $Front plane Liquid
11 RCC -22.5 -222.065 22.5 0.0 6.5 0.0 3.81 $Front plane PMT Thick
12 RCC -22.5 -215.565 22.5 0.0 17.2 0.0 2.94 $Front plane PMT skinny
13 RCC -22.5 -222.7 22.5 0.0 -1.2 0.0 3.25 $Front plane window thick
14 RCC -22.5 -222.7 22.5 0.0 0.635 0.0 3.9075 $Front plane window skinn
15 RCC -22.5 -222.7 22.5 0.0 -.64 0.0 4.2995 $Casing Lip
16 RCC -22.5 -222.7 22.5 0.0 -6.452 0.0 3.962 $Casing
c
20 RCC -37.5 -259.0 37.5 0.0 -9.2 0.0 3.81 $Middle Liquid scintillator
21 RCC -37.5 -268.835 37.5 0.0 -6.5 0.0 3.81 $Middle PMT thick
22 RCC -37.5 -275.335 37.5 0.0 -17.2 0.0 2.94 $Middle PMT skinny
23 RCC -37.5 -268.2 37.5 0.0 1.6 0.0 3.25 $Front plane window thick
24 RCC -37.5 -268.835 37.5 0.0 0.635 0.0 3.9075 $Front plane window skin
25 RCC -37.5 -258.848 37.5 0.0 -9.352 0.0 3.962 $Casing
c

```

```

30 RCC -12.5 -260.9 37.5 0.0 -7.62 0.0 3.81 $NaI scintillator
31 RCC -12.5 -268.52 37.5 0.0 -4.0 0.0 3.81 $Front part of NaI PMT
32 RCC -12.5 -272.52 37.5 0.0 -14.0 0.0 2.94 $Back part of NaI PMT
33 RCC -12.5 -260.748 37.5 0.0 -7.772 0.0 3.962 $Casing
c
40 RCC 22.5 -222.7 22.5 0.0 -9.2 0.0 3.81 $Front plane 3" liquid
41 RCC -22.5 -222.065 22.5 0.0 6.5 0.0 3.81 $Front plane PMT Thick
42 RCC -22.5 -215.565 22.5 0.0 17.2 0.0 2.94 $Front plane PMT skinny
43 RCC 22.5 -222.7 22.5 0.0 -1.6 0.0 3.25 $Front plane 3" window thic
44 RCC 22.5 -222.7 22.5 0.0 0.635 0.0 3.9075 $ Front plane 3" window s
45 RCC 22.5 -222.7 22.5 0.0 -9.352 0.0 3.962 $Casing
c ~~~~~
c Lead Shielding
c ~~~~~
51 C/Z -65.38 -2.5 6.4 $outer cylinder
53 C/Z 65.38 -2.5 6.4 $outer cylinder
52 PZ -16.25 $bottom of Pb
c ~~~~~
c Ground
c ~~~~~
61 PZ -108 $ Floor level
c ~~~~~
c MOX Source Container
c ~~~~~
72 C/Z -65.38 -2.5 5.1 $Support cylinder outer and upper empty space cylin
73 C/Z -65.38 -2.5 4.14 $inner container cylinder inner wall
74 C/Z -65.38 -2.5 4.445 $inner container cylinder outer wall
75 C/Z -65.38 -2.5 5.2 $outer container cylinder inner wall
76 C/Z -65.38 -2.5 5.4 $outer container cylinder outer wall
77 C/Z -65.38 -2.5 6.75 $top steel cylinder
92 C/Z 65.38 -2.5 5.1 $Support cylinder outer and upper empty space cylin
93 C/Z 65.38 -2.5 4.14 $inner container cylinder inner wall
94 C/Z 65.38 -2.5 4.445 $inner container cylinder outer wall
95 C/Z 65.38 -2.5 5.2 $outer container cylinder inner wall
96 C/Z 65.38 -2.5 5.4 $outer container cylinder outer wall
97 C/Z 65.38 -2.5 6.75 $top steel cylinder
79 PZ -14.0982 $outer container - BOTTOM
80 PZ -13.8982 $inner container outer surf
81 PZ -13.3982 $inner container inner surf
82 PZ 13.4018 $inner container inner surf
83 PZ 13.9018 $inner container outer surf
84 PZ 14.1018 $outer container
85 PZ 16.1018 $outer container
86 PZ 18.1018 $outer container
87 PZ 13.4017 $top of PuO powder
89 PZ -15.0982 $bottom
c ~~~~~
c Imager Structure?
c ~~~~~
c
c ~~~~~
c Environment
c ~~~~~
500 RPP -500 500 -800 200 -500 500

c ~~~~~
c Data
c ~~~~~
c
c ~~~~~
c Physics
c ~~~~~
MODE n p

```

```

PHYS:N J 20
CUT:P 2J 0
c ~~~~~
c Source
c ~~~~~
SDEF cel=d1 pos=FCEL d2 axs=0 0 1 rad=d5 ext=d6 erg=FCEL d7 tme= d10
c Source Cell
SI1 L 802 822
SP1 0.4682 0.5318
c Source Position
DS2 S 3 4
SI3 L -65.38 -2.5 -13.39
SP3 1
SI4 L 65.38 -2.5 -13.39
SP4 1
c Source Radius
SI5 0 4.14
c Source Height
SI6 0 26.79
c Source Energy
DS7 S 8 9
c MOX1
SI8 L 2 3 4 -38 -39 -40 -41
SP8 0.000086 0.416539 0.050756 0.058827 0.079966 0.124374 0.264248
c MOX2
SI9 L 2 3 4 -38 -39 -40 -41
SP9 0.000087 0.416538 0.050755 0.058827 0.079966 0.124373 0.264247
c Source Time
SI10 0 720000000000
c MOX 25 measurement time: 120 min
SP10 0 1
IPOL 99 1 2 1 J 2 88 111 112 113 114 121 122 123 124
131 132 133 134 141 142 143 144
411 412 413 414 421 422 423 424
431 432 433 434 441 442 443 444
211 212 213 214 221 222 223 224
511 512 513 514 521 522 523 524
311 312 313 314 321 322 323 324
611 612 613 614 621 622 623 624
711 712 713 714 721 722 723 724
731 732 733 734 741 742 743 744
766 767 768 769 776 777 778 779
NPS 81265678 $ 1.12868997136e+05 per sec (aged MOX src)
FILES 21 DUMN1
DBCN
PRDMP 2J 1
c ~~~~~
c Materials
c ~~~~~
c EJ-309 liquid scintillator d=-0.916
c (Eljen Technologies, EJ-309 Fact Sheet)
c Liquid Scintillator
m1 NLIB=70c PLIB=04p
1001 0.555443 $ H
6000.70c 0.444557 $ C
c
c NaI Scintillator
m2 NLIB=70c PLIB=04p
11023 -0.153373 $ Na
53127 -0.846627 $ I
c
c Air
m3 NLIB=70c PLIB=04p

```

```

7014 -0.755636 $ N
8016 -0.231475 $ O
18040 -0.012838 $ Ar-40 at 99.6035 percent of natural Ar
18036 -0.000043 $ Ar-36 at 0.3336 percent of natural Ar
18038 -0.000008 $ Ar-38 at 0.00629 percent of natural Ar
c
c Homogenized PMT
m4 NLIB=70c PLIB=04p
14000.60c -0.0933168 $Si
8016 -0.1312437 $Oxy
5010 -0.0079926 $B
11023 -0.0096386 $Na
13027 -0.0040993 $Al
26000.55c -0.2481451 $Fe
28000.50c -0.5049603 $Ni
7014 -0.0005934 $N
18040 -1.008186e-5 $Ar-40 at 99.6035 percent of natural Ar
18036 -3.376699e-8 $Ar-36 at 0.3336 percent of natural Ar
18038 -6.366738e-9 $AR-38 at 0.00629 percent of natural Ar
c
c Poly
m5 NLIB=70c PLIB=04p
1001 -0.14371 $H
6000.70c -0.856284 $C
c
c Lead
m6 NLIB=70c PLIB=04p
82204.70c -0.014 $Pb
82206.70c -0.241
82207.70c -0.221
82208.70c -0.524
c
c Polystyrene
m7 NLIB=70c PLIB=04p
1001 0.499994
6000.70c 0.500006
c
c BK7
m8 NLIB=70c PLIB=04p
14028 -0.323138999
8016 -0.483882614
5011 -0.033384805
56138 -0.027496631
11023 -0.077153875
19039 -0.052216449
33075 -0.002726626
c ~~~~~
c Aluminum table d=-2.70
c ~~~~~
m9 nlib=70c plib=04p
13027 -1
c ~~~~~
c Concrete (Mat. Compendium PNNL) d=-2.3
c (Mat. Compendium PNNL)
c ~~~~~
m10 nlib=70c plib=04p
1001 -0.022100
6000 -0.002484
8016 -0.574930
11023 -0.015208
12000 -0.001266
13027 -0.019953
14000.60c -0.304627

```



```

19000      -0.010045
20000      -0.042951
26000.42c -0.006435
c ~~~~~
c MOX sample d=-0.7
c (ENEA-01)
c ~~~~~
m11  nlib=60c  plib=04p
    94238.42c  -0.000229
    94239      -0.109720
    94240      -0.046112
    94241      -0.001529
    94242      -0.003317
    95241.61c  -0.005135
    92234      -0.000053
    92235      -0.004737
    92236      -0.000053
    92238      -0.663328
    8016       -0.165786
c ~~~~~
c Steel
c ~~~~~
m12  nlib=70c  plib=04p
    26000.55c -0.6950
    24000.50c -0.1900
    28000.50c -0.0950
    25055.51c -0.0200
c ~~~~~
c MOX sample d=-0.79807
c (ENEA-02)
c ~~~~~
m13  nlib=60c  plib=04p
    94238.42c  -0.000229
    94239      -0.109431
    94240      -0.045990
    94241      -0.001525
    94242      -0.003308
    95241.61c  -0.005122
    92234      -0.000054
    92235      -0.004773
    92236      -0.000054
    92238      -0.668350
    8016       -0.161165
c ~~~~~
c Tallies
c ~~~~~
c
c ~~~~~
c Translations
c ~~~~~
c Front Plane Translations
tr112 15  0.0  0.0
tr113 30  0.0  0.0
tr114 45  0.0  0.0
tr121 0.0  0.0 -15
tr122 15  0.0 -15
tr123 30  0.0 -15
tr124 45  0.0 -15
tr131 0.0  0.0 -30
tr132 15  0.0 -30
tr133 30  0.0 -30
tr134 45  0.0 -30
tr141 0.0  0.0 -45

```

```

tr142 15 0.0 -45
tr143 30 0.0 -45
tr144 45 0.0 -45
c
c Back Plane Liquid Translations
tr213 50 0.0 0.0
tr222 25 0.0 -25
tr224 75 0.0 -25
tr231 0.0 0.0 -50
tr233 50 0.0 -50
tr242 25 0.0 -75
tr244 75 0.0 -75
c
c Back Plane NaI Translations
tr314 50 0.0 0.0
tr321 -25 0.0 -25
tr323 25 0.0 -25
tr332 0.0 0.0 -50
tr334 50 0.0 -50
tr341 -25 0.0 -75
tr343 25 0.0 -75
c
c Back Plane Liquid Translations
tr413 50 -54 0.0
tr422 25 -54 -25
tr424 75 -54 -25
tr431 0.0 -54 -50
tr433 50 -54 -50
tr442 25 -54 -75
tr444 75 -54 -75
c
c ~~~~~

```

## Appendix B – Sample MPPost Input file

```
# ~~~~~
# ~~~~~
#
# Input file for MPPost
#
version                2.1.9
# ~~~~~
# ~~~~~

# ~~~~~
# GENERAL INFORMATION
# ~~~~~
title                  TEST
username               MLR

# ~~~~~
# I/O FILE INFORMATION
# ~~~~~
polimi_det_in          Measurements.dat # MCNP-PoliMi detector filename
import_pulses         no                # If processing pulse list (from measurements or
simulation) turn to yes
output_file            IspraSystem      # Desired output name
label_output          yes                # Place labels at the top of the output files
separate_det_response yes                # Print individual distributions for each
detector
list_of_pulses        no                # Print a list mode file of all collected pulses
incident_light        no                # Data written to list of pulses no = incident
energy (MeV)
# yes = write the max potential LIGHT (MeVee)
event_inventory_on    no                # Print out a table summarizing all events in the
file
collision_history     no                # Print summary of how collisions make pulses in
the detector
time_file_on         no                # Use TIME file to obtain start times for each
history
time_file_name        # Name of the TIME file
overwrite_files       yes                # Allow the code to overwrite old files
comma_delimited       yes                # Output files delimited by a comma

# ~~~~~
# MEMORY
# ~~~~~
division_size         50000 # MB, size of segments to divide the file
cushion               200    # number of lines added to the arrays to prevent overstepping
arrays

# ~~~~~
# DETECTOR INFORMATION
# ~~~~~
time_dependent        yes                # Perform analysis by time instead of by
history
NPS                   1                # NPS used in the MCNP run
detector_type         1 1 4 0 0 0 0 0 # Type of Detector - list for each cell
number
# 0 = Non Active Volume (i.e. PMT)
# 1 = Liquid Organic Scintillator
# 2 = He3 (Cannot be run with other types)
# 3 = Plastic Organic Scintillator
# 4 = NaI
# 5 = CaF2
```

```

#      6 = LaBr3
threshold          0.05 0.05 0.05      # MeVee, Threshold for event detection - list
for each cell number
upper_threshold    3.18 3.18 3.18      # MeVee, the max acceptable light for event
detection - list for each cell number
detector_cell_numbers ( 111 112 113 114 121 122 123 124 131 132 133 134 141 142 143
144 ) &
                ( 211 212 213 214 221 222 223 224 ) &
                ( 311 312 313 314 321 322 323 324 ) &
                ( 411 412 413 414 421 422 423 424 431 432 433 434 441 442 443
444 ) &
                ( 511 512 513 514 521 522 523 524 ) &
                ( 611 612 613 614 621 622 623 624 ) &
                ( 711 712 713 714 721 722 723 724 731 732 733 734 741 742 743
744 ) &      # Cell numbers of the detectors
                ( 766 767 768 769 776 777 778 779 )
# NOTE: To group cells add ( ) around the group.

# There must be a space before and after each (

# ~~~~~
# Capture Neutron Profile ( Works in CLYC cells)
# ~~~~~
ncp_on              no                  # yes/no, option to
produce a phd based on the energy released in each capture (on automatically for clyc)
ncp_low            0                    # MeV, lower
recorded neutron energy value
ncp_high          5                    # MeV, upper recorded
neutron energy value
ncp_incr          0.1                  # MeV, bin width for
recorded neutron energy values
capture_material   3007,5010           # List zaid for materials relevent
caputre_events can occur in, up to 10

# ~~~~~
# DETECTOR INFORMATION - Pulse Height
# ~~~~~
pulse_height_on    no                  # Print pulse height distributions
sum_then_light     no                  # Convert the sum of all contributing
particles energy to light
cross_talk_on      no                  # Eliminate histories with cross talk

# Pulse Generation Time - ns, Light collection time for a pulse
organic_liq_pgt    10
organic_pl_pgt     10
nai_pgt           10
caf2_pgt          10
labr3_pgt         10
clyc_pgt          10

# Deadtime - ns, deadtime of the detector between pulses
organic_liq_dt     0
organic_pl_dt      0
nai_dt            0
caf2_dt           0
labr3_dt          0
clyc_dt           0

histogram_start    0                    # MeVee, Min value for the pulse height
distribution
histogram_stop     10                   # MeVee, Max value for the pulse height
distribution
bin_step           0.01                 # MeVee, Bin step - top side of the bin

```

```

# ~~~~~
# ORGANIC SCINTILLATOR
# ~~~~~
calibration_regions 1 # Number of independently fit
neutron light regions
region_type 3 # Specify which form for the
coefficients, if multiple regions list selections # Type Form How to

enter values on the neutron_calibration line #
B C # 1 = Ax^2+Bx+C -> E1 E2 A
B # 2 = Ax^2/(x+B) -> E1 E2 A
B # 3 = A(Bx-C(1-exp(Dx^E)))
-> E1 E2 A B C D E # Where E1 and E2 are the

lower and upper energy bounds respectively in MeVee #
neutron_calibration 0 50 1 0.81723 2.6290 -0.29686 1 # Neutron Calibration - see
above for entry instructions #
# 0.8 1 0 0 0.03495 0.1424 -0.036 & # For multiple regions add
an '&' to the end of the line and continue next region #
# 1 50 0 0 0.03495 0.1424 -0.036 # on the next line
photon_calibration 1.000 0.000 # A,B: Parameters for photon
light conversion - Ax+B #
carbon_light_constant 0.02 # Constant value for carbon
light conversion #
deuterium_fit_type 2 # Specify which form for the
coefficients for deuterium light conversion: 1 or 2 #
deuterium_calibration 1 0.74692 3.5522 -0.1977 1 # Enter coefficients for
chosen deuterium fit type #
# 1 = Ax^4+Bx^3+Cx^2+Dx+E -
# 2 = A(Bx-C(1-exp(Dx^E))) -

> A B C D E #
> A B C D E #
clyc_n_calib .6465 # Constant value for light
conversion for capture events in CLYC

# ~~~~~
# Energy Resolution
# ~~~~~
light_resolution_on yes # Turns on/off the a Gaussian Energy
Broadening
organic_liq_p_lgt 9.8532 0 4738.66 # Coefficients A,B,C for Gaussian
Broadening: A*LO+B*Sqrt(LO)+C
organic_liq_n_lgt 9.8532 0 4738.66
organic_pl_p_lgt 10.083 311.77 431.58
organic_pl_n_lgt 10.083 311.77 431.58
nai_lgt # For Inorganics leave blank to use defaults
caf2_lgt # or specify Coefficients as
labr3_low_lgt # Coefficients A,B,C for Gaussian Broadening:
A*LO+B*Sqrt(LO)+C
labr3_high_lgt
clyc_lgt 3.6218 -79.1285 3092.1

# ~~~~~
# Time Resolution
# ~~~~~
tme_resolution_on yes # Turns on time broadening
organic_liq_tme 1
organic_pl_tme 1
nai_tme 10
caf2_tme 24

```

```

labr3_tme          1
clyc_tme

# ~~~~~
# Voxels
# ~~~~~
cell_voxels_on    yes
cells_to_voxel    111          211          311          # Cell
numbers that are to be voxeled
xVox              -30  15  30   -50  25  50   -50  25  50   # Start,
step, max for voxelation
yVox              -229  6.3 -222.7 -268.2 9.2 -259 -268.52 7.62 -260.9 #
for multiple cells repeat start,step,stop
zVox              -30  15  30   -50  25  50   -50  25  50   #
start1,step1,stop1,start2,step2,stop2

# ~~~~~
# TIME-OF-FLIGHT, CORRELATION, and AUTOCORRELATION INFORMATION
# ~~~~~
tof_on            no          # yes/no, Turn on TOF distributions (cannot have a
start detector)
cross_correlation_on no      # yes/no, Turn on cross correlation function
auto_correlation_on no      # yes/no, Turn on auto correlation function
start_detector    100       # Cell number of the start detector
time_start        -100.5    # ns, time for the correlation plot to start (NOTE:
there has to be a decimal point, even if it is just 100.0)
time_stop         100.5    # ns, time for the correlation plot to stop (NOTE:
there has to be a decimal point, even if it is just 100.0)
time_increment    1        # ns, time increment between the bins - top side of
the bin
cc_window_incr    1000     # ns, time window for correlation events for time
dependent analysis
# ~~~~~
# Pulse Height Correlation
# ~~~~~
pulse_correlation_on no      # yes/no, turn on pulse height correlation analysis
pc_min            0        # MeVee, Minimum value for pulse height binning
pc_max            5        # MeVee, Maximum value for pulse height binning
pc_incr           0.05     # MeVee, increment for pulse height binning
stop_pulse_only   yes      # Ignore start detector pulse height
# ~~~~~
# CAPTURE GATED DETECTORS
# ~~~~~
capture_gate_on   no        # Run the capture gated detector response
cap_low           0        # ns, start time for binning the time to capture
histogram
cap_high          2000     # ns, stop time for binning the time to capture
histogram
cap_incr          10       # ns, bin size the time to capture histogram

# ~~~~~
# IMAGING SYSTEM
# ~~~~~
imaging_system_on yes      # yes/no, turn on the imaging system
longdistance      yes      # yes/no, turn on long distance
window_front      5        # Time window used to discriminate double scatters in plane
1 for neutrons
window_start      5        # (implemented before and after the trigger)
                    # Start of time window used to correlate neutrons
window_end        100     # Time window used to correlate neutrons
window_gamma      25      # Time window used to correlate gammas
                    # (implemented before and after the trigger)
backprojection    yes      # yes/no, run back projection algorithm

```

```

sphere_center      0 0 0    # X, Y, and Z coordinates of the center of the back
projection sphere
sphere_radius      250    # Radius of the back projection sphere
sphere_mesh        2      # Degrees per mesh point
cone_thickness     2      # Thickness of the back projection cones
mlem_input_data    yes    # yes/no, outputs data to use with MLEM algorithm
mlem_angle_bin     10     # Angle binning used for MLEM
p_emin            0      # Min cutoff energy in MeVee for back projection imaging
photons & MLEM
p_ekin            0.1     # Energy Binning in MeVee for back projection imaging
photons & MLEM
p_emax            5      # Max cutoff energy in MeVee for back projection imaging
photons & MLEM
n_emin            0      # Min cutoff energy in MeVee for back projection imaging
neutrons & MLEM
n_ekin            1      # Energy Binning in MeVee for back projection imaging
neutrons & MLEM
n_emax            15     # Max cutoff energy in MeVee for back projection imaging
neutrons & MLEM
uncertaintythickness no    # yes/no
distancecheck      no    # yes/no

# ~~~~~
# He3 MODULE
# ~~~~~
he3_multiplicity   no    # yes/no: Turn on the He3 module
number_of_windows  256   # Number of windows to evaluate
window_increment   16    # Window increment in microseconds
deadtime_type      1     # Control which model is applied for dead time
# 1 = Type I, applied to each tube only
# 2 = Type II, applied to each tube then fed into an
amplifier          # 3 = Type III, AWCC style, detector, into amp, into OP
amp
detector_deadtime  4     # Detector dead time in microseconds
amplifier_deadtime 0.5   # Level I amplifier dead time in microseconds
amp_2_deadtime     0.03  # Level II amplifier dead time in microseconds
max_multiplicity   500   # Maximum multiplicity expected (for array size handling)
trigger_type       1     # Control how the multiplicity windows are triggered
# 1 = Constant window
# 2 = Open on trigger (Reverse)
# 3 = Open on trigger (Forward)
pre_delay          4.5   # Predelay after event trigger in microseconds
long_delay         1024  # Delay between R+A window and A window in microseconds
run_time           105.33 # Time the source is distributed over in seconds
output_style       3     # Controls what data is printed to a file
# 1 = All multiplicity distributions + Feynman-Y + S,D,T
# 2 = Last multiplicity distribution + S,D,T rates
# 3 = Last multiplicity distribution + Mean, Variance,
Feynman-Y
generation_analysis_on yes # yes/no, analysis of the neutron generations captured
paralyzable        no    # yes/no, yes treats He-3 detectors as paralyzable, no
treated as non-paralyzable
# ~~~~~
# Select Capture Event Type
# ~~~~~
output_sort_file   no    # Print out a file with all sorted events
sort_ipt           1     # Particle type to sort by, set -1 to ignore
sort_nxs           2003  # Material of interaction to sort by, set to -1 to ignore
sort_ntyn         0     # Interaction type to sort by, set to -1 to ignore

# ~~~~~
# Scintillator Multiplicity MODULE

```

```

# ~~~~~
scint_mult      no      # Turn on Scintillator Multiplicity
neutrons_only  no      # Only process neutron multiplicities (i.e. np -> n and
nppp -> nn)
digitizer_window 480    # ns, Length of the digitizer window
digitizer_gap    16     # ns, Delay between successive digitizer windows
digitizer_end    220    # ns, Time at end of digitizer window where pulses are not
seen
digitizer_lag    80     # ns, Time at the beginning of digitizer window before a
pulse can be seen
sm_dist_on      yes     # yes/no, Pulse height distributions for each multiplicity
combination

# ~~~~~
# Variance Reduction
# ~~~~~
apply_weight    no      # yes/no, use the non-unity weights of particles

```



## Appendix C – MPPost source code extract

```
Subroutine Imaging_correlation
!
!~~~~~
! V 4.0
! This subroutine correlates interactions within the different detectors
! declared
! Also contains the following additional subroutines and functions used
! locally in Imaging_correlation:
! - MLEM_input
! - Backprojection
!
!~~~~~

use parameters_m
use Imaging_system_m
use Pulse_Height_m
use Main_m

character(len=12)::VoxelString
integer:: iReIndex, iCorrel, iNeutron, iPhoton, iTime, DoubleScatter,
Correlated
integer:: idealPCounts, idealNCounts, COUNTN1, COUNTN2, COUNT1, COUNT2,
COUNT3, IDEALN1, IDEALN2, IDEAL1, IDEAL2, IDEAL3
!$$$$$ integer:: CAUSE1, CAUSE2, CAUSE21, CAUSE22, CAUSE3, CAUSE4
real(kind=8), allocatable, dimension(:,)::temp
type(Pulses), allocatable, dimension(:):: Neutron, Photon
integer, dimension(3)::PlaneMat
real::ReverseBirks

real::X1, Y1, Z1, X2, Y2, Z2, X3, Y3, Z3
real::E1, E2, secaxis(3), costeta2, ETOF
real::A, B, C, D, E, low_limit, high_limit
real::WAPR
integer::iBackPro, iEnergy, NERROR

real::R2, theta, phi, errorInScatter, errorInAbsorbption, angleUncertaintyGeometry
real::energyRes1, energyRes2, angleUncertaintyEnergy

iNeutron = 1
iPhoton = 1

allocate (Neutron (Pulse_key-1), Photon (Pulse_key-1), temp (200, 9))

if (psd_imaging==.TRUE.) then
  do iReIndex = 1, Pulse_key-1
    of the Pulse_Data (separation of neutrons and photons)
      ! Re-indexation
      if (Pulse_data(iReIndex,3)==1) then
        if (import_pulses == .FALSE.) then
          Pulse_data(iReIndex,10) =
Detectors (Pulse_data(iReIndex,1))%Cell
        endif
      endif
    enddo
  enddo
enddo
```

```

write(VoxelString, ' (I12.12) ') int(Pulse_data(iReIndex,10),8)
!write(*,*) ''
!write(*,*) VoxelString(1:3)
!write(*,*) VoxelString(4:6)
!write(*,*) VoxelString(7:9)
!write(*,*) VoxelString(10:12)
!write(*,*) ''
read(VoxelString(1:3),*) Neutron(iNeutron)%Plane
read(VoxelString(4:6),*) Neutron(iNeutron)%X
read(VoxelString(7:9),*) Neutron(iNeutron)%Y
read(VoxelString(10:12),*) Neutron(iNeutron)%Z
Neutron(iNeutron)%Energy=Pulse_data(iReIndex,5)
Neutron(iNeutron)%Time=Pulse_data(iReIndex,2)
Neutron(iNeutron)%History=Pulse_data(iReIndex,4)
Neutron(iNeutron)%ParticleNumber=Pulse_data(iReIndex,7)
Neutron(iNeutron)%InteractionNumber=Pulse_data(iReIndex,8)
if (import_pulses == .FALSE.) then

PlaneMat(Neutron(iNeutron)%Plane)=Detectors(Pulse_data(iReIndex,1))%det_type
endif
iNeutron = iNeutron + 1

elseif (Pulse_data(iReIndex,3)==2) then
if (import_pulses == .FALSE.) then
Pulse_data(iReIndex,10) =
Detectors(Pulse_data(iReIndex,1))%Cell
endif
write(VoxelString, ' (I12.12) ') int(Pulse_data(iReIndex,10),8)
!write(*,*) ''
!write(*,*) VoxelString(1:3)
!write(*,*) VoxelString(4:6)
!write(*,*) VoxelString(7:9)
!write(*,*) VoxelString(10:12)
!write(*,*) ''
read(VoxelString(1:3),*) Photon(iPhoton)%Plane
read(VoxelString(4:6),*) Photon(iPhoton)%X
read(VoxelString(7:9),*) Photon(iPhoton)%Y
read(VoxelString(10:12),*) Photon(iPhoton)%Z
Photon(iPhoton)%Energy=Pulse_data(iReIndex,5)
Photon(iPhoton)%Time=Pulse_data(iReIndex,2)
Photon(iPhoton)%History=Pulse_data(iReIndex,4)
Photon(iPhoton)%ParticleNumber=Pulse_data(iReIndex,7)
Photon(iPhoton)%InteractionNumber=Pulse_data(iReIndex,8)
if ((liqDPI == .true.) .and. (Photon(iPhoton)%Plane==2)) then
Photon(iPhoton)%Plane = 3
endif
if (import_pulses == .FALSE.) then

PlaneMat(Photon(iPhoton)%Plane)=Detectors(Pulse_data(iReIndex,1))%det_type
endif
iPhoton = iPhoton + 1
endif

enddo
else

```

```

do iReIndex = 1, Pulse_key-1                                ! Re-indexation
of the Pulse_Data (no separation of neutrons and photons under given
threshold)
  if (import_pulses == .FALSE.) then
    Pulse_data(iReIndex,10) = Detectors(Pulse_data(iReIndex,1))%Cell
  endif
  write(VoxelString,'(I12.12)') int(Pulse_data(iReIndex,10),8)
  !write(*,*) ''
  !write(*,*) VoxelString(1:3)
  !write(*,*) VoxelString(4:6)
  !write(*,*) VoxelString(7:9)
  !write(*,*) VoxelString(10:12)
  !write(*,*) ''
  if ((Pulse_data(iReIndex,5)<PSDthresh) .OR.
(Pulse_data(iReIndex,3)==1)) then
    read(VoxelString(1:3),*) Neutron(iNeutron)%Plane
    read(VoxelString(4:6),*) Neutron(iNeutron)%X
    read(VoxelString(7:9),*) Neutron(iNeutron)%Y
    read(VoxelString(10:12),*) Neutron(iNeutron)%Z
    Neutron(iNeutron)%Energy=Pulse_data(iReIndex,5)
    Neutron(iNeutron)%Time=Pulse_data(iReIndex,2)
    Neutron(iNeutron)%History=Pulse_data(iReIndex,4)
    Neutron(iNeutron)%ParticleNumber=Pulse_data(iReIndex,7)
    Neutron(iNeutron)%InteractionNumber=Pulse_data(iReIndex,8)
    iNeutron = iNeutron + 1
  endif
  if ((Pulse_data(iReIndex,5)<PSDthresh) .OR.
(Pulse_data(iReIndex,3)==2)) then
    read(VoxelString(1:3),*) Photon(iPhoton)%Plane
    read(VoxelString(4:6),*) Photon(iPhoton)%X
    read(VoxelString(7:9),*) Photon(iPhoton)%Y
    read(VoxelString(10:12),*) Photon(iPhoton)%Z
    Photon(iPhoton)%Energy=Pulse_data(iReIndex,5)
    Photon(iPhoton)%Time=Pulse_data(iReIndex,2)
    Photon(iPhoton)%History=Pulse_data(iReIndex,4)
    Photon(iPhoton)%ParticleNumber=Pulse_data(iReIndex,7)
    Photon(iPhoton)%InteractionNumber=Pulse_data(iReIndex,8)
    if ((liqDPI == .true.) .and. (Photon(iPhoton)%Plane==2)) then
      Photon(iPhoton)%Plane = 3
    endif
  endif
  if (import_pulses == .FALSE.) then

PlaneMat(Photon(iPhoton)%Plane)=Detectors(Pulse_data(iReIndex,1))%det_type
  endif
  iPhoton = iPhoton + 1
endif
enddo
endif

if (import_pulses == .TRUE.) then
  PlaneMat(1) = 1
  PlaneMat(2) = 1
  PlaneMat(3) = 4
endif

iNeutron = iNeutron - 1
iPhoton = iPhoton - 1

```

```

allocate (CorrelatedNeutrons (iNeutron), CorrelatedPhotons (iPhoton))

CorrelN_key = 1
idealNCounts = 0
COUNTN1 = 0
COUNTN2 = 0
IDEALN1 = 0
IDEALN2 = 0

do iCorrel = 1, iNeutron
Neutron Correlation
  if (Neutron(iCorrel)%Plane==1) then

    DoubleScatter=0

    iTIME = 1
    do while ((iCorrel-iTime>=1) .and. (Neutron(iCorrel-
iTime)%Time>=(Neutron(iCorrel)%Time-window_front))) !Check for double
scatters
      if (Neutron(iCorrel-iTime)%Plane==1) then
        DoubleScatter=1
      endif
      iTIME=iTime+1
    enddo

    iTIME=1
    do while ((iCorrel+iTime<=iNeutron) .and.
(Neutron(iCorrel+iTime)%Time<=(Neutron(iCorrel)%Time+window_front))) !Check
for double scatters
      if (Neutron(iCorrel+iTime)%Plane==1) then
        DoubleScatter=1
      endif
      iTIME=iTime+1
    enddo

    if (DoubleScatter==0) then
      iTIME=1
      Correlated = 1
      do while ((iCorrel+iTime<=iNeutron) .and.
(Neutron(iCorrel+iTime)%Time<=(Neutron(iCorrel)%Time+window_end)) .and.
(Correlated==1)) !Look for correlation
        if
((Neutron(iCorrel+iTime)%Time>=(Neutron(iCorrel)%Time+window_start)) .and.
(Neutron(iCorrel+iTime)%Plane==2)) then
          Temp (Correlated,1)=Neutron (iCorrel+iTime) %Time
          Temp (Correlated,2)=Neutron (iCorrel+iTime) %X
          Temp (Correlated,3)=Neutron (iCorrel+iTime) %Y
          Temp (Correlated,4)=Neutron (iCorrel+iTime) %Z
          Temp (Correlated,6)=Neutron (iCorrel+iTime) %History
          Temp (Correlated,7)=Neutron (iCorrel+iTime) %ParticleNumber
          Temp (Correlated,8)=Neutron (iCorrel+iTime) %InteractionNumber
          Temp (Correlated,9)=Neutron (iCorrel+iTime) %Energy
          Correlated = Correlated + 1
        endif
      endif
    endif
  endif
enddo

```

```

        iTime=iTime+1
    enddo

    if (Correlated == 2) then
! Correlated count found
        CorrelatedNeutrons(CorrelN_key)%Plane = Neutron(iCorrel)%Plane
        CorrelatedNeutrons(CorrelN_key)%Energy1 = Neutron(iCorrel)%Energy
        CorrelatedNeutrons(CorrelN_key)%X1 = Neutron(iCorrel)%X
        CorrelatedNeutrons(CorrelN_key)%Y1 = Neutron(iCorrel)%Y
        CorrelatedNeutrons(CorrelN_key)%Z1 = Neutron(iCorrel)%Z
        CorrelatedNeutrons(CorrelN_key)%Time1 = Temp(1,1) -
Neutron(iCorrel)%Time
        CorrelatedNeutrons(CorrelN_key)%X2 = Temp(1,2)
        CorrelatedNeutrons(CorrelN_key)%Y2 = Temp(1,3)
        CorrelatedNeutrons(CorrelN_key)%Z2 = Temp(1,4)
        CorrelatedNeutrons(CorrelN_key)%Energy2 = Temp(1,9)
        if ((Temp(1,6)==Neutron(iCorrel)%History) .and.
(Neutron(iCorrel)%ParticleNumber/= -999) .and. (Temp(1,7)/= -999) .and.
(Temp(1,7)==Neutron(iCorrel)%ParticleNumber) .and.
(Neutron(iCorrel)%InteractionNumber==1) .and. (Temp(1,8)==2)) then
            CorrelatedNeutrons(CorrelN_key)%Ideal = 1
            idealNCounts = idealNCounts + 1
            IDEALN1 = IDEALN1 + 1
        else
            CorrelatedNeutrons(CorrelN_key)%Ideal = 0
        endif
        if(Temp(1,6)==Neutron(iCorrel)%History) then
            CorrelatedNeutrons(CorrelN_key)%History =
Neutron(iCorrel)%History
        else
            CorrelatedNeutrons(CorrelN_key)%History = -999
        endif
        COUNTN1 = COUNTN1 + 1
        CorrelN_key = CorrelN_key + 1
    endif

endif

elseif (Neutron(iCorrel)%Plane==2) then

    DoubleScatter=0

    iTime = 1
    do while ((iCorrel-iTime>=1) .and. (Neutron(iCorrel-
iTime)%Time>=(Neutron(iCorrel)%Time-window_front))) !Check for double
scatters
        if (Neutron(iCorrel-iTime)%Plane==2) then
            DoubleScatter=1
        endif
        iTime=iTime+1
    enddo

    iTime=1
    do while ((iCorrel+iTime<=iNeutron) .and.
(Neutron(iCorrel+iTime)%Time<=(Neutron(iCorrel)%Time+window_front))) !Check
for double scatters
        if (Neutron(iCorrel+iTime)%Plane==2) then

```

```

        DoubleScatter=1
    endif
    iTime=iTime+1
enddo

if (DoubleScatter==0) then
    iTime=1
    Correlated = 1
    do while ((iCorrel+iTime<=iNeutron) .and.
(Neutron(iCorrel+iTime)%Time<=(Neutron(iCorrel)%Time+window_end)) .and.
(Correlated==1))          !Look for correlation
        if
((Neutron(iCorrel+iTime)%Time>=(Neutron(iCorrel)%Time+window_start)) .and.
(Neutron(iCorrel+iTime)%Plane==1)) then
            Temp(Correlated,1)=Neutron(iCorrel+iTime)%Time
            Temp(Correlated,2)=Neutron(iCorrel+iTime)%X
            Temp(Correlated,3)=Neutron(iCorrel+iTime)%Y
            Temp(Correlated,4)=Neutron(iCorrel+iTime)%Z
            Temp(Correlated,6)=Neutron(iCorrel+iTime)%History
            Temp(Correlated,7)=Neutron(iCorrel+iTime)%ParticleNumber
            Temp(Correlated,8)=Neutron(iCorrel+iTime)%InteractionNumber
            Temp(Correlated,9)=Neutron(iCorrel+iTime)%Energy
            Correlated = Correlated + 1
        endif
        iTime=iTime+1
    enddo

    if (Correlated == 2) then
! Correlated count found
        CorrelatedNeutrons(CorrelN_key)%Plane = Neutron(iCorrel)%Plane
        CorrelatedNeutrons(CorrelN_key)%Energy1 = Neutron(iCorrel)%Energy
        CorrelatedNeutrons(CorrelN_key)%X1 = Neutron(iCorrel)%X
        CorrelatedNeutrons(CorrelN_key)%Y1 = Neutron(iCorrel)%Y
        CorrelatedNeutrons(CorrelN_key)%Z1 = Neutron(iCorrel)%Z
        CorrelatedNeutrons(CorrelN_key)%Time1 = Temp(1,1) -
Neutron(iCorrel)%Time
        CorrelatedNeutrons(CorrelN_key)%X2 = Temp(1,2)
        CorrelatedNeutrons(CorrelN_key)%Y2 = Temp(1,3)
        CorrelatedNeutrons(CorrelN_key)%Z2 = Temp(1,4)
        CorrelatedNeutrons(CorrelN_key)%Energy2 = Temp(1,9)
        if ((Temp(1,6)==Neutron(iCorrel)%History) .and.
(Neutron(iCorrel)%ParticleNumber/= -999) .and. (Temp(1,7)/= -999) .and.
(Temp(1,7)==Neutron(iCorrel)%ParticleNumber) .and.
(Neutron(iCorrel)%InteractionNumber==1) .and. (Temp(1,8)==2)) then
            CorrelatedNeutrons(CorrelN_key)%Ideal = 1
            IDEALN2 = IDEALN2 + 1
            idealNCounts = idealNCounts+1
        else
            CorrelatedNeutrons(CorrelN_key)%Ideal = 0
        endif
        if (Temp(1,6)==Neutron(iCorrel)%History) then
            CorrelatedNeutrons(CorrelN_key)%History =
Neutron(iCorrel)%History
        else
            CorrelatedNeutrons(CorrelN_key)%History = -999
        endif
        COUNTN2 = COUNTN2 + 1
    endif
endif

```

```

        CorrelN_key = CorrelN_key + 1
    endif

endif

endif
enddo

CorrelP_key = 1
idealPCounts = 0
COUNT1=0
COUNT2=0
COUNT3=0
IDEAL1=0
IDEAL2=0
IDEAL3=0
!$$$$$$ CAUSE1=0
!$$$$$$ CAUSE2=0
!$$$$$$ CAUSE21=0
!$$$$$$ CAUSE22=0
!$$$$$$ CAUSE3=0
!$$$$$$ CAUSE4=0

do iCorrel = 1, iPhoton
! Photon Correlation
    if (Photon(iCorrel)%Plane==3) then

        iTime = 1
        Correlated = 1

        do while ((iCorrel-iTime>=1) .and. (Photon(iCorrel-
iTime)%Time>=(Photon(iCorrel)%Time-window_gamma)))          ! Look for
correlated count
            Temp(Correlated,1)=Photon(iCorrel-iTime)%Energy
            Temp(Correlated,2)=Photon(iCorrel-iTime)%X
            Temp(Correlated,3)=Photon(iCorrel-iTime)%Y
            Temp(Correlated,4)=Photon(iCorrel-iTime)%Z
            Temp(Correlated,5)=Photon(iCorrel-iTime)%Plane
            Temp(Correlated,6)=Photon(iCorrel-iTime)%History
            Temp(Correlated,7)=Photon(iCorrel-iTime)%ParticleNumber
            Temp(Correlated,8)=Photon(iCorrel-iTime)%InteractionNumber
            Temp(Correlated,9)=Photon(iCorrel-iTime)%Time
            Correlated = Correlated + 1
            iTime = iTime + 1
        enddo
        iTime = 1
        do while ((iCorrel+iTime<=iPhoton) .and.
(Photon(iCorrel+iTime)%Time<=(Photon(iCorrel)%Time+window_gamma)))
            Temp(Correlated,1)=Photon(iCorrel+iTime)%Energy
            Temp(Correlated,2)=Photon(iCorrel+iTime)%X
            Temp(Correlated,3)=Photon(iCorrel+iTime)%Y
            Temp(Correlated,4)=Photon(iCorrel+iTime)%Z
            Temp(Correlated,5)=Photon(iCorrel+iTime)%Plane
            Temp(Correlated,6)=Photon(iCorrel+iTime)%History
            Temp(Correlated,7)=Photon(iCorrel+iTime)%ParticleNumber
            Temp(Correlated,8)=Photon(iCorrel+iTime)%InteractionNumber

```

```

Temp (Correlated, 9)=Photon (iCorrel+iTime)%Time
Correlated = Correlated + 1
iTime = iTime + 1
enddo

if ((Correlated == 2) .and. ((Temp(1,5) == 1) .or. (Temp(1,5) == 2)))
then
! 2-plane Correlated count
found
CorrelatedPhotons (CorrelP_key)%Plane = Temp(1,5)
if (CorrelatedPhotons (CorrelP_key)%Plane == 1) then
CorrelatedPhotons (CorrelP_key)%Energy1 = Temp(1,1)
CorrelatedPhotons (CorrelP_key)%X1 = Temp(1,2)
CorrelatedPhotons (CorrelP_key)%Y1 = Temp(1,3)
CorrelatedPhotons (CorrelP_key)%Z1 = Temp(1,4)
CorrelatedPhotons (CorrelP_key)%Time1 = Temp(1,9) -
Photon (iCorrel)%Time
CorrelatedPhotons (CorrelP_key)%Energy2 = 0
CorrelatedPhotons (CorrelP_key)%X2 = 0
CorrelatedPhotons (CorrelP_key)%Y2 = 0
CorrelatedPhotons (CorrelP_key)%Z2 = 0
CorrelatedPhotons (CorrelP_key)%Time2 = 0
else
CorrelatedPhotons (CorrelP_key)%Energy2 = Temp(1,1)
CorrelatedPhotons (CorrelP_key)%X2 = Temp(1,2)
CorrelatedPhotons (CorrelP_key)%Y2 = Temp(1,3)
CorrelatedPhotons (CorrelP_key)%Z2 = Temp(1,4)
CorrelatedPhotons (CorrelP_key)%Time2 = Temp(1,9) -
Photon (iCorrel)%Time
CorrelatedPhotons (CorrelP_key)%Energy1 = 0
CorrelatedPhotons (CorrelP_key)%X1 = 0
CorrelatedPhotons (CorrelP_key)%Y1 = 0
CorrelatedPhotons (CorrelP_key)%Z1 = 0
CorrelatedPhotons (CorrelP_key)%Time1 = 0
endif
CorrelatedPhotons (CorrelP_key)%Energy3 = Photon (iCorrel)%Energy
CorrelatedPhotons (CorrelP_key)%X3 = Photon (iCorrel)%X
CorrelatedPhotons (CorrelP_key)%Y3 = Photon (iCorrel)%Y
CorrelatedPhotons (CorrelP_key)%Z3 = Photon (iCorrel)%Z
if ((Temp(1,6)==Photon (iCorrel)%History) .and.
(Photon (iCorrel)%ParticleNumber/= -999) .and. (Temp(1,7)/= -999) .and.
(Temp(1,7)==Photon (iCorrel)%ParticleNumber) .and.
(Photon (iCorrel)%InteractionNumber==2) .and. (Temp(1,8)==1)) then
CorrelatedPhotons (CorrelP_key)%Ideal = 1
idealPCounts = idealPCounts+1
else
CorrelatedPhotons (CorrelP_key)%Ideal = 0
!$$$$$$ if (Temp(1,6)/=Photon (iCorrel)%History) then
!$$$$$$ CAUSE1=CAUSE1+1
!$$$$$$ endif
!$$$$$$ if (Temp(1,7)==-999) then
!$$$$$$ CAUSE21=CAUSE21+1
!$$$$$$ endif
!$$$$$$ if (Photon (iCorrel)%ParticleNumber==-999) then
!$$$$$$ CAUSE22=CAUSE22+1
!$$$$$$ endif
!$$$$$$ if (Temp(1,7)/=Photon (iCorrel)%ParticleNumber) then
!$$$$$$ CAUSE2=CAUSE2+1

```



```

!$$$$$          endif
!$$$$$          if(Temp(1,8)/=1) then
!$$$$$            CAUSE3=CAUSE3+1
!$$$$$          endif
!$$$$$          if(Photon(iCorrel)%InteractionNumber/=2) then
!$$$$$            CAUSE4=CAUSE4+1
!$$$$$            write(*,*) Photon(iCorrel)%History
!$$$$$            write(*,*) Photon(iCorrel)%InteractionNumber
!$$$$$          endif
endif
if (Temp(1,6)==Photon(iCorrel)%History) then
  CorrelatedPhotons(CorrelP_key)%History = Photon(iCorrel)%History
else
  CorrelatedPhotons(CorrelP_key)%History = -999
endif
if (CorrelatedPhotons(CorrelP_key)%Plane == 1) then
  COUNT1=COUNT1+1
  if (CorrelatedPhotons(CorrelP_key)%Ideal == 1) then
    IDEAL1=IDEAL1+1
  endif
else
  COUNT2=COUNT2+1
  if (CorrelatedPhotons(CorrelP_key)%Ideal == 1) then
    IDEAL2=IDEAL2+1
  endif
endif
CorrelP_key = CorrelP_key + 1
endif

if ((Correlated == 3) .and. ((Temp(1,5) == 1) .and. (Temp(2,5) == 2))
.or. ((Temp(2,5) == 1) .and. (Temp(1,5) == 2))) then
Correlated count found
COUNT3=COUNT3+1
if (Temp(1,5) == 1) then
CorrelatedPhotons(CorrelP_key)%Energy1 = Temp(1,1)
CorrelatedPhotons(CorrelP_key)%X1 = Temp(1,2)
CorrelatedPhotons(CorrelP_key)%Y1 = Temp(1,3)
CorrelatedPhotons(CorrelP_key)%Z1 = Temp(1,4)
CorrelatedPhotons(CorrelP_key)%Time1 = Temp(1,9) -
Photon(iCorrel)%Time
CorrelatedPhotons(CorrelP_key)%Energy2 = Temp(2,1)
CorrelatedPhotons(CorrelP_key)%X2 = Temp(2,2)
CorrelatedPhotons(CorrelP_key)%Y2 = Temp(2,3)
CorrelatedPhotons(CorrelP_key)%Z2 = Temp(2,4)
CorrelatedPhotons(CorrelP_key)%Time2 = Temp(2,9) -
Photon(iCorrel)%Time
CorrelatedPhotons(CorrelP_key)%Energy3 = Photon(iCorrel)%Energy
CorrelatedPhotons(CorrelP_key)%X3 = Photon(iCorrel)%X
CorrelatedPhotons(CorrelP_key)%Y3 = Photon(iCorrel)%Y
CorrelatedPhotons(CorrelP_key)%Z3 = Photon(iCorrel)%Z
if ((Temp(1,6)==Photon(iCorrel)%History) .and.
(Temp(2,6)==Photon(iCorrel)%History) .and. (Photon(iCorrel)%ParticleNumber/=
-999) .and. (Temp(1,7)/= -999) .and. (Temp(2,7)/= -999) .and.
(Temp(1,7)==Photon(iCorrel)%ParticleNumber) .and.
(Temp(2,7)==Photon(iCorrel)%ParticleNumber) .and.
! 3-plane

```

```

(Photon(iCorrel)%InteractionNumber==3) .and. (Temp(1,8)==1) .and.
(Temp(2,8)==2) then
    CorrelatedPhotons(CorrelP_key)%Ideal = 1
    idealPCounts = idealPCounts+1
    IDEAL3=IDEAL3+1
else
    CorrelatedPhotons(CorrelP_key)%Ideal = 0
endif
else
    CorrelatedPhotons(CorrelP_key)%Energy1 = Temp(2,1)
    CorrelatedPhotons(CorrelP_key)%X1 = Temp(2,2)
    CorrelatedPhotons(CorrelP_key)%Y1 = Temp(2,3)
    CorrelatedPhotons(CorrelP_key)%Z1 = Temp(2,4)
    CorrelatedPhotons(CorrelP_key)%Time1 = Temp(2,9) -
Photon(iCorrel)%Time
    CorrelatedPhotons(CorrelP_key)%Energy2 = Temp(1,1)
    CorrelatedPhotons(CorrelP_key)%X2 = Temp(1,2)
    CorrelatedPhotons(CorrelP_key)%Y2 = Temp(1,3)
    CorrelatedPhotons(CorrelP_key)%Z2 = Temp(1,4)
    CorrelatedPhotons(CorrelP_key)%Time2 = Temp(1,9) -
Photon(iCorrel)%Time
    CorrelatedPhotons(CorrelP_key)%Energy3 = Photon(iCorrel)%Energy
    CorrelatedPhotons(CorrelP_key)%X3 = Photon(iCorrel)%X
    CorrelatedPhotons(CorrelP_key)%Y3 = Photon(iCorrel)%Y
    CorrelatedPhotons(CorrelP_key)%Z3 = Photon(iCorrel)%Z
    if ((Temp(1,6)==Photon(iCorrel)%History) .and.
(Temp(2,6)==Photon(iCorrel)%History) .and.
(Temp(1,7)==Photon(iCorrel)%ParticleNumber) .and.
(Temp(2,7)==Photon(iCorrel)%ParticleNumber) .and.
(Photon(iCorrel)%InteractionNumber==3) .and. (Temp(1,8)==2) .and.
(Temp(2,8)==1)) then
        CorrelatedPhotons(CorrelP_key)%Ideal = 1
        idealPCounts = idealPCounts+1
        IDEAL3=IDEAL3+1
    else
        CorrelatedPhotons(CorrelP_key)%Ideal = 0
    endif
endif
endif
    CorrelatedPhotons(CorrelP_key)%Plane = 3
    if ((Temp(1,6)==Photon(iCorrel)%History) .and.
(Temp(2,6)==Photon(iCorrel)%History)) then
        CorrelatedPhotons(CorrelP_key)%History = Photon(iCorrel)%History
    else
        CorrelatedPhotons(CorrelP_key)%History = -999
    endif
    CorrelP_key = CorrelP_key + 1
endif

endif
enddo

CorrelN_key = CorrelN_key - 1
CorrelP_key = CorrelP_key - 1

deallocate (Neutron, Photon, temp)

open(74, file=(trim(output_file)//'_counts.c'), status='replace')

```

```

write (74,*) 'TotalType1-2Counts ',COUNTN1
write (74,*) 'TotalType2-1Counts ',COUNTN2
write (74,*) 'TotalNeutronCounts ',CorrelN_key
write (74,*) 'TotalType1-3Counts ',COUNT1
write (74,*) 'TotalType2-3Counts ',COUNT2
write (74,*) 'TotalType1-2-3Counts',COUNT3
write (74,*) 'TotalPhotonCounts ',CorrelP_key
write (74,*) 'TrueType1-2Counts ',IDEALN1
write (74,*) 'TrueType2-1Counts ',IDEALN2
write (74,*) 'TrueNeutronCounts ',idealNCounts
write (74,*) 'TrueType1-3Counts ',IDEAL1
write (74,*) 'TrueType2-3Counts ',IDEAL2
write (74,*) 'TrueType1-2-3Counts ',IDEAL3
write (74,*) 'TruePhotonCounts ',idealPCounts
close(74)

if (segment_number == 1) then

open(85,file=(trim(output_file)//'_Correlated_pulses_n.o'),status='replace')
else

open(85,file=(trim(output_file)//'_Correlated_pulses_n.o'),status='old',access='append')
endif
!NOTE:: Correlated_pulses_n has the form [Plane, Energy1, X1, Y1, Z1, Time, X2, Y2, Z2, Ideal]
333 Format (I3,A1,F20.6,A1,I3,A1,I3,A1,I3,A1,F25.8,A1,I3,A1,I3,A1,I3,A1,I3)
do iOutput=1,CorrelN_key
write(85,333)
CorrelatedNeutrons(iOutput)%Plane,', ',CorrelatedNeutrons(iOutput)%Energy1,', ',
,CorrelatedNeutrons(iOutput)%X1,', ',CorrelatedNeutrons(iOutput)%Y1,', ',CorrelatedNeutrons(iOutput)%Z1,', ',CorrelatedNeutrons(iOutput)%Time1,', ',CorrelatedNeutrons(iOutput)%X2,', ',CorrelatedNeutrons(iOutput)%Y2,', ',CorrelatedNeutrons(iOutput)%Z2,', ',CorrelatedNeutrons(iOutput)%Ideal
enddo
close(85)

if (segment_number == 1) then

open(86,file=(trim(output_file)//'_Correlated_pulses_p.o'),status='replace')
else

open(86,file=(trim(output_file)//'_Correlated_pulses_p.o'),status='old',access='append')
endif
!NOTE:: Correlated_pulses_p has the form [Plane, Energy1, X1, Y1, Z1, Energy2, X2, Y2, Z2, Energy3, X3, Y3, Z3, Ideal]
334 Format
(I3,A1,F20.6,A1,I3,A1,I3,A1,I3,A1,F20.6,A1,I3,A1,I3,A1,I3,A1,F20.6,A1,I3,A1,I3,A1,I3,A1,I3)
do iOutput=1,CorrelP_key
write(86,334)
CorrelatedPhotons(iOutput)%Plane,', ',CorrelatedPhotons(iOutput)%Energy1,', ',CorrelatedPhotons(iOutput)%X1,', ',CorrelatedPhotons(iOutput)%Y1,', ',CorrelatedPhotons(iOutput)%Z1,', ',CorrelatedPhotons(iOutput)%Energy2,', ',CorrelatedPhotons(iOutput)%X2,', ',CorrelatedPhotons(iOutput)%Y2,', ',CorrelatedPhotons(iOutput)%Z2,', ',CorrelatedPhotons(iOutput)%Energy3,', ',CorrelatedPhotons(iOutput)%

```

```

X3, ',', CorrelatedPhotons(iOutput)%Y3, ',', CorrelatedPhotons(iOutput)%Z3, ',', CorrelatedPhotons(iOutput)%Ideal
enddo
close(86)

!Processing of data before heading to imaging

allocate(ReconstructedEnergyN(CorrelN_key), ReconstructedEnergyP(CorrelP_key),
angleN(CorrelN_key), angleP(CorrelP_key), SigmaN(CorrelN_key), SigmaP(CorrelP_key),
TypeN(CorrelN_key), TypeP(CorrelP_key))
allocate(axisN(CorrelN_key,3), axisP(CorrelP_key,3), originN(CorrelN_key,3), originP(CorrelP_key,3))

do iBackPro=1, CorrelN_key
  if (CorrelatedNeutrons(iBackPro)%Plane == 1) then
    X1 = xVox(1,1) + (CorrelatedNeutrons(iBackPro)%X1 - 0.5) * xVox(1,2)
    Y1 = yVox(1,1) + (CorrelatedNeutrons(iBackPro)%Y1 - 0.5) * yVox(1,2)
    Z1 = zVox(1,1) + (CorrelatedNeutrons(iBackPro)%Z1 - 0.5) * zVox(1,2)
    X2 = xVox(2,1) + (CorrelatedNeutrons(iBackPro)%X2 - 0.5) * xVox(2,2)
    Y2 = yVox(2,1) + (CorrelatedNeutrons(iBackPro)%Y2 - 0.5) * yVox(2,2)
    Z2 = zVox(2,1) + (CorrelatedNeutrons(iBackPro)%Z2 - 0.5) * zVox(2,2)
    TypeN(iBackPro)=1
  elseif (CorrelatedNeutrons(iBackPro)%Plane == 2) then
    X1 = xVox(2,1) + (CorrelatedNeutrons(iBackPro)%X1 - 0.5) * xVox(2,2)
    Y1 = yVox(2,1) + (CorrelatedNeutrons(iBackPro)%Y1 - 0.5) * yVox(2,2)
    Z1 = zVox(2,1) + (CorrelatedNeutrons(iBackPro)%Z1 - 0.5) * zVox(2,2)
    X2 = xVox(1,1) + (CorrelatedNeutrons(iBackPro)%X2 - 0.5) * xVox(1,2)
    Y2 = yVox(1,1) + (CorrelatedNeutrons(iBackPro)%Y2 - 0.5) * yVox(1,2)
    Z2 = zVox(1,1) + (CorrelatedNeutrons(iBackPro)%Z2 - 0.5) * zVox(1,2)
    TypeN(iBackPro)=2
  endif
  axisN(iBackPro,1)=X1-X2
  axisN(iBackPro,2)=Y1-Y2
  axisN(iBackPro,3)=Z1-Z2
  originN(iBackPro,1)=X1
  originN(iBackPro,2)=Y1
  originN(iBackPro,3)=Z1
  CorrelatedNeutrons(iBackPro)%Energy3=CorrelatedNeutrons(iBackPro)%Energy1
  if (use_birksH==.TRUE.) then
    CorrelatedNeutrons(iBackPro)%Energy1 =
ReverseBirks(CorrelatedNeutrons(iBackPro)%Energy1,1, PlaneMat(CorrelatedNeutrons(iBackPro)%Plane))
  else
    do iEnergy=1, neutron_calibration_regions
      if (neutron_region_type(iEnergy) == 1) then
        A=Neutron_calibration(iEnergy,5)
        B=Neutron_calibration(iEnergy,6)
        C=Neutron_calibration(iEnergy,7)

low_limit=A*Neutron_Calibration(iEnergy,1)**2+B*Neutron_Calibration(iEnergy,1)+C

high_limit=A*Neutron_Calibration(iEnergy,2)**2+B*Neutron_Calibration(iEnergy,2)+C

        if (CorrelatedNeutrons(iBackPro)%Energy1>=low_limit .and.
CorrelatedNeutrons(iBackPro)%Energy1<high_limit) then

```

```

CorrelatedNeutrons (iBackPro) %Energy1=(sqrt (( B/A) **2-4* (C-
CorrelatedNeutrons (iBackPro) %Energy1) /A) - (B/A) ) /2
endif
elseif (neutron_region_type(iEnergy) == 2) then
A=Neutron_calibration(iEnergy,6)
B=Neutron_calibration(iEnergy,7)

low_limit=(A*Neutron_Calibration(iEnergy,1)**2)/(Neutron_Calibration(iEnergy,
1)+B)

high_limit=(A*Neutron_Calibration(iEnergy,2)**2)/(Neutron_Calibration(iEnergy
,2)+B)

if (CorrelatedNeutrons (iBackPro) %Energy1>=low_limit .and.
CorrelatedNeutrons (iBackPro) %Energy1<high_limit) then

CorrelatedNeutrons (iBackPro) %Energy1=(CorrelatedNeutrons (iBackPro) %Energy1+sq
rt (CorrelatedNeutrons (iBackPro) %Energy1) *sqrt (4*A*B+CorrelatedNeutrons (iBackP
ro) %Energy1) ) / (2*A)
endif
elseif (neutron_region_type(iEnergy) == 3) then
A=Neutron_calibration(iEnergy,3)
B=Neutron_calibration(iEnergy,4)
C=Neutron_calibration(iEnergy,5)
D=Neutron_calibration(iEnergy,6)
E=Neutron_calibration(iEnergy,7)
low_limit=A*(B*Neutron_Calibration(iEnergy,1)-C*(1-
exp(D*Neutron_Calibration(iEnergy,1)**E)))
high_limit=A*(B*Neutron_Calibration(iEnergy,2)-C*(1-
exp(D*Neutron_Calibration(iEnergy,2)**E)))
if (CorrelatedNeutrons (iBackPro) %Energy1>=low_limit .and.
CorrelatedNeutrons (iBackPro) %Energy1<high_limit) then
!
CorrelatedNeutrons (iBackPro) %Energy1=(100*(40861500*WEW_A(-(39022247*exp(-
(29686*y)/81723-
39022247/40861500))/40861500,EN)+14843000*y+39022247))/1213014489

CorrelatedNeutrons (iBackPro) %Energy1=(A*C+CorrelatedNeutrons (iBackPro) %Energy
1) / (A*B) -
(WAPR((C*D*exp((D*(A*C+CorrelatedNeutrons (iBackPro) %Energy1) / (A*B)))/B,0,NER
ROR,0,0))/D
endif
endif
enddo
endif
ETOF =
JtoMeV*(neutron_mass/2)*(((0.01*axisN(iBackPro,1))**2+(0.01*axisN(iBackPro,2)
)**2+(0.01*axisN(iBackPro,3))**2)/(1E-
9*CorrelatedNeutrons (iBackPro) %Time1)**2)

angleN(iBackPro)=180*atan(sqrt(CorrelatedNeutrons (iBackPro) %Energy1/ETOF))/pi
ReconstructedEnergyN(iBackPro)=CorrelatedNeutrons (iBackPro) %Energy1+ETOF
R2= sqrt( (axisN(iBackPro,1))**2 + (axisN(iBackPro,2))**2 +
(axisN(iBackPro,3))**2 )
theta = acos( abs(axisN(iBackPro,3)) / R2)
phi = atan( abs( (axisN(iBackPro,2))/(axisN(iBackPro,1)) ) )
errorInScatter = 180/pi*sqrt(
(xVox(CorrelatedNeutrons (iBackPro) %Plane,2)*cos(phi))**2*((1/R2)*cos(theta))*

```

```

*2 +
(yVox(CorrelatedNeutrons(iBackPro)%Plane,2)*sin(phi))**2*((1/r2)*cos(theta))*
*2 )
errorInAbsorbtion = 180/pi*sqrt( (1/R2**2)*((xVox(3-
CorrelatedNeutrons(iBackPro)%Plane,2)*cos(theta)*cos(phi))**2+(yVox(3-
CorrelatedNeutrons(iBackPro)%Plane,2)*cos(theta)*sin(phi))**2+ (zVox(3-
CorrelatedNeutrons(iBackPro)%Plane,2)*sin(theta))**2) )
angleUncertaintyGeometry = sqrt( errorInScatter**2+errorInAbsorbtion**2)
angleUncertaintyEnergy=sqrt(1.22*(1-
CorrelatedNeutrons(iBackPro)%Time1**2/(CorrelatedNeutrons(iBackPro)%Time1+Org
anic_Liq_tme)**2))*acos(sqrt(ETOF/(ETOF+CorrelatedNeutrons(iBackPro)%Energy1)
))*180/pi;
SigmaN(iBackPro) = sqrt(angleUncertaintyGeometry**2+
angleUncertaintyEnergy**2)
enddo

do iBackPro=1,CorrelP_key
X1 = xVox(1,1) + (CorrelatedPhotons(iBackPro)%X1 - 0.5) * xVox(1,2)
Y1 = yVox(1,1) + (CorrelatedPhotons(iBackPro)%Y1 - 0.5) * yVox(1,2)
Z1 = zVox(1,1) + (CorrelatedPhotons(iBackPro)%Z1 - 0.5) * zVox(1,2)
X2 = xVox(2,1) + (CorrelatedPhotons(iBackPro)%X2 - 0.5) * xVox(2,2)
Y2 = yVox(2,1) + (CorrelatedPhotons(iBackPro)%Y2 - 0.5) * yVox(2,2)
Z2 = zVox(2,1) + (CorrelatedPhotons(iBackPro)%Z2 - 0.5) * zVox(2,2)
X3 = xVox(3,1) + (CorrelatedPhotons(iBackPro)%X3 - 0.5) * xVox(3,2)
Y3 = yVox(3,1) + (CorrelatedPhotons(iBackPro)%Y3 - 0.5) * yVox(3,2)
Z3 = zVox(3,1) + (CorrelatedPhotons(iBackPro)%Z3 - 0.5) * zVox(3,2)
if (CorrelatedPhotons(iBackPro)%Plane == 1) then
axisP(iBackPro,1)=X1-X3
axisP(iBackPro,2)=Y1-Y3
axisP(iBackPro,3)=Z1-Z3
originP(iBackPro,1)=X1
originP(iBackPro,2)=Y1
originP(iBackPro,3)=Z1
E1=CorrelatedPhotons(iBackPro)%Energy1
E2=CorrelatedPhotons(iBackPro)%Energy3
TypeP(iBackPro)=1
elseif (CorrelatedPhotons(iBackPro)%Plane == 2) then
axisP(iBackPro,1)=X2-X3
axisP(iBackPro,2)=Y2-Y3
axisP(iBackPro,3)=Z2-Z3
originP(iBackPro,1)=X2
originP(iBackPro,2)=Y2
originP(iBackPro,3)=Z2
E1=CorrelatedPhotons(iBackPro)%Energy2
E2=CorrelatedPhotons(iBackPro)%Energy3
TypeP(iBackPro)=2
elseif (CorrelatedPhotons(iBackPro)%Plane == 3) then
axisP(iBackPro,1)=X1-X2
axisP(iBackPro,2)=Y1-Y2
axisP(iBackPro,3)=Z1-Z2
originP(iBackPro,1)=X1
originP(iBackPro,2)=Y1
originP(iBackPro,3)=Z1
secaxis(1)=X3-X2
secaxis(2)=Y3-Y2
secaxis(3)=Z3-Z2

```

```

        costeta2=DOT_PRODUCT(-axisP(iBackPro,:),secaxis)/sqrt(DOT_PRODUCT(-
axisP(iBackPro,:),-axisP(iBackPro,:))*DOT_PRODUCT(secaxis,secaxis))
        if (costeta2/=1) then
            E1=CorrelatedPhotons(iBackPro)%Energy1

E2=(sqrt(CorrelatedPhotons(iBackPro)%Energy2**2+(4*0.511*CorrelatedPhotons(iB
ackPro)%Energy2)/(1-costeta2))-CorrelatedPhotons(iBackPro)%Energy2)/2
            else
                E1=-999
                E2=-999
                ReconstructedEnergyP(iBackPro)=-999
                angleP(iBackPro)=-999
            endif
            TypeP(iBackPro)=3
        endif

        if (E2/=-999) then
            ReconstructedEnergyP(iBackPro)=E1+E2
            if (liqDPI==.TRUE.) then
                E2 = liqDPInerg - E1
            endif
            if (abs(1-((0.511*E1)/((E1+E2)*E2)))<=1) then
                angleP(iBackPro)=180*acos(1-(0.511*E1)/((E1+E2)*(E2)))/pi
                R2= sqrt( (axisP(iBackPro,1))**2 + (axisP(iBackPro,2))**2 +
(axisP(iBackPro,3))**2 )
                theta = acos( abs(axisP(iBackPro,3)) / R2)
                phi = atan( abs( (axisP(iBackPro,2))/(axisP(iBackPro,1)) ) )
                if (CorrelatedPhotons(iBackPro)%Plane == 3) then
                    errorInScatter = 180/pi*sqrt(
(xVox(1,2)*cos(phi))**2*((1/R2)*cos(theta))**2 +
(yVox(1,2)*sin(phi))**2*((1/r2)*cos(theta))**2 )
                    errorInAbsorbtion = 180/pi*sqrt(
(1/R2**2)*((xVox(2,2)*cos(theta)*cos(phi))**2+(yVox(2,2)*cos(theta)*sin(phi))
**2+ (zVox(2,2)*sin(theta))**2) )
                else
                    errorInScatter = 180/pi*sqrt(
(xVox(CorrelatedPhotons(iBackPro)%Plane,2)*cos(phi))**2*((1/R2)*cos(theta))**
2 +
(yVox(CorrelatedPhotons(iBackPro)%Plane,2)*sin(phi))**2*((1/r2)*cos(theta))**
2 )
                    errorInAbsorbtion = 180/pi*sqrt(
(1/R2**2)*((xVox(3,2)*cos(theta)*cos(phi))**2+(yVox(3,2)*cos(theta)*sin(phi))
**2+ (zVox(3,2)*sin(theta))**2) )
                endif
                angleUncertaintyGeometry = sqrt(
errorInScatter**2+errorInAbsorbtion**2)

energyRes1=((RES_2(2)*sqrt(1000*Energy))+RES_2(3)+(1000*Energy*RES_2(1)))/(1
00*1000)
                energyRes2=((811*((1000*E2)**(-1.06)))-
(5*((1000*E2)/4000)**(1.8))+6.2)/100*(E2)
                angleUncertaintyEnergy = 180/pi*sqrt(((.511*energyRes2)/((E1 +
E2)**4 * (1-.261121 /((E1+E2)**2)))+(energyRes1*.261121
/((E1+E2)**2*(1.022*E1+1.022*E2-.261121))))
                !angleUncertaintyEnergy = sqrt((E1**2*energyRes2**2*(-29.2781*E1-
58.5563*E2)**2)/(E2**4*(E1+E2)**4*(1-(1-

```

```

(0.511*E1)/(E2*(E1+E2))**2))+ (32400*energyRes1**2*((0.511*E1)/(E2*(E1+E2))**2
)-0.511/(E2*(E1+E2))**2)/(Pi**2*(1-(1-(0.511*E1)/(E2*(E1+E2))**2)))
        angleUncertaintyEnergy = 0
        SigmaP(iBackPro) = sqrt(angleUncertaintyGeometry**2+
angleUncertaintyEnergy**2)
    else
        angleP(iBackPro)=-999
        SigmaP(iBackPro)=-999
    endif
endif
enddo

if (segment_number == 1) then

open(83,file=(trim(output_file)//'_correlatedneutrons.phd'),status='replace')
else

open(83,file=(trim(output_file)//'_correlatedneutrons.phd'),status='old',acce
ss='append')
endif
do iBackPro=1,CorrelN_key
write
(83,*)ReconstructedEnergyN(iBackPro),CorrelatedNeutrons(iBackPro)%ideal,Corre
latedNeutrons(iBackPro)%Plane
enddo
close(83)

if (segment_number == 1) then

open(84,file=(trim(output_file)//'_correlatedphotons.phd'),status='replace')
else

open(84,file=(trim(output_file)//'_correlatedphotons.phd'),status='old',acces
s='append')
endif
do iBackPro=1,CorrelP_key
write
(84,*)ReconstructedEnergyP(iBackPro),CorrelatedPhotons(iBackPro)%ideal,Correl
atedPhotons(iBackPro)%Plane
enddo
close(84)

! open(83,file=(trim(output_file)//'_SigmaN_debug.o'),status='replace')
! do iBackPro=1,CorrelN_key
! write (83,*)SigmaN(iBackPro)
! enddo
! close(83)

! open(84,file=(trim(output_file)//'_SigmaP_debug.o'),status='replace')
! do iBackPro=1,CorrelP_key
! write (84,*)SigmaP(iBackPro)
! enddo
! close(84)

if (segment_number == 1) then

open(85,file=(trim(output_file)//'_Correlated_events_n.o'),status='replace')

```



```

else

open(85,file=(trim(output_file)//'_Correlated_events_n.o'),status='old',access='append')
endif
335 Format
(F20.6,A1,F20.6,A1,I3,A1,F20.6,A1,I3,A1,I3,A1,I3,A1,F20.6,A1,I3,A1,I3,A1,I3,A1,F20.6,A1,I3,A1,I20)
do iOutput=1,CorrelN_key
write(85,335)
ReconstructedEnergyN(iOutput),',',angleN(iOutput),',',CorrelatedNeutrons(iOutput)%Plane,',',CorrelatedNeutrons(iOutput)%Energy3,',',CorrelatedNeutrons(iOutput)%X1,',',CorrelatedNeutrons(iOutput)%Y1,',',CorrelatedNeutrons(iOutput)%Z1,',',CorrelatedNeutrons(iOutput)%Energy2,',',CorrelatedNeutrons(iOutput)%X2,',',CorrelatedNeutrons(iOutput)%Y2,',',CorrelatedNeutrons(iOutput)%Z2,',',CorrelatedNeutrons(iOutput)%Time1,',',CorrelatedNeutrons(iOutput)%Ideal,',',CorrelatedNeutrons(iOutput)%History
enddo
close(85)
if (segment_number == 1) then

open(86,file=(trim(output_file)//'_Correlated_events_p.o'),status='replace')
else

open(86,file=(trim(output_file)//'_Correlated_events_p.o'),status='old',access='append')
endif
336 Format
(F20.6,A1,F20.6,A1,I3,A1,F20.6,A1,I3,A1,I3,A1,I3,A1,F20.6,A1,F20.6,A1,I3,A1,I3,A1,I3,A1,F20.6,A1,I3,A1,I20)
do iOutput=1,CorrelP_key
write(86,336)
ReconstructedEnergyP(iOutput),',',angleP(iOutput),',',CorrelatedPhotons(iOutput)%Plane,',',CorrelatedPhotons(iOutput)%Energy1,',',CorrelatedPhotons(iOutput)%X1,',',CorrelatedPhotons(iOutput)%Y1,',',CorrelatedPhotons(iOutput)%Z1,',',CorrelatedPhotons(iOutput)%Time1,',',CorrelatedPhotons(iOutput)%Energy2,',',CorrelatedPhotons(iOutput)%X2,',',CorrelatedPhotons(iOutput)%Y2,',',CorrelatedPhotons(iOutput)%Z2,',',CorrelatedPhotons(iOutput)%Time2,',',CorrelatedPhotons(iOutput)%Energy3,',',CorrelatedPhotons(iOutput)%X3,',',CorrelatedPhotons(iOutput)%Y3,',',CorrelatedPhotons(iOutput)%Z3,',',CorrelatedPhotons(iOutput)%Ideal,',',CorrelatedPhotons(iOutput)%History
enddo
close(86)

! Call the MLEM_Input subroutine
if (mlem_input_data==.TRUE.) then
call MLEM_input
endif

! Call the Backprojection subroutine
if (backprojection==.TRUE.) then
call backproject
endif

deallocate(CorrelatedNeutrons,CorrelatedPhotons)

```

```
end Subroutine Imaging_correlation
```

```
Subroutine MLEM_input
```

```
!
```

```
! This subroutine outputs MLEM algorithm input obtained from the correlation  
! of particles.
```

```
!
```

```
use parameters_m
```

```
use Imaging_system_m
```

```
use Main_m
```

```
integer, allocatable, dimension(:, :, :)::MLEMN1, MLEMN2, MLEMP
```

```
integer, allocatable, dimension(:, :, :, :, :, :)::MLEMNA, MLEMPA, PAIRNSAE, PAIRPSAE
```

```
integer, allocatable, dimension(:, :, :, :, :, :)::MLEMPSAE, MLEMNSAE
```

```
integer::iNeutron, iPhoton
```

```
integer::iX, iY, iZ
```

```
integer::iPlane, iX1, iY1, iZ1, iX2, iY2, iZ2
```

```
integer::iEnergy, iAngle
```

```
integer::XP1MAX, YP1MAX, ZP1MAX, XPMAX, YPMAX, ZPMAX
```

```
XP1MAX=MAX(ceiling(real(anint(10000*(xVox(1,3)-  
xVox(1,1))))/real(anint(10000*xVox(1,2)))) , ceiling(real(anint(10000*(xVox(2,3)  
)-xVox(2,1))))/real(anint(10000*xVox(2,2))))
```

```
YP1MAX=MAX(ceiling(real(anint(10000*(yVox(1,3)-  
yVox(1,1))))/real(anint(10000*yVox(1,2)))) , ceiling(real(anint(10000*(yVox(2,3)  
)-yVox(2,1))))/real(anint(10000*yVox(2,2))))
```

```
ZP1MAX=MAX(ceiling(real(anint(10000*(zVox(1,3)-  
zVox(1,1))))/real(anint(10000*zVox(1,2)))) , ceiling(real(anint(10000*(zVox(2,3)  
)-zVox(2,1))))/real(anint(10000*zVox(2,2))))
```

```
XPMAX=MAX((ceiling(real(anint(10000*(xVox(1,3)-  
xVox(1,1))))/real(anint(10000*xVox(1,2))))-  
1)+(ceiling(real(anint(10000*(xVox(2,3)-  
xVox(2,1))))/real(anint(10000*xVox(2,2))))-  
1)+1, (ceiling(real(anint(10000*(xVox(1,3)-  
xVox(1,1))))/real(anint(10000*xVox(1,2))))-  
1)+(ceiling(real(anint(10000*(xVox(3,3)-  
xVox(3,1))))/real(anint(10000*xVox(3,2))))-  
1)+1, (ceiling(real(anint(10000*(xVox(2,3)-  
xVox(2,1))))/real(anint(10000*xVox(2,2))))-  
1)+(ceiling(real(anint(10000*(xVox(3,3)-  
xVox(3,1))))/real(anint(10000*xVox(3,2))))-1)+1)
```

```
YPMAX=MAX((ceiling(real(anint(10000*(yVox(1,3)-  
yVox(1,1))))/real(anint(10000*yVox(1,2))))-  
1)+(ceiling(real(anint(10000*(yVox(2,3)-  
yVox(2,1))))/real(anint(10000*yVox(2,2))))-  
1)+1, (ceiling(real(anint(10000*(yVox(1,3)-  
yVox(1,1))))/real(anint(10000*yVox(1,2))))-  
1)+(ceiling(real(anint(10000*(yVox(3,3)-  
yVox(3,1))))/real(anint(10000*yVox(3,2))))-  
1)+1, (ceiling(real(anint(10000*(yVox(2,3)-
```

```

yVox(2,1))) /real (anint (10000*yVox(2,2))) -
1)+(ceiling (real (anint (10000*(yVox(3,3)-
yVox(3,1)))) /real (anint (10000*yVox(3,2))) -1)+1)
ZPMAX=MAX((ceiling (real (anint (10000*(zVox(1,3)-
zVox(1,1)))) /real (anint (10000*zVox(1,2))) -
1)+(ceiling (real (anint (10000*(zVox(2,3)-
zVox(2,1)))) /real (anint (10000*zVox(2,2))) -
1)+1, (ceiling (real (anint (10000*(zVox(1,3)-
zVox(1,1)))) /real (anint (10000*zVox(1,2))) -
1)+(ceiling (real (anint (10000*(zVox(3,3)-
zVox(3,1)))) /real (anint (10000*zVox(3,2))) -
1)+1, (ceiling (real (anint (10000*(zVox(2,3)-
zVox(2,1)))) /real (anint (10000*zVox(2,2))) -
1)+(ceiling (real (anint (10000*(zVox(3,3)-
zVox(3,1)))) /real (anint (10000*zVox(3,2))) -1)+1)

if (segment_number == 1) then
    allocate (MLEMN1 (ceiling (real (anint (10000*(xVox(1,3)-
xVox(1,1)))) /real (anint (10000*xVox(1,2))), ceiling (real (anint (10000*(yVox(1,3)
)-
yVox(1,1)))) /real (anint (10000*yVox(1,2))), ceiling (real (anint (10000*(zVox(1,3)
)-zVox(1,1)))) /real (anint (10000*zVox(1,2)))))
    allocate (MLEMN2 (ceiling (real (anint (10000*(xVox(2,3)-
xVox(2,1)))) /real (anint (10000*xVox(2,2))), ceiling (real (anint (10000*(yVox(2,3)
)-
yVox(2,1)))) /real (anint (10000*yVox(2,2))), ceiling (real (anint (10000*(zVox(2,3)
)-zVox(2,1)))) /real (anint (10000*zVox(2,2)))))
    allocate (MLEMP (ceiling (real (anint (10000*(xVox(3,3)-
xVox(3,1)))) /real (anint (10000*xVox(3,2))), ceiling (real (anint (10000*(yVox(3,3)
)-
yVox(3,1)))) /real (anint (10000*yVox(3,2))), ceiling (real (anint (10000*(zVox(3,3)
)-zVox(3,1)))) /real (anint (10000*zVox(3,2)))))

    allocate (MLEMNA (2, ceiling (real (anint (10000*(xVox(1,3)-
xVox(1,1)))) /real (anint (10000*xVox(1,2))), ceiling (real (anint (10000*(yVox(1,3)
)-
yVox(1,1)))) /real (anint (10000*yVox(1,2))), ceiling (real (anint (10000*(zVox(1,3)
)-
zVox(1,1)))) /real (anint (10000*zVox(1,2))), ceiling (real (anint (10000*(xVox(2,3)
)-
xVox(2,1)))) /real (anint (10000*xVox(2,2))), ceiling (real (anint (10000*(yVox(2,3)
)-
yVox(2,1)))) /real (anint (10000*yVox(2,2))), ceiling (real (anint (10000*(zVox(2,3)
)-zVox(2,1)))) /real (anint (10000*zVox(2,2)))))
    allocate (MLEMPA (2, XP1MAX, YP1MAX, ZP1MAX, ceiling (real (anint (10000*(xVox(
3,3)-
xVox(3,1)))) /real (anint (10000*xVox(3,2))), ceiling (real (anint (10000*(yVox(3,3)
)-
yVox(3,1)))) /real (anint (10000*yVox(3,2))), ceiling (real (anint (10000*(zVox(3,3)
)-zVox(3,1)))) /real (anint (10000*zVox(3,2)))))

    allocate (PAIRNSAE (2, ceiling ((n_emax-
n_emin)/n_ebin), ceiling (90/mlem_angle_bin), ceiling (real (anint (10000*(xVox(1,3)
)-
xVox(1,1)))) /real (anint (10000*xVox(1,2))), ceiling (real (anint (10000*(zVox(1,3)
)-
zVox(1,1)))) /real (anint (10000*zVox(1,2))), ceiling (real (anint (10000*(xVox(2,3)

```

```

)-
xVox(2,1))) /real (anint (10000*xVox(2,2))) , ceiling (real (anint (10000*(zVox(2,3)
)-zVox(2,1))) /real (anint (10000*zVox(2,2))))))
allocate (PAIRPSAE (2, ceiling ((p_emax-
p_emin)/p_ebin) , ceiling (180/mlem_angle_bin) , XP1MAX, ZP1MAX, ceiling (real (anint (
10000*(xVox(3,3)-
xVox(3,1))) /real (anint (10000*xVox(3,2))) , ceiling (real (anint (10000*(zVox(3,3)
)-zVox(3,1))) /real (anint (10000*zVox(3,2))))))

allocate (MLEMNSAE (2, ceiling ((n_emax-
n_emin)/n_ebin) , ceiling (90/mlem_angle_bin) , (ceiling (real (anint (10000*(xVox(1,
3)-xVox(1,1))) /real (anint (10000*xVox(1,2))) -
1)+(ceiling (real (anint (10000*(xVox(2,3)-
xVox(2,1))) /real (anint (10000*xVox(2,2))) -
1)+1, (ceiling (real (anint (10000*(yVox(1,3)-
yVox(1,1))) /real (anint (10000*yVox(1,2))) -
1)+(ceiling (real (anint (10000*(yVox(2,3)-
yVox(2,1))) /real (anint (10000*yVox(2,2))) -
1)+1, (ceiling (real (anint (10000*(zVox(1,3)-
zVox(1,1))) /real (anint (10000*zVox(1,2))) -
1)+(ceiling (real (anint (10000*(zVox(2,3)-
zVox(2,1))) /real (anint (10000*zVox(2,2))) -1)+1))
allocate (MLEMPSAE (3, ceiling ((p_emax-
p_emin)/p_ebin) , ceiling (180/mlem_angle_bin) , XPMAX, YPMAX, ZPMAX))
endif

MLEMN1 (:, :, :) = 0
MLEMN2 (:, :, :) = 0
MLEMP (:, :, :) = 0

MLEMNA (:, :, :, :, :, :, :) = 0
MLEMPA (:, :, :, :, :, :, :, :) = 0

PAIRNSAE (:, :, :, :, :, :, :, :) = 0
PAIRPSAE (:, :, :, :, :, :, :, :) = 0

MLEMNSAE (:, :, :, :, :, :, :, :) = 0
MLEMPSAE (:, :, :, :, :, :, :, :, :) = 0

do iNeutron = 1, CorrelN_key
  if (CorrelatedNeutrons(iNeutron)%Plane==1) then

MLEMN2 (CorrelatedNeutrons (iNeutron) %X2, CorrelatedNeutrons (iNeutron) %Y2, Correl
atedNeutrons (iNeutron) %Z2) = MLEMN2 (CorrelatedNeutrons (iNeutron) %X2, CorrelatedN
eutrons (iNeutron) %Y2, CorrelatedNeutrons (iNeutron) %Z2) + 1

MLEMNA (CorrelatedNeutrons (iNeutron) %Plane, CorrelatedNeutrons (iNeutron) %X1, Cor
relatedNeutrons (iNeutron) %Y1, CorrelatedNeutrons (iNeutron) %Z1, CorrelatedNeutro
ns (iNeutron) %X2, CorrelatedNeutrons (iNeutron) %Y2, CorrelatedNeutrons (iNeutron) %
Z2) = MLEMNA (CorrelatedNeutrons (iNeutron) %Plane, CorrelatedNeutrons (iNeutron) %X1
, CorrelatedNeutrons (iNeutron) %Y1, CorrelatedNeutrons (iNeutron) %Z1, CorrelatedNe
utrons (iNeutron) %X2, CorrelatedNeutrons (iNeutron) %Y2, CorrelatedNeutrons (iNeutr
on) %Z2) + 1
  if ((ReconstructedEnergyN(iNeutron) > n_emin) .and.
(ReconstructedEnergyN(iNeutron) <= n_emax)) then

MLEMNSAE (CorrelatedNeutrons (iNeutron) %Plane, ceiling ((ReconstructedEnergyN (iNe

```

```

utron)-
n_emin)/n_ebin), ceiling(AngleN(iNeutron)/mlem_angle_bin), CorrelatedNeutrons(i
Neutron)%X1-
CorrelatedNeutrons(iNeutron)%X2+ceiling(real(anint(10000*(xVox(2,3)-
xVox(2,1))))/real(anint(10000*xVox(2,2))))), CorrelatedNeutrons(iNeutron)%Y1-
CorrelatedNeutrons(iNeutron)%Y2+ceiling(real(anint(10000*(yVox(2,3)-
yVox(2,1))))/real(anint(10000*yVox(2,2))))), CorrelatedNeutrons(iNeutron)%Z1-
CorrelatedNeutrons(iNeutron)%Z2+ceiling(real(anint(10000*(zVox(2,3)-
zVox(2,1))))/real(anint(10000*zVox(2,2)))))=MLEMNSAE(CorrelatedNeutrons(iNeut
ron)%Plane, ceiling((ReconstructedEnergyN(iNeutron)-
n_emin)/n_ebin), ceiling(AngleN(iNeutron)/mlem_angle_bin), CorrelatedNeutrons(i
Neutron)%X1-
CorrelatedNeutrons(iNeutron)%X2+ceiling(real(anint(10000*(xVox(2,3)-
xVox(2,1))))/real(anint(10000*xVox(2,2))))), CorrelatedNeutrons(iNeutron)%Y1-
CorrelatedNeutrons(iNeutron)%Y2+ceiling(real(anint(10000*(yVox(2,3)-
yVox(2,1))))/real(anint(10000*yVox(2,2))))), CorrelatedNeutrons(iNeutron)%Z1-
CorrelatedNeutrons(iNeutron)%Z2+ceiling(real(anint(10000*(zVox(2,3)-
zVox(2,1))))/real(anint(10000*zVox(2,2)))))+1

PAIRNSAE(CorrelatedNeutrons(iNeutron)%Plane, ceiling((ReconstructedEnergyN(iNe
utron)-
n_emin)/n_ebin), ceiling(AngleN(iNeutron)/mlem_angle_bin), CorrelatedNeutrons(i
Neutron)%X1, CorrelatedNeutrons(iNeutron)%Z1, CorrelatedNeutrons(iNeutron)%X2, C
orrelatedNeutrons(iNeutron)%Z2)=PAIRNSAE(CorrelatedNeutrons(iNeutron)%Plane, c
eiling((ReconstructedEnergyN(iNeutron)-
n_emin)/n_ebin), ceiling(AngleN(iNeutron)/mlem_angle_bin), CorrelatedNeutrons(i
Neutron)%X1, CorrelatedNeutrons(iNeutron)%Z1, CorrelatedNeutrons(iNeutron)%X2, C
orrelatedNeutrons(iNeutron)%Z2)+1
endif
elseif (CorrelatedNeutrons(iNeutron)%Plane==2) then

MLEMN1(CorrelatedNeutrons(iNeutron)%X2, CorrelatedNeutrons(iNeutron)%Y2, Correl
atedNeutrons(iNeutron)%Z2)=MLEMN1(CorrelatedNeutrons(iNeutron)%X2, CorrelatedN
eutrons(iNeutron)%Y2, CorrelatedNeutrons(iNeutron)%Z2)+1

MLEMNA(CorrelatedNeutrons(iNeutron)%Plane, CorrelatedNeutrons(iNeutron)%X2, Cor
relatedNeutrons(iNeutron)%Y2, CorrelatedNeutrons(iNeutron)%Z2, CorrelatedNeutro
ns(iNeutron)%X1, CorrelatedNeutrons(iNeutron)%Y1, CorrelatedNeutrons(iNeutron)%
Z1)=MLEMNA(CorrelatedNeutrons(iNeutron)%Plane, CorrelatedNeutrons(iNeutron)%X2
, CorrelatedNeutrons(iNeutron)%Y2, CorrelatedNeutrons(iNeutron)%Z2, CorrelatedNe
utrons(iNeutron)%X1, CorrelatedNeutrons(iNeutron)%Y1, CorrelatedNeutrons(iNeutr
on)%Z1)+1
if ((ReconstructedEnergyN(iNeutron) > n_emin) .and.
(ReconstructedEnergyN(iNeutron) <= n_emax)) then

MLEMNSAE(CorrelatedNeutrons(iNeutron)%Plane, ceiling((ReconstructedEnergyN(iNe
utron)-
n_emin)/n_ebin), ceiling(AngleN(iNeutron)/mlem_angle_bin), CorrelatedNeutrons(i
Neutron)%X2-
CorrelatedNeutrons(iNeutron)%X1+ceiling(real(anint(10000*(xVox(1,3)-
xVox(1,1))))/real(anint(10000*xVox(1,2))))), CorrelatedNeutrons(iNeutron)%Y2-
CorrelatedNeutrons(iNeutron)%Y1+ceiling(real(anint(10000*(yVox(1,3)-
yVox(1,1))))/real(anint(10000*yVox(1,2))))), CorrelatedNeutrons(iNeutron)%Z2-
CorrelatedNeutrons(iNeutron)%Z1+ceiling(real(anint(10000*(zVox(1,3)-
zVox(1,1))))/real(anint(10000*zVox(1,2)))))=MLEMNSAE(CorrelatedNeutrons(iNeut
ron)%Plane, ceiling((ReconstructedEnergyN(iNeutron)-
n_emin)/n_ebin), ceiling(AngleN(iNeutron)/mlem_angle_bin), CorrelatedNeutrons(i

```

```

Neutron)%X2-
CorrelatedNeutrons (iNeutron)%X1+ceiling (real (anint (10000* (xVox (1, 3) -
xVox (1, 1)))) /real (anint (10000*xVox (1, 2)))) ,CorrelatedNeutrons (iNeutron)%Y2-
CorrelatedNeutrons (iNeutron)%Y1+ceiling (real (anint (10000* (yVox (1, 3) -
yVox (1, 1)))) /real (anint (10000*yVox (1, 2)))) ,CorrelatedNeutrons (iNeutron)%Z2-
CorrelatedNeutrons (iNeutron)%Z1+ceiling (real (anint (10000* (zVox (1, 3) -
zVox (1, 1)))) /real (anint (10000*zVox (1, 2)))))+1

PAIRNSAE (CorrelatedNeutrons (iNeutron)%Plane, ceiling ((ReconstructedEnergyN (iNeutron) -
n_emin)/n_ebin), ceiling (AngleN (iNeutron)/mlem_angle_bin), CorrelatedNeutrons (iNeutron)%X2, CorrelatedNeutrons (iNeutron)%Z2, CorrelatedNeutrons (iNeutron)%X1, CorrelatedNeutrons (iNeutron)%Z1)=PAIRNSAE (CorrelatedNeutrons (iNeutron)%Plane, ceiling ((ReconstructedEnergyN (iNeutron) -
n_emin)/n_ebin), ceiling (AngleN (iNeutron)/mlem_angle_bin), CorrelatedNeutrons (iNeutron)%X2, CorrelatedNeutrons (iNeutron)%Z2, CorrelatedNeutrons (iNeutron)%X1, CorrelatedNeutrons (iNeutron)%Z1)+1
endif
endif
enddo

do iPhoton = 1, CorrelP_key

MLEMP (CorrelatedPhotons (iPhoton)%X3, CorrelatedPhotons (iPhoton)%Y3, CorrelatedPhotons (iPhoton)%Z3)=MLEMP (CorrelatedPhotons (iPhoton)%X3, CorrelatedPhotons (iPhoton)%Y3, CorrelatedPhotons (iPhoton)%Z3)+1
if (CorrelatedPhotons (iPhoton)%Plane==1) then

MLEMPA (CorrelatedPhotons (iPhoton)%Plane, CorrelatedPhotons (iPhoton)%X1, CorrelatedPhotons (iPhoton)%Y1, CorrelatedPhotons (iPhoton)%Z1, CorrelatedPhotons (iPhoton)%X3, CorrelatedPhotons (iPhoton)%Y3, CorrelatedPhotons (iPhoton)%Z3)=MLEMPA (CorrelatedPhotons (iPhoton)%Plane, CorrelatedPhotons (iPhoton)%X1, CorrelatedPhotons (iPhoton)%Y1, CorrelatedPhotons (iPhoton)%Z1, CorrelatedPhotons (iPhoton)%X3, CorrelatedPhotons (iPhoton)%Y3, CorrelatedPhotons (iPhoton)%Z3)+1
if ((AngleP (iPhoton)>0) .and. (ReconstructedEnergyP (iPhoton) > p_emin) .and. (ReconstructedEnergyP (iPhoton) <= p_emax)) then

MLEMPSAE (CorrelatedPhotons (iPhoton)%Plane, ceiling ((ReconstructedEnergyP (iPhoton) -
p_emin)/p_ebin), ceiling (AngleP (iPhoton)/mlem_angle_bin), CorrelatedPhotons (iPhoton)%X1-CorrelatedPhotons (iPhoton)%X3+ceiling (real (anint (10000* (xVox (3, 3) -
xVox (3, 1)))) /real (anint (10000*xVox (3, 2)))) ,CorrelatedPhotons (iPhoton)%Y1-CorrelatedPhotons (iPhoton)%Y3+ceiling (real (anint (10000* (yVox (3, 3) -
yVox (3, 1)))) /real (anint (10000*yVox (3, 2)))) ,CorrelatedPhotons (iPhoton)%Z1-CorrelatedPhotons (iPhoton)%Z3+ceiling (real (anint (10000* (zVox (3, 3) -
zVox (3, 1)))) /real (anint (10000*zVox (3, 2)))))=MLEMPSAE (CorrelatedPhotons (iPhoton)%Plane, ceiling ((ReconstructedEnergyP (iPhoton) -
p_emin)/p_ebin), ceiling (AngleP (iPhoton)/mlem_angle_bin), CorrelatedPhotons (iPhoton)%X1-CorrelatedPhotons (iPhoton)%X3+ceiling (real (anint (10000* (xVox (3, 3) -
xVox (3, 1)))) /real (anint (10000*xVox (3, 2)))) ,CorrelatedPhotons (iPhoton)%Y1-CorrelatedPhotons (iPhoton)%Y3+ceiling (real (anint (10000* (yVox (3, 3) -
yVox (3, 1)))) /real (anint (10000*yVox (3, 2)))) ,CorrelatedPhotons (iPhoton)%Z1-CorrelatedPhotons (iPhoton)%Z3+ceiling (real (anint (10000* (zVox (3, 3) -
zVox (3, 1)))) /real (anint (10000*zVox (3, 2)))))+1

PAIRPSAE (CorrelatedPhotons (iPhoton)%Plane, ceiling ((ReconstructedEnergyP (iPhoton) -

```

```

p_emin)/p_ebin), ceiling(AngleP(iPhoton)/mlem_angle_bin), CorrelatedPhotons(iPhoton)%X1, CorrelatedPhotons(iPhoton)%Z1, CorrelatedPhotons(iPhoton)%X3, CorrelatedPhotons(iPhoton)%Z3)=PAIRPSAE(CorrelatedPhotons(iPhoton)%Plane, ceiling((ReconstructedEnergyP(iPhoton)-
p_emin)/p_ebin), ceiling(AngleP(iPhoton)/mlem_angle_bin), CorrelatedPhotons(iPhoton)%X1, CorrelatedPhotons(iPhoton)%Z1, CorrelatedPhotons(iPhoton)%X3, CorrelatedPhotons(iPhoton)%Z3)+1
endif
else if (CorrelatedPhotons(iPhoton)%Plane==2) then

MLEMPA(CorrelatedPhotons(iPhoton)%Plane, CorrelatedPhotons(iPhoton)%X2, CorrelatedPhotons(iPhoton)%Y2, CorrelatedPhotons(iPhoton)%Z2, CorrelatedPhotons(iPhoton)%X3, CorrelatedPhotons(iPhoton)%Y3, CorrelatedPhotons(iPhoton)%Z3)=MLEMPA(CorrelatedPhotons(iPhoton)%Plane, CorrelatedPhotons(iPhoton)%X2, CorrelatedPhotons(iPhoton)%Y2, CorrelatedPhotons(iPhoton)%Z2, CorrelatedPhotons(iPhoton)%X3, CorrelatedPhotons(iPhoton)%Y3, CorrelatedPhotons(iPhoton)%Z3)+1
if ((AngleP(iPhoton)>0) .and. (ReconstructedEnergyP(iPhoton) > p_emin) .and. (ReconstructedEnergyP(iPhoton) <= p_emax)) then

MLEMPSAE(CorrelatedPhotons(iPhoton)%Plane, ceiling((ReconstructedEnergyP(iPhoton)-
p_emin)/p_ebin), ceiling(AngleP(iPhoton)/mlem_angle_bin), CorrelatedPhotons(iPhoton)%X2-CorrelatedPhotons(iPhoton)%X3+ceiling(real(anint(10000*(xVox(3,3)-xVox(3,1))))/real(anint(10000*xVox(3,2))))), CorrelatedPhotons(iPhoton)%Y2-CorrelatedPhotons(iPhoton)%Y3+ceiling(real(anint(10000*(yVox(3,3)-yVox(3,1))))/real(anint(10000*yVox(3,2))))), CorrelatedPhotons(iPhoton)%Z2-CorrelatedPhotons(iPhoton)%Z3+ceiling(real(anint(10000*(zVox(3,3)-zVox(3,1))))/real(anint(10000*zVox(3,2))))))=MLEMPSAE(CorrelatedPhotons(iPhoton)%Plane, ceiling((ReconstructedEnergyP(iPhoton)-
p_emin)/p_ebin), ceiling(AngleP(iPhoton)/mlem_angle_bin), CorrelatedPhotons(iPhoton)%X2-CorrelatedPhotons(iPhoton)%X3+ceiling(real(anint(10000*(xVox(3,3)-xVox(3,1))))/real(anint(10000*xVox(3,2))))), CorrelatedPhotons(iPhoton)%Y2-CorrelatedPhotons(iPhoton)%Y3+ceiling(real(anint(10000*(yVox(3,3)-yVox(3,1))))/real(anint(10000*yVox(3,2))))), CorrelatedPhotons(iPhoton)%Z2-CorrelatedPhotons(iPhoton)%Z3+ceiling(real(anint(10000*(zVox(3,3)-zVox(3,1))))/real(anint(10000*zVox(3,2))))))+1

PAIRPSAE(CorrelatedPhotons(iPhoton)%Plane, ceiling((ReconstructedEnergyP(iPhoton)-
p_emin)/p_ebin), ceiling(AngleP(iPhoton)/mlem_angle_bin), CorrelatedPhotons(iPhoton)%X2, CorrelatedPhotons(iPhoton)%Z2, CorrelatedPhotons(iPhoton)%X3, CorrelatedPhotons(iPhoton)%Z3)=PAIRPSAE(CorrelatedPhotons(iPhoton)%Plane, ceiling((ReconstructedEnergyP(iPhoton)-
p_emin)/p_ebin), ceiling(AngleP(iPhoton)/mlem_angle_bin), CorrelatedPhotons(iPhoton)%X2, CorrelatedPhotons(iPhoton)%Z2, CorrelatedPhotons(iPhoton)%X3, CorrelatedPhotons(iPhoton)%Z3)+1
endif
else if ((CorrelatedPhotons(iPhoton)%Plane==3) .and. (AngleP(iPhoton)>0) .and. (ReconstructedEnergyP(iPhoton) > p_emin) .and. (ReconstructedEnergyP(iPhoton) <= p_emax)) then

MLEMPSAE(CorrelatedPhotons(iPhoton)%Plane, ceiling((ReconstructedEnergyP(iPhoton)-
p_emin)/p_ebin), ceiling(AngleP(iPhoton)/mlem_angle_bin), CorrelatedPhotons(iPhoton)%X1-CorrelatedPhotons(iPhoton)%X2+ceiling(real(anint(10000*(xVox(2,3)-xVox(2,1))))/real(anint(10000*xVox(2,2))))), CorrelatedPhotons(iPhoton)%Y1-CorrelatedPhotons(iPhoton)%Y2+ceiling(real(anint(10000*(yVox(2,3)-

```

```

yVox(2,1))) /real (anint (10000*yVox(2,2))) , CorrelatedPhotons (iPhoton)%Z1-
CorrelatedPhotons (iPhoton)%Z2+ceiling (real (anint (10000* (zVox(2,3) -
zVox(2,1)))) /real (anint (10000*zVox(2,2)))) =MLEMPSAE (CorrelatedPhotons (iPhoto
n)%Plane, ceiling ((ReconstructedEnergyP (iPhoton) -
p_emin)/p_ekin) , ceiling (AngleP (iPhoton)/mlem_angle_bin) , CorrelatedPhotons (iPh
oton)%X1-CorrelatedPhotons (iPhoton)%X2+ceiling (real (anint (10000* (xVox(2,3) -
xVox(2,1)))) /real (anint (10000*xVox(2,2))) , CorrelatedPhotons (iPhoton)%Y1-
CorrelatedPhotons (iPhoton)%Y2+ceiling (real (anint (10000* (yVox(2,3) -
yVox(2,1)))) /real (anint (10000*yVox(2,2))) , CorrelatedPhotons (iPhoton)%Z1-
CorrelatedPhotons (iPhoton)%Z2+ceiling (real (anint (10000* (zVox(2,3) -
zVox(2,1)))) /real (anint (10000*zVox(2,2)))))+1
    endif
enddo

if (FileIsDone == 1) then

open (75, file=(trim(output_file)//'_1.cn'), status='replace')
do iY=1, ceiling (real (anint (10000* (yVox(1,3) -
yVox(1,1)))) /real (anint (10000*yVox(1,2))))
    do iZ=1, ceiling (real (anint (10000* (zVox(1,3) -
zVox(1,1)))) /real (anint (10000*zVox(1,2))))
        do iX=1, ceiling (real (anint (10000* (xVox(1,3) -
xVox(1,1)))) /real (anint (10000*xVox(1,2))))-1
            write (75, '(I12,A1,$)') MLEMN1 (iX,iY,iZ), ', '
        enddo
        write (75, '(I12)') MLEMN1 (iX,iY,iZ)
    enddo
enddo
close (75)

open (85, file=(trim(output_file)//'_2.cn'), status='replace')
do iY=1, ceiling (real (anint (10000* (yVox(2,3) -
yVox(2,1)))) /real (anint (10000*yVox(2,2))))
    do iZ=1, ceiling (real (anint (10000* (zVox(2,3) -
zVox(2,1)))) /real (anint (10000*zVox(2,2))))
        do iX=1, ceiling (real (anint (10000* (xVox(2,3) -
xVox(2,1)))) /real (anint (10000*xVox(2,2))))-1
            write (85, '(I12,A1,$)') MLEMN2 (iX,iY,iZ), ', '
        enddo
        write (85, '(I12)') MLEMN2 (iX,iY,iZ)
    enddo
enddo
close (85)

open (76, file=(trim(output_file)//'.cp'), status='replace')
do iY=1, ceiling (real (anint (10000* (yVox(3,3) -
yVox(3,1)))) /real (anint (10000*yVox(3,2))))
    do iZ=1, ceiling (real (anint (10000* (zVox(3,3) -
zVox(3,1)))) /real (anint (10000*zVox(3,2))))
        do iX=1, ceiling (real (anint (10000* (xVox(3,3) -
xVox(3,1)))) /real (anint (10000*xVox(3,2))))-1
            write (76, '(I12,A1,$)') MLEMP (iX,iY,iZ), ', '
        enddo
        write (76, '(I12)') MLEMP (iX,iY,iZ)
    enddo
enddo
close (76)

```



```

open(89,file=(trim(output_file)//'_mlem.cn'),status='replace')
do iPlane = 1,2
  do iY1=1,ceiling(real(anint(10000*(yVox(1,3)-
yVox(1,1)))/real(anint(10000*yVox(1,2))))
    do iZ1=1,ceiling(real(anint(10000*(zVox(1,3)-
zVox(1,1)))/real(anint(10000*zVox(1,2))))
      do iX1=1,ceiling(real(anint(10000*(xVox(1,3)-
xVox(1,1)))/real(anint(10000*xVox(1,2))))
        do iY2=1,ceiling(real(anint(10000*(yVox(2,3)-
yVox(2,1)))/real(anint(10000*yVox(2,2))))
          do iZ2=1,ceiling(real(anint(10000*(zVox(2,3)-
zVox(2,1)))/real(anint(10000*zVox(2,2))))
            do iX2=1,ceiling(real(anint(10000*(xVox(2,3)-
xVox(2,1)))/real(anint(10000*xVox(2,2))))
              write(89,'(I12)') MLEMNA(iPlane,iX1,iY1,iZ1,iX2,iY2,iZ2)
            enddo
          enddo
        enddo
      enddo
    enddo
  enddo
enddo
close(89)

```

```

open(90,file=(trim(output_file)//'_mlem.cp'),status='replace')
do iPlane = 1,2
  do iY1=1,YP1MAX
    do iZ1=1,ZP1MAX
      do iX1=1,XP1MAX
        do iY2=1,ceiling(real(anint(10000*(yVox(3,3)-
yVox(3,1)))/real(anint(10000*yVox(3,2))))
          do iZ2=1,ceiling(real(anint(10000*(zVox(3,3)-
zVox(3,1)))/real(anint(10000*zVox(3,2))))
            do iX2=1,ceiling(real(anint(10000*(xVox(3,3)-
xVox(3,1)))/real(anint(10000*xVox(3,2))))
              write(90,'(I12)') MLEMPA(iPlane,iX1,iY1,iZ1,iX2,iY2,iZ2)
            enddo
          enddo
        enddo
      enddo
    enddo
  enddo
enddo
close(90)

```

```

open(89,file=(trim(output_file)//'_pairsae.cn'),status='replace')
do iPlane = 1,2
  do iEnergy = 1,ceiling((n_emax-n_emin)/n_ebin)
    do iAngle = 1, ceiling(90/mlem_angle_bin)
      do iZ1=1,ceiling(real(anint(10000*(zVox(1,3)-
zVox(1,1)))/real(anint(10000*zVox(1,2))))
        do iX1=1,ceiling(real(anint(10000*(xVox(1,3)-
xVox(1,1)))/real(anint(10000*xVox(1,2))))
          do iZ2=1,ceiling(real(anint(10000*(zVox(2,3)-
zVox(2,1)))/real(anint(10000*zVox(2,2))))

```

```

        do iX2=1,ceiling(real(anint(10000*(xVox(2,3)-
xVox(2,1))))/real(anint(10000*xVox(2,2))))
            write(89,'(I12)')
PAIRNSAE(iPlane,iEnergy,iAngle,iX1,iZ1,iX2,iZ2)
        enddo
    enddo
enddo
enddo
enddo
enddo
close(89)

open(90,file=(trim(output_file)//'_pairsae.cp'),status='replace')
do iPlane = 1,2
    do iEnergy = 1,ceiling((p_emax-p_emin)/p_ebin)
        do iAngle = 1,ceiling(180/mlem_angle_bin)
            do iZ1=1,ZP1MAX
                do iX1=1,XP1MAX
                    do iZ2=1,ceiling(real(anint(10000*(zVox(3,3)-
zVox(3,1))))/real(anint(10000*zVox(3,2))))
                        do iX2=1,ceiling(real(anint(10000*(xVox(3,3)-
xVox(3,1))))/real(anint(10000*xVox(3,2))))
                            write(90,'(I12)')
PAIRPSAE(iPlane,iEnergy,iAngle,iX1,iZ1,iX2,iZ2)
                        enddo
                    enddo
                enddo
            enddo
        enddo
    enddo
enddo
close(90)

open(91,file=(trim(output_file)//'_mlemsae.cn'),status='replace')
do iPlane = 1,2
    do iEnergy = 1,ceiling((n_emax-n_emin)/n_ebin)
        do iAngle = 1, ceiling(90/mlem_angle_bin)
            do iY=1,(ceiling(real(anint(10000*(yVox(1,3)-
yVox(1,1))))/real(anint(10000*yVox(1,2))))-
1)+(ceiling(real(anint(10000*(yVox(2,3)-
yVox(2,1))))/real(anint(10000*yVox(2,2))))-1)+1
                do iZ=1,(ceiling(real(anint(10000*(zVox(1,3)-
zVox(1,1))))/real(anint(10000*zVox(1,2))))-
1)+(ceiling(real(anint(10000*(zVox(2,3)-
zVox(2,1))))/real(anint(10000*zVox(2,2))))-1)+1
                    do iX=1,(ceiling(real(anint(10000*(xVox(1,3)-
xVox(1,1))))/real(anint(10000*xVox(1,2))))-
1)+(ceiling(real(anint(10000*(xVox(2,3)-
xVox(2,1))))/real(anint(10000*xVox(2,2))))-1)+1
                        write(91,'(I12)') MLEMNSAE(iPlane,iEnergy,iAngle,iX,iY,iZ)
                    enddo
                enddo
            enddo
        enddo
    enddo
enddo
enddo
enddo
enddo

```

```

close(91)

open(92,file=(trim(output_file)//'_mlemsae.cp'),status='replace')
do iPlane = 1,3
  do iEnergy = 1,ceiling((p_emax-p_emin)/p_ebin)
    do iAngle = 1,ceiling(180/mlem_angle_bin)
      do iY=1,YPMAX
        do iZ=1,ZPMAX
          do iX=1,XPMAX
            write(92,'(I12)') MLEMPSAE(iPlane,iEnergy,iAngle,iX,iY,iZ)
          enddo
        enddo
      enddo
    enddo
  enddo
enddo
close(92)

deallocate(MLEMN1,MLEMN2,MLEMP,MLEMNA,MLEMPA,MLEMNSAE,MLEMPSAE)

endif

end Subroutine MLEM_input

Subroutine backproject
!
!~~~~~
! This subroutine backprojects the correlated counts onto a meshed sphere
!
!~~~~~

use parameters_m
use Imaging_system_m
use Main_m

integer::teta,fi,done,index1,index2
integer::iBackPro,iMesh,iEnergy,iType
character(len=5)::label
real::spherePoint(3)

!$$$$$
open(87,file=(trim(output_file)//'_Correlated_pulses_after_n.o'),status='repl
ace')
!$$$$$ !NOTE:: Correlated_pulses_n has the form [Plane, Energy1, X1, Y1, Z1,
Time, X2, Y2, Z2, Ideal]
!$$$$$ 335 Format
(F20.6,A1,F20.6,A1,F20.6,A1,F20.6,A1,F20.6,A1,I3,A1,F20.6,A1,F20.6,A1,F20.6,A
1,F20.6,A1,F25.8,A1,F20.6,A1,F20.6,A1,F20.6,A1,I3)
!$$$$$ do iOutput=1,CorrelN_key
!$$$$$ write(87,335)
axisN(iOutput,1),',',axisN(iOutput,2),',',axisN(iOutput,3),',',angleN(iOutput
),',',ReconstructedEnergyN(iOutput),',',CorrelatedNeutrons(iOutput)%Plane,',',

```

```

,CorrelatedNeutrons (iOutput)%Energy1,',',CorrelatedNeutrons (iOutput)%X1,',',C
orrelatedNeutrons (iOutput)%Y1,',',CorrelatedNeutrons (iOutput)%Z1,',',Correlat
edNeutrons (iOutput)%Time1,',',CorrelatedNeutrons (iOutput)%X2,',',CorrelatedNe
utrons (iOutput)%Y2,',',CorrelatedNeutrons (iOutput)%Z2,',',CorrelatedNeutrons (
iOutput)%Ideal
!$$$$$ enddo
!$$$$$ close (87)

!$$$$$
open (88,file=(trim(output_file) //'_Correlated_pulses_after_p.o'),status='repl
ace')
!$$$$$ !NOTE:: Correlated_pulses_p has the form [Plane, Energy1, X1, Y1, Z1,
Energy2, X2, Y2, Z2, Energy3, X3, Y3, Z3, Ideal]
!$$$$$ 336 Format
(F20.6,A1,F20.6,A1,F20.6,A1,F20.6,A1,F20.6,A1,I3,A1,F20.6,A1,F20.6,A1,F20.6,A
1,F20.6,A1,F20.6,A1,F20.6,A1,F20.6,A1,F20.6,A1,F20.6,A1,F20.6,A1,F20.6,A1,F20
.6,A1,I3)
!$$$$$ do iOutput=1,CorrelP_key
!$$$$$ write (88,336)
axisP (iOutput,1),',',axisP (iOutput,2),',',axisP (iOutput,3),',',angleP (iOutput
),',',ReconstructedEnergyP (iOutput),',',CorrelatedPhotons (iOutput)%Plane,',',
CorrelatedPhotons (iOutput)%Energy1,',',CorrelatedPhotons (iOutput)%X1,',',Corr
elatedPhotons (iOutput)%Y1,',',CorrelatedPhotons (iOutput)%Z1,',',CorrelatedPho
tons (iOutput)%Energy2,',',CorrelatedPhotons (iOutput)%X2,',',CorrelatedPhotons
(iOutput)%Y2,',',CorrelatedPhotons (iOutput)%Z2,',',CorrelatedPhotons (iOutput)
%Energy3,',',CorrelatedPhotons (iOutput)%X3,',',CorrelatedPhotons (iOutput)%Y3,
',',CorrelatedPhotons (iOutput)%Z3,',',CorrelatedPhotons (iOutput)%Ideal
!$$$$$ enddo
!$$$$$ close (88)

index1=0
index2=0
done=0
do while (done==0)

if (segment_number == 1) then
    allocate (Image (int ((360/sphere_mesh) * (180/sphere_mesh))), IdealImage (in
t ((360/sphere_mesh) * (180/sphere_mesh)))
    allocate (ImageTypeN (int ((360/sphere_mesh) * (180/sphere_mesh)), 2), IdealI
mageTypeN (int ((360/sphere_mesh) * (180/sphere_mesh)), 2))
    allocate (ImageTypeP (int ((360/sphere_mesh) * (180/sphere_mesh)), 3), IdealI
mageTypeP (int ((360/sphere_mesh) * (180/sphere_mesh)), 3))
    allocate (ImageN (int ((360/sphere_mesh) * (180/sphere_mesh)), ceiling ((n_em
ax-
n_emin)/n_ebin), 2), IdealImageN (int ((360/sphere_mesh) * (180/sphere_mesh)), ceili
ng ((n_emax-n_emin)/n_ebin), 2))
    allocate (ImageP (int ((360/sphere_mesh) * (180/sphere_mesh)), ceiling ((p_em
ax-
p_emin)/p_ebin), 3), IdealImageP (int ((360/sphere_mesh) * (180/sphere_mesh)), ceili
ng ((p_emax-p_emin)/p_ebin), 3))
endif

iMesh=0
teta = 0

```

```

if(distancecheck==.FALSE.) then
    done=1
    label=''
else
    if (segment_number /= 1) then
        write(*,*) ' '
        write(*,*) '!!!FATAL ERROR!!! - Distance check incompatible with file
splitting'
        write(*,*) ' '
    endif
    longdistance=.FALSE.
    index1=index1+1
    if(index1==10) then
        index1=1
        index2=index2+1
    endif
    sphere_radius=(index1*10)*(10**index2)
    write(label,'(I5.5)') int(sphere_radius)
    if(sphere_radius==10000) then
        done=1
    endif
endif

do while (teta<=360-sphere_mesh)
    fi = sphere_mesh
    do while (fi<=180-sphere_mesh)
        iMesh=iMesh+1
        if(longdistance==.TRUE.) then
            spherePoint(1)=sphere_radius*sin(Pi*fi/180)*cos(Pi*teta/180)
            spherePoint(2)=sphere_radius*sin(Pi*fi/180)*sin(Pi*teta/180)
            spherePoint(3)=sphere_radius*cos(Pi*fi/180)
        endif
        if (segment_number /= 1) then
            Image(iMesh)=0
            IdealImage(iMesh)=0
            ImageN(iMesh, :, :)=0
            IdealImageN(iMesh, :, :)=0
            ImageP(iMesh, :, :)=0
            IdealImageP(iMesh, :, :)=0
            ImageTypeN(iMesh, :)=0
            IdealImageTypeN(iMesh, :)=0
            ImageTypeP(iMesh, :)=0
            IdealImageTypeP(iMesh, :)=0
        endif

        do iBackPro=1,CorrelN_key
            if (longdistance==.FALSE.) then

spherePoint(1)=sphere_radius*sin(Pi*fi/180)*cos(Pi*teta/180)+sphere_center(1)
-originN(iBackPro,1)

spherePoint(2)=sphere_radius*sin(Pi*fi/180)*sin(Pi*teta/180)+sphere_center(2)
-originN(iBackPro,2)
            spherePoint(3)=sphere_radius*cos(Pi*fi/180)+sphere_center(3)-
-originN(iBackPro,3)
            endif

```

```

        if ((ReconstructedEnergyN(iBackPro) > n_emin) .and.
(ReconstructedEnergyN(iBackPro) <= n_emax)) then
            if (uncertaintythickness==.TRUE.) then
                ImageN(iMesh, ceiling((ReconstructedEnergyN(iBackPro)-
n_emin)/n_ebin), TypeN(iBackPro))=ImageN(iMesh, ceiling((ReconstructedEnergyN(i
BackPro)-
n_emin)/n_ebin), TypeN(iBackPro))+(1/(SigmaN(iBackPro)*sqrt(2*Pi)))*exp(-
1*(180*acos(DOT_PRODUCT(spherePoint, axisN(iBackPro, :))/sqrt(DOT_PRODUCT(spher
ePoint, spherePoint)*DOT_PRODUCT(axisN(iBackPro, :), axisN(iBackPro, :))))/Pi-
angleN(iBackPro)**2 / (2*SigmaN(iBackPro)**2))

                ImageTypeN(iMesh, TypeN(iBackPro))=ImageTypeN(iMesh, TypeN(iBackPro))+1
/(SigmaN(iBackPro)*sqrt(2*Pi))*exp(-
1*(180*acos(DOT_PRODUCT(spherePoint, axisN(iBackPro, :))/sqrt(DOT_PRODUCT(spher
ePoint, spherePoint)*DOT_PRODUCT(axisN(iBackPro, :), axisN(iBackPro, :))))/Pi-
angleN(iBackPro)**2 / (2*SigmaN(iBackPro)**2))
                if (CorrelatedNeutrons(iBackPro)%ideal == 1) then

IdealImageN(iMesh, ceiling((ReconstructedEnergyN(iBackPro)-
n_emin)/n_ebin), TypeN(iBackPro))=IdealImageN(iMesh, ceiling((ReconstructedEner
gyN(iBackPro)-
n_emin)/n_ebin), TypeN(iBackPro))+(1/(SigmaN(iBackPro)*sqrt(2*Pi)))*exp(-
1*(180*acos(DOT_PRODUCT(spherePoint, axisN(iBackPro, :))/sqrt(DOT_PRODUCT(spher
ePoint, spherePoint)*DOT_PRODUCT(axisN(iBackPro, :), axisN(iBackPro, :))))/Pi-
angleN(iBackPro)**2 / (2*SigmaN(iBackPro)**2))

                IdealImageTypeN(iMesh, TypeN(iBackPro))=IdealImageTypeN(iMesh, TypeN(iBa
ckPro))+1/(SigmaN(iBackPro)*sqrt(2*Pi))*exp(-
1*(180*acos(DOT_PRODUCT(spherePoint, axisN(iBackPro, :))/sqrt(DOT_PRODUCT(spher
ePoint, spherePoint)*DOT_PRODUCT(axisN(iBackPro, :), axisN(iBackPro, :))))/Pi-
angleN(iBackPro)**2 / (2*SigmaN(iBackPro)**2))
                endif
            else
                if
((DOT_PRODUCT(spherePoint, axisN(iBackPro, :))<=sqrt(DOT_PRODUCT(spherePoint, sp
herePoint)*DOT_PRODUCT(axisN(iBackPro, :), axisN(iBackPro, :))))*cos(pi*(angleN(i
BackPro)-cone_thickness/2)/180)) .and.
(DOT_PRODUCT(spherePoint, axisN(iBackPro, :))>=sqrt(DOT_PRODUCT(spherePoint, sph
erePoint)*DOT_PRODUCT(axisN(iBackPro, :), axisN(iBackPro, :))))*cos(pi*(angleN(iB
ackPro)+cone_thickness/2)/180)) then
                    ImageN(iMesh, ceiling((ReconstructedEnergyN(iBackPro)-
n_emin)/n_ebin), TypeN(iBackPro))=ImageN(iMesh, ceiling((ReconstructedEnergyN(i
BackPro)-n_emin)/n_ebin), TypeN(iBackPro))+1

                    ImageTypeN(iMesh, TypeN(iBackPro))=ImageTypeN(iMesh, TypeN(iBackPro))+1
                    if (CorrelatedNeutrons(iBackPro)%ideal == 1) then

IdealImageN(iMesh, ceiling((ReconstructedEnergyN(iBackPro)-
n_emin)/n_ebin), TypeN(iBackPro))=IdealImageN(iMesh, ceiling((ReconstructedEner
gyN(iBackPro)-n_emin)/n_ebin), TypeN(iBackPro))+1

                    IdealImageTypeN(iMesh, TypeN(iBackPro))=IdealImageTypeN(iMesh, TypeN(iBa
ckPro))+1
                endif
            endif
        endif
    endif
endif
endif
endif

```

```

        enddo

        do iBackPro=1,CorrelP_key
            if (longdistance==.FALSE.) then

spherePoint(1)=sphere_radius*sin(Pi*fi/180)*cos(Pi*teta/180)+sphere_center(1)
-originP(iBackPro,1)

spherePoint(2)=sphere_radius*sin(Pi*fi/180)*sin(Pi*teta/180)+sphere_center(2)
-originP(iBackPro,2)
            spherePoint(3)=sphere_radius*cos(Pi*fi/180)+sphere_center(3)-
originP(iBackPro,3)
            endif
            if (angleP(iBackPro) /= -999) then
                if ((ReconstructedEnergyP(iBackPro) > p_emin) .and.
(ReconstructedEnergyP(iBackPro) <= p_emax)) then
                    if (uncertaintythickness==.TRUE.) then
                        ImageP(iMesh,ceiling((ReconstructedEnergyP(iBackPro)-
p_emin)/p_ebin),TypeP(iBackPro))=ImageP(iMesh,ceiling((ReconstructedEnergyP(i
BackPro)-
p_emin)/p_ebin),TypeP(iBackPro))+(1/(SigmaP(iBackPro)*sqrt(2*Pi)))*exp(-
1*(180*acos(DOT_PRODUCT(spherePoint,axisP(iBackPro,:)))/sqrt(DOT_PRODUCT(spher
ePoint,spherePoint)*DOT_PRODUCT(axisP(iBackPro,:),axisP(iBackPro,:))))/Pi-
angleP(iBackPro))**2 / (2*SigmaP(iBackPro)**2))

                        ImageTypeP(iMesh,TypeP(iBackPro))=ImageTypeP(iMesh,TypeP(iBackPro))+(1
/(SigmaP(iBackPro)*sqrt(2*Pi)))*exp(-
1*(180*acos(DOT_PRODUCT(spherePoint,axisP(iBackPro,:)))/sqrt(DOT_PRODUCT(spher
ePoint,spherePoint)*DOT_PRODUCT(axisP(iBackPro,:),axisP(iBackPro,:))))/Pi-
angleP(iBackPro))**2 / (2*SigmaP(iBackPro)**2))
                            if (CorrelatedPhotons(iBackPro)%ideal == 1) then

IdealImageP(iMesh,ceiling((ReconstructedEnergyP(iBackPro)-
p_emin)/p_ebin),TypeP(iBackPro))=IdealImageP(iMesh,ceiling((ReconstructedEner
gyP(iBackPro)-
p_emin)/p_ebin),TypeP(iBackPro))+(1/(SigmaP(iBackPro)*sqrt(2*Pi)))*exp(-
1*(180*acos(DOT_PRODUCT(spherePoint,axisP(iBackPro,:)))/sqrt(DOT_PRODUCT(spher
ePoint,spherePoint)*DOT_PRODUCT(axisP(iBackPro,:),axisP(iBackPro,:))))/Pi-
angleP(iBackPro))**2 / (2*SigmaP(iBackPro)**2))

                            IdealImageTypeP(iMesh,TypeP(iBackPro))=IdealImageTypeP(iMesh,TypeP(iBa
ckPro))+(1/(SigmaP(iBackPro)*sqrt(2*Pi)))*exp(-
1*(180*acos(DOT_PRODUCT(spherePoint,axisP(iBackPro,:)))/sqrt(DOT_PRODUCT(spher
ePoint,spherePoint)*DOT_PRODUCT(axisP(iBackPro,:),axisP(iBackPro,:))))/Pi-
angleP(iBackPro))**2 / (2*SigmaP(iBackPro)**2))
                                endif
                            else
                                if
((DOT_PRODUCT(spherePoint,axisP(iBackPro,:))<=sqrt(DOT_PRODUCT(spherePoint,sp
herePoint)*DOT_PRODUCT(axisP(iBackPro,:),axisP(iBackPro,:)))*cos(pi*(angleP(i
BackPro)-cone_thickness/2)/180)) .and.
(DOT_PRODUCT(spherePoint,axisP(iBackPro,:))>=sqrt(DOT_PRODUCT(spherePoint,sp
herePoint)*DOT_PRODUCT(axisP(iBackPro,:),axisP(iBackPro,:)))*cos(pi*(angleP(iB
ackPro)+cone_thickness/2)/180))) then

ImageP(iMesh,ceiling((ReconstructedEnergyP(iBackPro)-

```

```

p_emin)/p_ebin),TypeP(iBackPro))=ImageP(iMesh,ceiling((ReconstructedEnergyP(i
BackPro)-p_emin)/p_ebin),TypeP(iBackPro))+1

    ImageTypeP(iMesh,TypeP(iBackPro))=ImageTypeP(iMesh,TypeP(iBackPro))+1
        if (CorrelatedPhotons(iBackPro)%ideal == 1) then

IdealImageP(iMesh,ceiling((ReconstructedEnergyP(iBackPro)-
p_emin)/p_ebin),TypeP(iBackPro))=IdealImageP(iMesh,ceiling((ReconstructedEner
gyP(iBackPro)-p_emin)/p_ebin),TypeP(iBackPro))+1

    IdealImageTypeP(iMesh,TypeP(iBackPro))=IdealImageTypeP(iMesh,TypeP(iBa
ckPro))+1
        endif
    endif
    endif
    endif
    endif
enddo

    Image(iMesh)=SUM(ImageN(iMesh,,:,:))+SUM(ImageP(iMesh,,:,:))

IdealImage(iMesh)=SUM(IdealImageN(iMesh,,:,:))+SUM(IdealImageP(iMesh,,:,:))

    fi = fi + sphere_mesh
enddo
    teta = teta + sphere_mesh
enddo

if (FileIsDone == 1) then

open(77,file=(trim(output_file)//trim(label)//'_total.bp'),status='replace')
do iBackPro=1,iMesh
write (77,*)Image(iBackPro)
enddo
close(77)

open(78,file=(trim(output_file)//trim(label)//'_ideal.bp'),status='replace')
do iBackPro=1,iMesh
write (78,*)IdealImage(iBackPro)
enddo
close(78)

open(79,file=(trim(output_file)//trim(label)//'_photon.bp'),status='replace')
do iBackPro=1,iMesh
write (79,*)SUM(ImageTypeP(iBackPro,:))
enddo
close(79)

open(80,file=(trim(output_file)//trim(label)//'_neutron.bp'),status='replace'
)
do iBackPro=1,iMesh
write (80,*)SUM(ImageTypeN(iBackPro,:))
enddo
close(80)

```



```

open(81,file=(trim(output_file)//trim(label)//'_idealphoton.bp'),status='replace')
do iBackPro=1,iMesh
write (81,*)SUM(IdealImageTypeP(iBackPro,:))
enddo
close(81)

open(82,file=(trim(output_file)//trim(label)//'_idealneutron.bp'),status='replace')
do iBackPro=1,iMesh
write (82,*)SUM(IdealImageTypeN(iBackPro,:))
enddo
close(82)

open(93,file=(trim(output_file)//trim(label)//'_photon_ebin.bp'),status='replace')
do iBackPro=1,iMesh
do iEnergy=1,ceiling((p_emax-p_emin)/p_ebin)
write (93,*)ImageP(iBackPro,iEnergy,1), ImageP(iBackPro,iEnergy,2),
ImageP(iBackPro,iEnergy,3)
enddo
enddo
close(93)

open(94,file=(trim(output_file)//trim(label)//'_neutron_ebin.bp'),status='replace')
do iBackPro=1,iMesh
do iEnergy=1,ceiling((n_emax-n_emin)/n_ebin)
write (94,*)ImageN(iBackPro,iEnergy,1), ImageN(iBackPro,iEnergy,2)
enddo
enddo
close(94)

open(95,file=(trim(output_file)//trim(label)//'_idealphoton_ebin.bp'),status='replace')
do iBackPro=1,iMesh
do iEnergy=1,ceiling((p_emax-p_emin)/p_ebin)
write
(95,*)IdealImageP(iBackPro,iEnergy,1),IdealImageP(iBackPro,iEnergy,2),IdealImageP(iBackPro,iEnergy,3)
enddo
enddo
close(95)

open(96,file=(trim(output_file)//trim(label)//'_idealneutron_ebin.bp'),status='replace')
do iBackPro=1,iMesh
do iEnergy=1,ceiling((n_emax-n_emin)/n_ebin)
write (96,*)IdealImageN(iBackPro,iEnergy,1), IdealImageN(iBackPro,iEnergy,2)
enddo
enddo
close(96)

open(93,file=(trim(output_file)//trim(label)//'_photon_type.bp'),status='replace')
do iBackPro=1,iMesh
do iType=1,3

```

```

write (93,*) ImageTypeP(iBackPro,iType)
enddo
enddo
close(93)

open(94,file=(trim(output_file)//trim(label)//'_neutron_type.bp'),status='replace')
do iBackPro=1,iMesh
do iType=1,2
write (94,*) ImageTypeN(iBackPro,iType)
enddo
enddo
close(94)

open(95,file=(trim(output_file)//trim(label)//'_idealphoton_type.bp'),status='replace')
do iBackPro=1,iMesh
do iType=1,3
write (95,*) IdealImageTypeP(iBackPro,iType)
enddo
enddo
close(95)

open(96,file=(trim(output_file)//trim(label)//'_idealneutron_type.bp'),status='replace')
do iBackPro=1,iMesh
do iType=1,2
write (96,*) IdealImageTypeN(iBackPro,iType)
enddo
enddo
close(96)

deallocate(Image,IdealImage)
deallocate(ImageN,IdealImageN,ImageP,IdealImageP)
deallocate(ImageTypeN,IdealImageTypeN,ImageTypeP,IdealImageTypeP)

endif

enddo

deallocate(angleN,angleP)
deallocate(ReconstructedEnergyN,ReconstructedEnergyP)
deallocate(axisN,axisP)
deallocate(TypeN,TypeP)
deallocate(SigmaN,SigmaP)
deallocate(originN,originP)

end Subroutine backproject

```

## Appendix D – Quick Acquisition source code extract

```
#ifndef _IMAGECLASS_H_
#define _IMAGECLASS_H_

#include <cstdio>
#include <cmath>
using namespace std;

class ImageClass
{
private:
    int numChans;
    double** coord;

public:
    double lightCoef[3];

    double minEnergy, maxEnergy;
    int sphereMesh;
    int coneThickness;
    double sphereRadius;
    int* imageP;
    int* imageN;
    int imageLength;

    double spectrumBin, spectrumMax;
    int* spectrumP;
    int* spectrumN;
    int spectrumLength;

    int neutronCounts, photonCounts;
    uint64_t timeRefresh;

    ImageClass()
    {
        numChans = 0;
        sphereMesh = 2;
        coneThickness = 2;
        sphereRadius = 100;
        neutronCounts = 0;
        photonCounts = 0;
        lightCoef[0]=0.03495;
        lightCoef[1]=0.1424;
        lightCoef[2]=-0.036;
        timeRefresh = 10000;
        minEnergy=0;
    }
};
```

```

    maxEnergy=50;
    spectrumBin=0.1;
    spectrumMax=50;
}

~ImageClass()
{
    delete [] imageP;
    delete [] imageN;
    delete [] spectrumP;
    delete [] spectrumN;
    for(int ch=0; ch<numChans; ch++)
    {
        delete [] coord[ch];
    }
    delete [] coord;
}

void setImage()
{
    imageLength = (360/sphereMesh)*((180-
sphereMesh)/sphereMesh);
    spectrumLength = ceil(spectrumMax/spectrumBin)+1;
    imageP = new int [imageLength];
    imageN = new int [imageLength];
    spectrumP = new int [spectrumLength];
    spectrumN = new int [spectrumLength];
    for(int iMesh=0; iMesh<imageLength; iMesh++)
    {
        imageP[iMesh]=0;
        imageN[iMesh]=0;
    }
    for(int iBin=0; iBin<spectrumLength; iBin++)
    {
        spectrumP[iBin]=0;
        spectrumN[iBin]=0;
    }
}

void printImage()
{
    FILE *imagePFile;
    FILE *imageNFile;
    FILE *spectrumFile;
    imagePFile = fopen("photonimage.bp", "wt");
    imageNFile = fopen("neutronimage.bp", "wt");
    spectrumFile = fopen("spectrum.o", "wt");
}

```

```

    for(int iMesh=0; iMesh<imageLength; iMesh++)
    {
        fprintf(imagePFile,"%u\n",imageP[iMesh]);
        fprintf(imageNFile,"%u\n",imageN[iMesh]);
    }
    for(int iBin=0; iBin<spectrumLength; iBin++)
    {
        fprintf(spectrumFile,"%u
%u\n",spectrumN[iBin],spectrumP[iBin]);
    }
    fclose(imagePFile);
    fclose(imageNFile);
    fclose(spectrumFile);
}

void setUpCoordinates(int nBoards, int boardType)
{
    numChans = nBoards*(8+8*boardType);
    coord = new double* [numChans];
    for(int ch=0; ch<numChans; ch++)
    {
        coord[ch] = new double [3];
    }
}

double X(int ch)
{
    return(coord[ch][0]);
}

double Y(int ch)
{
    return(coord[ch][1]);
}

double Z(int ch)
{
    return(coord[ch][2]);
}

void setX(int bd, int nChans, int ch, double value)
{
    coord[bd*nChans+ch][0] = value;
}

void setY(int bd, int nChans, int ch, double value)
{

```

```
    coord[bd*nChans+ch][1] = value;  
}
```

## References

- [1] R. A. Burns, *Fundamentals of Chemistry* (4<sup>th</sup> Ed.). Prentice Hall, 2002.
- [2] *Dictionary of Military and Associated Terms*. (2005).
- [3] <http://www.un.org/disarmament/WMD/Nuclear/NPT.shtml>
- [4] [http://www.oxforddictionaries.com/us/definition/american\\_english/image?q=imaging#image\\_\\_17](http://www.oxforddictionaries.com/us/definition/american_english/image?q=imaging#image__17)
- [5] Needham, Joseph (1986). *Science and Civilization in China: Volume 4, Physics and Physical Technology, Part 1, Physics*. Taipei: Caves Books Ltd. Page 82.
- [6] K. P. Ziock, W. W. Craig, L. Fabris, R. C. Lanza, S. Gallagher, B. K. P. Horn, and N. W. Madden, *Large area imaging detector for long-range, passive detection of fissile material*. IEEE Trans. Nucl. Sci., 51, 2238 – 2244, 2004.
- [7] G. W. Phillips, *Applications of Compton Imaging in Nuclear Waste Characterization and Treaty Verification*. Nuclear Science Symposium Conference Record, (NSS/MIC), IEEE, 1997.
- [8] K. P. Ziock, C. J. Haley, T. B. Gosnell, and J. H. Lupton, *A Gamma-Ray Imager for Arms Control*. IEEE Trans. Nucl. Sci., 39, 1046 –1050, 1992.
- [9] N. Mascarenhas, J. Brennan, K. Krenz, P. Marleau, and S. Mrowka, *Results with the neutron scatter camera*, IEEE Trans. Nucl. Sci., Vol. 56, pp. 1269-1273, 2009.
- [10] A. C. Madden, P. F. Bloser, D. Fourquette, L. Larocque, J. S. Legere, M. Lewis, M. L. McConnell, M. Rousseau, and J. M. Ryan, *An imaging neutron/gamma-ray spectrometer*. Proceedings of SPIE 8710, Chemical, Biological, Radiological, Nuclear, and Explosives (CBRNE) Sensing XIV, 87101L (May 29, 2013)
- [11] R. W. Todd, J. M. Nightingale, and D. B. Everett, *A proposed gamma camera*, Nature, vol. 251, no. 5471, pp. 132–134, 1974.
- [12] D. Herzo, R. Koga, W. A. Millard, S. Moon, J. Ryan, R. Wilson, A. D. Zych, and R. S. White, *A Large Double Scatter Telescope for Gamma Rays and Neutrons*, Nucl. Instr. Meth., vol. 123, pp. 583–597, 1975.
- [13] M. Singh, *An Electronically Collimated Gamma Camera for Single Photon Emission Computed Tomography. Part I: Theoretical Considerations and Design Criteria*, Med. Phys., vol. 10, pp. 421–427, 1983.
- [14] Y. Feng, R. S. Detwiler, J. E. Baciak, and W. Kernan, *Optimized Geometry and Limitations of Compton Cameras with LaBr<sub>3</sub>*, Nuclear Science Symposium Conference Record, (NSS/MIC), IEEE, 2007.
- [15] H. Seo, S. H. Lee, C. H. Kim, S. H. An, J. H. Lee, and C. S. Lee, *Optimal Geometrical Configuration of a Double Scattering Compton Camera for Maximum Imaging Resolution and Sensitivity*, Nucl. Instr. Meth., vol. 591, pp. 80–83, 2008.
- [16] L.E. Smith, C. Chen, D.K. Wehe, Z. He, *Hybrid collimation for industrial gamma-ray imaging: combining spatially coded and compton aperture data*, NIM-A, vol. 462, pp. 576–587, 2001.
- [17] S. A. Pozzi, S. D. Clarke, W. Walsh, E. C. Miller, J.L. Dolan, M. Flaska, B. M. Wiegner, A. Enqvist, E. Padovani, J. K. Mattingly, D. Chichester, and P. Peerani, *MCNPX-PoliMi for Nuclear Nonproliferation Applications*, NIM-A, vol. 694, pp. 119-125, 2012.
- [18] E. C. Miller, S. D. Clarke, M. Flaska, S. A. Pozzi, and P. Peerani, *MCNPX-PoliMi Post-Processing Algorithm for Detector Response Simulations*, Journal of Nuclear Materials Management
- [19] G. E. P. Box and Mervin E. Muller, *A Note on the Generation of Random Normal Deviates*, The Annals of Mathematical Statistics, Vol. 29, No. 2 pp. 610–611, 1958.
- [20] K. Roemer, G. Pausch, C.-M. Herbach, Y. Kong, R. Lentering, C. Plettner, J. Stein, M. Moszynski, T. Swiderski, and T. Szczesniak. *A technique for measuring the energy resolution of low-Z scintillators*, Nuclear Science Symposium Conference Record (NSS/MIC), IEEE, 2009.
- [21] G. F. Knoll, *Radiation Detection and Measurement* (4<sup>th</sup> Ed.). John Wiley & Sons, 2010.
- [22] D. Mitchell, Sandia National Laboratory, *private communications*.
- [23] M. J. Myjak, and C. E. Seifert. *Real-Time Compton Imaging for the GammaTracker Handheld CdZnTe Detector*. IEEE Trans. Nucl. Sci., 55, 769 – 777, 2008.
- [24] I. Pazsit, *private communications*.
- [25] C. E. Ordonez, W. Chang, and A. Bolozdynya, *Angular Uncertainties due to Geometry and Spatial Resolution in Compton Cameras*, IEEE Trans. Nucl. Sci., vol. 46, pp. 1142–1147, 1999.

- [26] S.R. Tornga, and M.W. Rawool Sullivan, and J.P. Sullivan *Three-dimensional Compton Imaging Using List-Mode Maximum Likelihood Expectation Maximization*, IEEE Trans. Nucl. Sci., vol. 56, 1372 – 1376, 2009.
- [27] J. S. Brennan, E. Brubaker, M. Gerling, N. Le Galloudec, P. Marleau, K. McMillan, and A. Nowack, *Results from laboratory tests of the two-dimensional Time-Encoded Imaging System*, Sandia Report, 2014.
- [28] J. S. Brennan, E. Brubaker, N. R. Hilton, P. Marleau, and J. Steele, *Calibration and Simulation of a Coded Aperture Neutron Imaging System*, Nuclear Science Symposium Conference Record (NSS/MIC), IEEE, 2009.
- [29] J. B. Birks, D. W. Fry, L. Costrell, and K. Kandiah, *The Theory and Practice of Scintillation Counting*. Oxford, New York, Pergamon Press, 1964.
- [30] A. Enqvist, C. C. Lawrence, B. M. Wieger, S. A. Pozzi, and T. N. Massey, *Neutron light output response and resolution functions in EJ-309 liquid scintillation detectors*, NIM-A, vol. 715, pp. 79–86, 2013.
- [31] S. P. Ahlen, B. G. Cartwright, and G. Tarle', *Return to unsaturated response of polymeric scintillators excited by relativistic heavy ions*, NIM-A, vol. 147, pp. 321-328, 1977.
- [32] M. Norsworthy et al.
- [33] S. D. Ambers, M. Flaska, and S. A. Pozzi, *A Hybrid Pulse Shape Discrimination Technique with Enhanced Performance at Neutron Energies below 500 keV*, NIM-A, vol. 638, pp. 116-121, 2011.
- [34] K. Ide, M.F. Becchetti, M. Flaska, A. Poitrasson-Riviere, M.C. Hamel, J.K. Polack, C.C. Lawrence, S.D. Clarke, and S.A. Pozzi, *Analysis of a measured neutron background below 6 MeV for fast-neutron imaging systems*, NIM-A, vol. 694, pp. 24–31, 2012.
- [35] E.R. Siciliano, J.H. Ely, R.T. Kouzes, B.D. Milbrath, J.E. Schweppe, and D.C. Stromswold, *Comparison of PVT and NaI(Tl) scintillators for vehicle portal monitor applications*, NIM-A, vol. 550, pp. 647 – 674, 2005.
- [36] S. Zelakiewicz, R. Hctor, A. Ivan, W. Ross, E. Nieters, W. Smith, D. McDevitt, M. Wittbrodt, B. Millbrath, *SORIS—A standoff radiation imaging system*, NIM-A, vol. 652, pp. 5 – 9, 2011.
- [37] R. S. Miller, J. R. Macri, M. L. McConnell, J. M. Ryan, E. Flückiger, L. Desorgher, *SONTRAC: An imaging spectrometer for MeV neutrons*, NIM-A, vol. 505, pp. 36 – 40, 2003.
- [38] B. Ayaz-Maierhafer, J. P. Hayward, K. P. Ziock, M. A. Blackston, and L. Fabris, *Angular resolution study of a combined gamma-neutron coded aperture imager for standoff detection*, NIM-A, vol. 712, pp. 120 – 125, 2013.
- [39] T. Kamae, R. Enomoto, N. Hanada, *A new method to measure energy, direction and polarization of gamma rays*, NIM-A, vol. 260, pp. 254-257, 1987.
- [40] [www.wiener-d.com](http://www.wiener-d.com)
- [41] <http://www.caen.it>
- [42] <http://www.mathworks.com/products/matlab/>
- [43] D. Reilly, N. Ensslin, H. Smith, and S. Kreiner, *Passive Nondestructive Assay of Nuclear Materials*, US NRC, 1991.
- [44] M. C. Hamel, A. Poitrasson-Rivière, J. K. Polack, S. D. Clarke, M. Flaska, S. A. Pozzi, “Design and Analysis of a Two-Plane Dual-Particle Imaging System,” Proceedings of the Institute of Nuclear Materials Management 54th Annual Meeting on CD-ROM, Palm Desert, California, USA. July 14 – 18, 2013.
- [45] M. C. Hamel, J. K. Polack, A. Poitrasson-Rivière, M. Flaska, S. D. Clarke, S. A. Pozzi, A. Tomanin, P. Peerani, *Stochastic image reconstruction for a dual-particle imaging system*, submitted to NIM-A, 2015
- [46] M. C. Hamel, J. K. Polack, A. Poitrasson-Rivière, D. D. Klemm, M. Flaska, S. D. Clarke, S. A. Pozzi, A. Tomanin, P. Peerani, “Time-of-Flight Neutron Spectrum Unfolding for Mixed-Oxide Nuclear Fuel and Plutonium Metal Using a Dual-Particle Imager,” IEEE Nuclear Science Symposium and Medical Imaging Conference Record, November 8–15, 2014, Seattle, Washington, USA.
- [47] J. L. Dolan, M. Flaska, Sara A. Pozzi, D. L. Chichester, *Passive measurements of mixed-oxide fuel for nuclear nonproliferation*, NIM-A, vol. 703, pp. 102 – 108, 2013.
- [48] D. Xu, Z. He, *Gamma-ray energy-imaging integrated spectral deconvolution*, NIM-A, vol. 574, pp. 98 – 109, 2007.
- [49] J. K. Polack, A. Poitrasson-Rivière, M. C. Hamel, K. Ito, S. D. Clarke, M. Flaska, S. A. Pozzi, A. Tomanin, P. Peerani, “Image Reconstruction of Shielded Mixed-Oxide Fuel Using a Dual-Particle Imaging System,” IEEE Nuclear Science Symposium and Medical Imaging Conference Record, November 8–15, 2014, Seattle, Washington, USA.
- [50] F. Acerbi, A. Ferri, A. Gola, N. Zorzi, and C. Piemonte, *Analysis of single-photon time resolution of FBK silicon photomultipliers*, NIM-A, vol. 787, pp. 34-37, 2015.
- [51] T. Yanagida, K. Watanabe, and Y. Fujimoto, *Comparative study of neutron and gamma-ray pulse shape discrimination of anthracene, stilbene, and p-terphenyl*, NIM-A, vol. 784, pp. 111-114, 2015.
- [52] S. A. Pozzi, M. M. Bourne, and S. D. Clarke, *Pulse shape discrimination in the plastic scintillator EJ-299-33*, NIM-A, vol. 723, pp. 19-23, 2013.



- [53] E. van Loef, G. Markosyan, U. Shirwadkar, M. McClish, and K. Shah, *Gamma-ray spectroscopy and pulse shape discrimination with a plastic scintillator*, NIM-A, vol. 788, pp. 71-72, 2015.
- [54] J. K. Polack, M. C. Hamel, A. Poitrasson-Rivière, P. Marleau, M. Flaska, S. D. Clarke, S. A. Pozzi, "Spectrum Isolation in Multi-Source Image Reconstruction Using a Dual-Particle Imager," Proceedings of the Institute of Nuclear Materials Management 56th Annual Meeting on CD-ROM, Palm Desert, California, USA. July 12 – 16, 2015.